



Michigan Technological University
Create the Future Digital Commons @ Michigan Tech

Dissertations, Master's Theses and Master's
Reports - Open

Dissertations, Master's Theses and Master's
Reports

2007

Non-intrusive pressure measurement in microchannels

Derek Fultz

Michigan Technological University

Follow this and additional works at: <https://digitalcommons.mtu.edu/etds>

 Part of the [Mechanical Engineering Commons](#)

Copyright 2007 Derek Fultz

Recommended Citation

Fultz, Derek, "Non-intrusive pressure measurement in microchannels", Master's Thesis, Michigan Technological University, 2007.

<https://doi.org/10.37099/mtu.dc.etds/361>

Follow this and additional works at: <https://digitalcommons.mtu.edu/etds>

 Part of the [Mechanical Engineering Commons](#)

NON-INTRUSIVE PRESSURE MEASUREMENT IN
MICROCHANNELS

By

Derek Fultz

A THESIS

Submitted in partial fulfillment of the requirements

for the degree of

Master of Science in Mechanical Engineering

MICHIGAN TECHNOLOGICAL UNIVERSITY

2007

This thesis, “NON-INTRUSIVE PRESSURE MEASUREMENT IN MICROCHANNELS” is hereby approved in partial fulfillment of the requirements of the Degree of Master of Science in Mechanical Engineering.

Department of Mechanical Engineering - Engineering Mechanics

Advisor: _____
Jeffrey S. Allen PhD

Committee Member: _____
Amitabh Narain PhD

Committee Member: _____
Yoke Khin Yap PhD

Department Chair: _____
Professor William W. Predebon

Date: _____

ABSTRACT

NON-INTRUSIVE PRESSURE MEASUREMENT IN MICROCHANNELS

Derek Fultz

Michigan Technological University, 2007

A non-intrusive interferometric measurement technique has been successfully developed to measure fluid compressibility in both gas and liquid phases via refractive index (RI) changes. The technique, consisting of an unfocused laser beam impinging a glass channel, can be used to separate and quantify cell deflection, fluid flow rates, and pressure variations in microchannels. Currently in fields such as microfluidics, pressure and flow rate measurement devices are orders of magnitude larger than the channel cross-sections making direct pressure and fluid flow rate measurements impossible. Due to the non-intrusive nature of this technique, such measurements are now possible, opening the door for a myriad of new scientific research and experimentation.

This technique, adapted from the concept of Micro Interferometric Backscatter Detection (MIBD), boasts the ability to provide comparable sensitivities in a variety of channel types and provides quantification capability not previously demonstrated in backscatter detection techniques. Measurement sensitivity depends heavily on experimental parameters such as beam impingement angle, fluid volume, photodetector sensitivity, and a channel's dimensional tolerances. The current apparatus readily quantifies fluid RI changes of 10^{-5} refractive index units (RIU) corresponding to pressures of approximately 14 psi and 1 psi in water and air, respectively. MIBD reports detection capability as low as 10^{-9} RIU and the newly adapted technique has the potential to meet and exceed this limit providing quantification in the place of detection. Specific device sensitivities are discussed and suggestions are provided on how the technique may be refined to provide optimal quantification capabilities based on experimental conditions.

ACKNOWLEDGMENTS

I would like to thank all the family, friends, classmates, and professors who have provided help and encouragement throughout my college years. Without your support, I could never have made it to this point.

Also, a special thanks to my advisor, Dr. Jeffrey Allen, for continually pushing me to test new ideas and become a better student, researcher, and engineer. The educational, travel, and employment opportunities you have given me have not only enhanced my college experience, but my life experience as well.

CONTENTS

<i>Abstract</i>	i
<i>Acknowledgments</i>	ii
<i>Table of Contents</i>	iii
<i>List of Figures</i>	v
<i>List of Tables</i>	x
1. <i>Introduction</i>	1
2. <i>Interferometry</i>	3
2.1 Types of Interferometers	3
2.2 Basic Interferometric Theory	6
3. <i>Backscattering Interferometry</i>	10
3.1 The History of Backscattering Interferometry	10
3.2 The MIBD Technique	10
3.3 Scientific Advancements from MIBD	13
4. <i>Related Scientific Work and Measurement Techniques</i>	15
4.1 RI Measurement Methods	15
4.2 Related Measurement Techniques	17
5. <i>Experimental Description</i>	19
5.1 Adapted Backscattering Setup	19
5.2 Experimental Parameters - Thin Walled Channels	21
5.3 Experimental Parameters - Thick Walled Channels	22
5.4 Fringe Formation	23
5.5 Geometric Path Length Derivation	26
6. <i>Data Processing Procedures</i>	29
6.1 Counting Fringes	29
6.2 Fringe Tracking in Spotlight	30
6.3 Fringe Tracking in Matlab	30
6.4 Relating the FFT to Spatial Images	34

7. <i>Experimental Results</i>	38
7.1 Channel Cross-Section Less than Beam Diameter	38
7.2 Channel Cross-Section Greater than Beam Diameter	48
8. <i>Verification of Results</i>	61
8.1 Laser Stability Testing	61
8.2 Deflection Testing	64
8.3 Verification with Known Data	67
8.4 Description of Matlab Codes Used in Data Processing	70
9. <i>Device Sensitivity</i>	71
9.1 Detection Limits	71
9.2 Effects of Experimental Parameters	71
9.3 Sources of Experimental Error	73
10. <i>Conclusions</i>	76
 <i>Appendix</i>	 80
A. <i>Syringe Pump Calibration</i>	81
B. <i>Pressure Transducer Claibration</i>	85
C. <i>Spotlight Fringe Tracking Results</i>	87
D. <i>Laser Stability Plots</i>	90
E. <i>Configurations for Results Verification</i>	94
E.1 Tube Pinch-Off Mechanism	94
E.2 Michelson Interferometer for Deflection Testing	94
F. <i>Fringe Tracking Program</i>	97
G. <i>Matlab Code for Static Pressure Test Processing</i>	102
H. <i>Matlab External Functions</i>	108
I. <i>Program to Find Sensitivity Using Water</i>	110
J. <i>Program to Find Sensitivity Using Air</i>	112

LIST OF FIGURES

2.1	The classic Michelson interferometer.	4
2.2	The Mach-Zehnder interferometer, commonly used for single pass RI measurements.	5
2.3	The Sagnac Interferometer, commonly used in performing angular velocity measurements.	6
2.4	The Fabry-Perot, commonly used to measure the wavelength of light.	7
3.1	The MIBD experimental setup in which an unfocused laser beam is reflected from a capillary tube resulting in a backscattered arc of interference fringes [2].	11
3.2	Ray trace of the light path through a circular channel resulting in multiple reflections. The vertical lines represent the side walls of the channel [3].	12
3.3	Cross sectional view of ray trace through a circular channel resulting in a 360° backscattered arc [3].	12
3.4	The use of a bicell photodetector for detection of fringe shift. The detector consists of two photo-sensitive sectors represented by the white rectangles over the left fringe [1].	13
4.1	Experimental setup for the laser-capillary-cube technique showing interference due to reflection and refraction of incoming light rays.	16
5.1	Simplified ray trace of the light path through a capillary scale channel from the side view.	20
5.2	Capillary tube and fringe acquisition apparatus showing beam behavior as series of green lines superimposed on the image.	20
5.3	Experimental apparatus used in flow testing.	21
5.4	Formation of fringes caused by primary reflections from glass surface at top and inner wall of a capillary tube (rays b and d from Figure 5.1).	22
5.5	Diagram of experimental apparatus used in static pressure tests of the thick walled channels.	23
5.6	The formation of fringes from planar light waves emitted from two sources (planar waves appear spherical at macro-scale.	25
5.7	Typical diversity of fringe types produced from different channel sizes and geometries. Note that red arrows denote fringe shift direction.	25
5.8	Ray trace of a beam through the thick walled rectangular channel used in derivation of the path length difference relationship.	26
5.9	Formation of fringes from the thick walled channel shown in Figure 5.8	26

6.1	Typical fringe pattern captured from a 500 micron square glass capillary.	31
6.2	Eight areas of interest manually placed on the intensity threshold used for interface tracking in Spotlight.	31
6.3	Filtered fringe image used to smooth laser speckle at edges and increase tracking accuracy.	32
6.4	Flow of image processing which occurs in the program to prepare fringe images for tracking.	34
6.5	FFT produced from the grayscale image. The centered FFT is characterized by low frequency content at its center. Upon zooming of this area one can distinguish the energy (white spots) associated with the fringes.	35
6.6	Multiplication of FFT and Gaussian low pass filter in the frequency domain resulting in a filtered fringe image. Note that the filter is shown in both 2D and 3D for ease in viewing.	35
6.7	Threshold of filtered image set at about half the range of intensities present. The eight bit images have pixel intensity values of zero to 255, thus all areas above the max threshold value are set to white (255 in the case of eight bit and one in the case of binary) resulting in the black and white image shown at the right.	36
6.8	Generic line patterns and their corresponding FFTs. The pattern at the right is a sum of the previous three showing the frequency domain result of having periodicity in three directions [4].	37
7.1	Typical thin walled capillary tube mounted with padded clamps in preparation for flow rate testing. Note that the channel is plumbed using plastic couplers which can be melted around in the inlet and outlet of the channel. The outlet is open to atmospheric conditions to facilitate pressure estimations from pressure drop calculations. . . .	40
7.2	Plot of fringe shift due to fluid flow at various velocities in a 500 micron square microchannel.	40
7.3	Plot showing fringe shift tracked by the eight AOI's shown in Figure 6.2.	41
7.4	Plot showing fringe thickness tracked by the eight AOI's shown in Figure 6.2.	42
7.5	Plot of fringe shift with respect to an implied pressure drop in a 500 micron square microchannel. Note that the outlet is open to atmospheric conditions.	42
7.6	Plot showing results of fringe tracking for three AOI's on a round glass capillary of 0.9375 mm inner diameter. The pump was not properly primed at the point where no fringe shift occurred.	43
7.7	Fringe tracked by Matlab program described in Chapter 6 to study fringe morphology. Red and green borders denote areas that are tracked by the program through each frame.	44

7.8	Shift of interface shown in red in Figure 7.7 through a series of 460 frames. The z-direction shows the magnitude of the fringe shift. Flow was initiated at frame 30 and extinguished at frame 300.	45
7.9	Thickness change calculated from the difference between interfaces shown in red and green in Figure 7.7. The z-direction shows fringe thickness which decreases as the pump is initiated at frame 30 and increases to the original values and the pump is extinguished.	45
7.10	Thick walled square microchannel used to study effects of RI change and channel wall deflection on fringe shift.	46
7.11	Thick walled round microchannel used to isolate the effects of RI change and channel wall deflection on fringe shift.	47
7.12	Rectangular channel with relatively thin walls and channel width significantly larger than the laser beam diameter.	48
7.13	Fringe shift at various fluid flow velocities for the thin walled rectangular channel shown in Figure 7.12.	49
7.14	Dimensionless shift at various static pressures for the thin walled rectangular channel shown in Figure 7.12. As channel deflects due to pressurization, the shift becomes non-linear.	50
7.15	Thickness change of a bright fringe at various static pressures for the thin walled rectangular channel shown in Figure 7.12.	51
7.16	Rectangular channel with thick walls and channel width significantly larger than the laser beam diameter.	52
7.17	Fringe shifts due to fluid flow in a 50 micron channel with thick side walls for three separate test sequences.	53
7.18	Fringe shift due to static channel pressurization using distilled water and the test cell shown in Figure 7.16.	54
7.19	Fringe thickness changes due to static channel pressurization using distilled water and the test cell shown in Figure 7.18.	54
7.20	Fringe shift of left and right sides of interrogated fringe due to static channel pressurization using air and the test cell shown in Figure 7.16.	55
7.21	Dimensionless fringe shift due to static channel pressurization using air and the test cell shown in Figure 7.16.	56
7.22	Fringe thickness changes due to static channel pressurization using air in the test cell shown in Figure 7.16.	56
8.1	Simple optical arrangement used in testing laser intensity fluctuations.	57
8.2	Shift of one side of a fringe captured at 3 fps showing error in shift detection (manifested as variation in the z-direction) caused primarily by intensity fluctuations and mechanical vibrations.	58
8.3	Intensity fluctuations displayed by a 1.5 mW HeNe laser as captured by a photodetector.	59
8.4	Mirror placed on top flow channel to make up second leg of a Michelson interferometer and test for plate deflection in the top surface of the channel.	61

8.5	FEA analysis of thick walled rectangular channel under a static pressure of 5 psig. Deflection of the impingement area is shown in blue and is approximately 18 nm when both sides of the cell are considered.	62
8.6	Rotated view of Figure 8.5 showing deflection of bottom surface of cell in the z-direction.	63
8.7	Estimation of cell deflection using finite element model with a mesh size of 0.8 mm.	64
8.8	Behavior of deflection estimation as mesh size is decreased at a static pressure of 5 psig. The mesh appears to converge at a value near 19 nm for this pressure value, a slight overestimation of the experimental results as expected.	64
8.9	Comparison of finite element model results with calculated deflections based on experimental data for air and water.	66
9.1	Plot of the experimental results for cell pressurization with air showing components of the signal from channel deflection and fluid RI change.	70
9.2	Plot of the experimental results for cell pressurization with water showing components of the signal from channel deflection and fluid RI change.	70
A.1	Calibration of syringe pump for use with a 50.0 cubic centimeter capacity syringe.	78
A.2	Calibration of syringe pump for use with a 5.0 cubic centimeter capacity syringe.	79
B.1	Calibration of pressure transducer using an inclined manometer.	80
C.1	Tracking of fringe position and thickness using eight AOI's at a pump flow setting of 17.	81
C.2	Tracking of fringe position and thickness using eight AOI's at a pump flow setting of 19.	81
C.3	Tracking of fringe position and thickness using eight AOI's at a pump flow setting of 21.	82
C.4	Tracking of fringe position and thickness using eight AOI's at a pump flow setting of 23.	82
C.5	Tracking of fringe position and thickness using eight AOI's at a pump flow setting of 25.	82
C.6	Tracking of fringe position and thickness using eight AOI's at a pump flow setting of 27.	83
C.7	Tracking of fringe position and thickness using eight AOI's at a pump flow setting of 29.	83
D.1	Laser intensity fluctuations as captured by the photodetector approximately 2 minutes after laser startup.	84
D.2	Laser intensity fluctuations as captured by the photodetector approximately 10 minutes after laser startup.	85

D.3	Laser intensity fluctuations as captured by the photodetector approximately 16 minutes after laser startup.	85
D.4	Laser intensity fluctuations as captured by the photodetector approximately 23 minutes after laser startup.	86
D.5	Laser intensity fluctuations as captured by the photodetector approximately 70 minutes after laser startup.	86
D.6	Laser intensity fluctuations as captured by the photodetector approximately 120 minutes after laser startup.	87
E.1	Tube pinch-off mechanism used to induce pressure increases at detection point of backscatter set-up.	88
E.2	Backscatter setup showing placement of pinch-off mechanism and observation channel mounting.	88
E.3	Mirror placement on 50 micron channel for deflection sensing leg of Michelson interferometer.	89
E.4	Components of the Michelson interferometer used to detect displacements in the glass channel under increased pressure and fluid flow. . .	89

LIST OF TABLES

7.1	Various channel cross-section geometries and sizes used in testing.	39
7.2	Fringe shift results for flow rate selections 3-17. Areas of interest 2, 3, and 4 were placed at the top, middle and bottom of a light-dark interface, respectively.	44
7.3	Fringe shift data as well as corresponding velocity and pressure drop values calculated using Equation 7.2. Negative fringe shifts represent experimental error in addition to instances where the pump was not properly primed for flow. Raw data indicated an error of plus or minus two pixels.	49
8.1	Laser intensity fluctuation characteristics observed at various time intervals after startup.	58
A.1	Linear velocity of syringe pump at various flow rate settings.	77
A.2	Calibration using 50.0 cc Syringe.	78
A.3	Calibration using 5.0 cc Syringe.	79

1. INTRODUCTION

The growing field of microfluidics has proven to have applications ranging across scientific disciplines from biology and chemistry to materials science and mechanical engineering. Microchannels, named after their small geometry and defined by their low Bond number characteristics, are used in studying surface tension driven fluid mechanics here on earth where gravity governs larger systems. In microchannels, the Bond number (essentially a dimensionless relationship between gravitational and surface tension forces) is sufficiently low to allow surface tension to dominate the system. As a result of this observation, it is of interest to measure this driving force to better understand how this phenomenon may be controlled, manipulated, and put to use. The small size of such channels renders it impossible to accurately measure the forces within such systems using modern day pressure transducers. To meet this goal, it is desirable to develop a non-contact measurement device to quantify and study system characteristics. A technique has recently been proven which is adaptable to achieve such ambitions.

Micro interferometric backscatter detection (MIBD) is a very simple optical technique in which a laser is used to create high contrast interference fringes which shift based upon changes in the refractive index (RI) of a fluid within the microchannel. The details of the technique are left to Chapter 3, however, simply stated this detection technique is highly applicable to the study of microsystems. Sensitivity has been reported to detect changes as low as 10^{-7} refractive index units (RIU - a change in RI) in channels ranging in size from 1 mm to 30 μm using the MIBD technique and 10^{-9} RIU using a related technique, dual capillary dual bicell MIBD (DCDB MIBD), also discussed in Chapter 3 [1, 3]. Typically, characteristics that are difficult to directly measure in microsystems such as temperature, pressure, and concentration are all functions of RI, therefore, MIBD can theoretically allow for detection of changes in these parameters. In practice, no data has been published demonstrating that the technique can successfully be implemented to exceed a detection capability and perform measurements of such characteristics except under specific, in-situ circumstances. Additionally, no work has been done to implement MIBD for pressure detection. This is believed to be due to unpredictable channel deflection caused by pressurization which typically dominates the signal, making pressure detection an impractical application.

The objective of this research was to successfully adapt the MIBD technique to perform pressure detection and measurements in microchannels. From this information, characteristics such as fluid flow rate, velocity, and acceleration can typically be extracted depending upon the fluid flow regime. For example, it is known that the refractive index of water is a function of pressure and varies by approximately

0.000016 RIU for each atmosphere of pressure variation below 4 atm [5]. This falls well within the detection capability of MIBD, however, at such pressures the geometry of a microchannel has been found to be considerably altered thus making such detections seemingly impossible. This presents a need for an ability to detect channel deflection and separate the components of the signal to accurately quantify Δ RIU and channel geometry changes. Through the use of fluids with known pressure to RI relationships, the signals have successfully been deconvolved providing an ability to detect and quantify pressure changes within microchannels. This leads to an ability to quantify parameters that are functions of pressure such as fluid compressibility (both gas and liquid phases), fluid flow rates, and fluid velocities. This also leads to a wide variety of scientific applications for this research, perhaps the most interesting of which have not yet been realized by the extent of the work presented herein.

2. INTERFEROMETRY

Interferometry is the science of combining light waves to cause interference. As two beams of light occupy the same space at the same time they tend to interfere with one another causing areas of constructive and destructive interference. This interference is manifested as a series of light and dark bands in 2-D space, known as fringes in interferometry, which move based upon changes in phase. This change in phase is synonymous with the physical path length difference between the interfering waves of light. The movement of the interference bands, referred to as a fringe shift, can be used to quantify parameters that modify the path length traveled by the light. Such parameters may include RI, the geometry of the system, or any property that is a function of these parameters such as temperature, pressure, and concentration. Physically, the thickness of each fringe at a given magnification represents a path length equal to the wavelength of the light used to create the fringes. The common practice is therefore to measure the fringe shift based upon the number of fringes to pass a point on an observation screen. This number of fringes is then directly related to the physical path length change of the light which can be used to quantify a myriad of physical phenomena. The method used in counting fringes and the techniques effective in the quantification of shift data are discussed in greater detail in Chapter 6.

2.1 *Types of Interferometers*

There are several very common types of interferometers used in both research and industry. The simplest and oldest type, shown in Figure 2.1 is known as the Michelson interferometer. Historically this interferometric configuration was used in Michelson and Morley's attempt to study light traveling through the aether, which later resulted in disproving the aether concept altogether. Today, this type of interferometer can be used for other scientific applications such as highly sensitive deflection, flatness, temperature and RI measurements [6]. The Michelson interferometer begins at a coherent light source such as a laser which emits a beam that is then divided by a beam splitter, typically into two equally intense portions. These beams are then reflected by mirrors back towards the beam splitter. During this event, one beam is passed through a glass plate, as shown in the 2.1, to compensate for the phase difference caused by the thickness of the beam splitter. When the apparatus is properly aligned, the light waves are then recombined causing interference fringes which can be viewed on an observation screen or by a photodetector as shown in Figure 2.1. This interferometer is easily implemented as a deflection measurement device since one mirror can readily be attached to a system of interest. As the mirror moves there is a path length

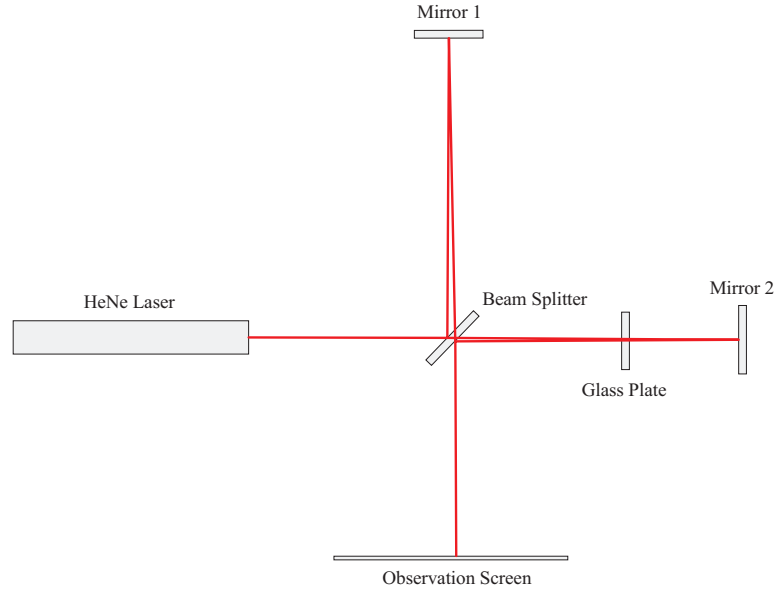


Fig. 2.1. The classic Michelson interferometer.

difference in one arm of the interferometer causing a fringe shift. Depending upon fringe shift detection capabilities, deflection measurements have been reported as low as 10^{-10} cm [7]. Implementation of this technique for detection of channel deflection is described in Chapter 8.

In addition to the Michelson interferometer, another very common configuration is known as the Mach-Zehnder interferometer. This device, shown in Figure 2.2, is commonly used to perform refractive index and temperature measurements. Here an incoming beam is once again divided by a beam splitter. The separate beams are then reflected from mirrors and directed towards a second beam splitter which recombines the two causing interference fringes. This configuration is particularly useful for small transparent samples which can be placed into one arm of the interferometer, as shown in Figure 2.2. Insertion of such a sample causes a path length change between the two beams resulting in a fringe shift. This configuration has also proven useful in measuring the quality and flatness of optical components as well as the thickness of transparent media and the index of refraction of optically transparent samples. One limitation of this arrangement is the fact that the light only makes a single pass through the sample. For other configurations such as MIBD (discussed in Chapter 3), the Michelson interferometer, and the Fabry-Perot interferometer shown in Figure 2.4, two or more passes through the sample can lead to double the detection sensitivity.

Yet another very common type of interferometer is known as the Sagnac interferometer. Under this arrangement, three mirrors are used in conjunction with a beam splitter to send the divided rays of light in opposing circular paths as shown in Figure 2.3. This interferometric assembly is particularly useful in the measurement of angular velocity and acceleration. As the device is rotated in one particular direction, the velocity of the light in that direction is decreased relative to the light traveling in

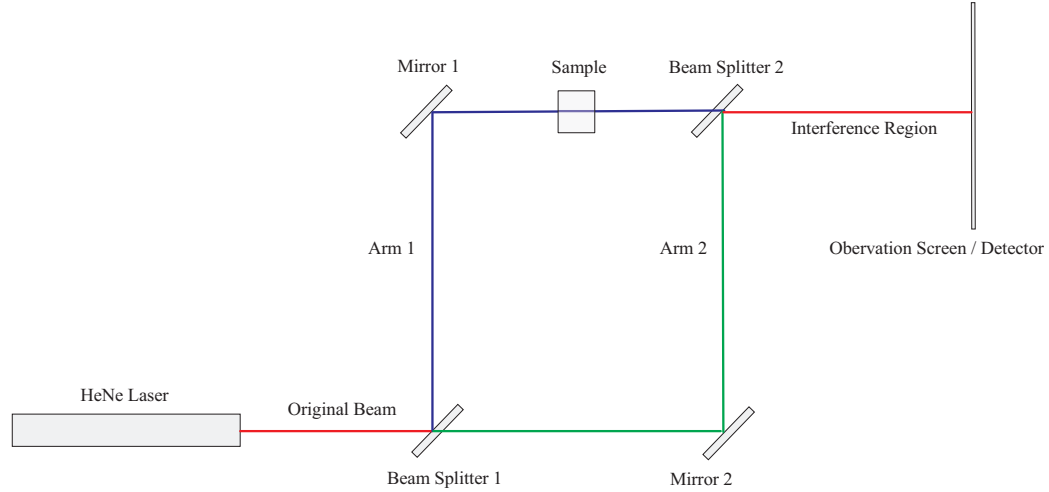


Fig. 2.2. The Mach-Zehnder interferometer, commonly used for single pass RI measurements.

the opposite direction. This velocity difference is manifested as a phase shift, causing a measurable fringe shift which can be related back to the angular velocity of the device. A drawback to this device is the fact that it must be rotated to produce a response, therefore it is desired that it be miniaturized to minimize its inertial effects on the system of interest.

A final common arrangement is known as the Fabry-Perot interferometer which is shown in Figure 2.4. This configuration uses two parallel half silvered plates to reflect a beam several times through a medium of index of refraction, n . Since the plates are only partially reflective, a portion of the light is transmitted upon each reflection resulting in a group of transmitted rays at one side of the apparatus and a group of reflected rays at the other. Generally, either the transmitted or reflected rays are analyzed to determine information such as the value of n , the RI of the medium between the plates, or the wavelength of the light composing the incoming beam [8]. Since the interference pattern is constructed of multiple reflected beams, it is classified as a multiple source interference and the fringe pattern attained can look quite unique in comparison to those produced from the previous interferometric arrangements. Since this technique is not utilized in this research, the description of this configuration will remain brief and further investigation will be left to the reader.

The formation of these unique fringes is dependent upon the phase of each exiting beam. When multiple beams are in phase with one another, there is a large peak of constructive interference. Conversely, when beams are out of phase there is an area of destructive interference. The contrast between these interference regions as well as their width is directly related to the construction of the interferometer, which includes the wavelength of the light, plate spacing, RI of the material occupying the separation, plate reflectivity, and beam impingement angle [9]. Typically these parameters remain constant with the exception of the impingement angle or the plate separation. Through modification of one of these variables, the device is most com-

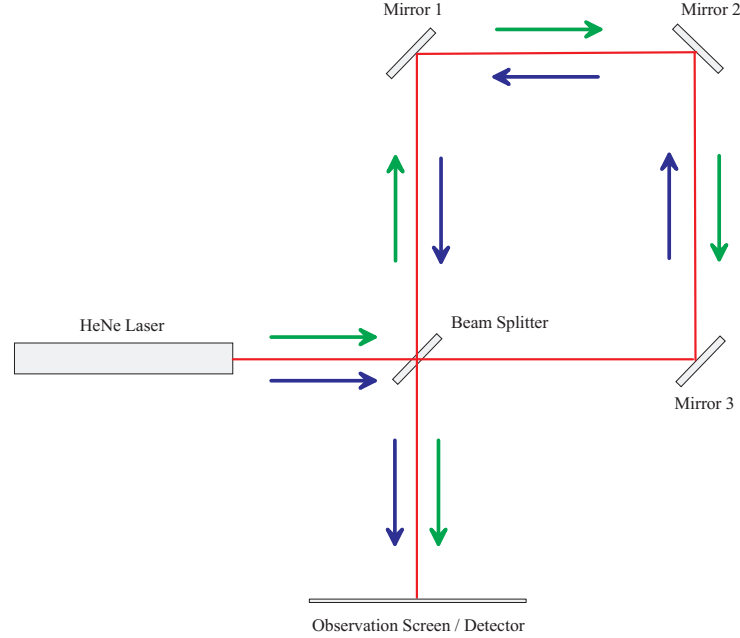


Fig. 2.3. The Sagnac Interferometer, commonly used in performing angular velocity measurements.

only used to determine the wavelength of the incoming beam. Since the exiting beams are constructively interfering with one another, the maximum interference will occur when all of these beams are perfectly in phase [8]. By varying plate separation until the maximum intensity of the constructive interference peaks occurs, the wavelength can be extracted through known physical relationships of the geometry of the interferometer. Succinctly put, by varying plate separation, the Fabry-Perot interferometer is used to determine the wavelengths present in a light source.

temperature, RI, pressure, displacement, and astronomy, fiber optics, and plasma physics.

2.2 Basic Interferometric Theory

In this section, relationships are given to better describe the method by which interferometers are used in performing the measurements referred to in Section 2.1. Relationships for path length and phase changes are described for the Michelson and Mach-Zehnder interferometers. In addition, the relationship for intensity of fringes, or visibility, is provided in more detail. Finally, the relationships describing multiple beam interference and the Fabry-Perot interferometer are presented to bring additional clarity to this complex phenomenon.

Once again considering the Michelson arrangement shown in Figure 2.1 one can imagine a beam of light traversing one arm of the interferometer. To complete the path of the first arm, the light would travel from the laser source then reflect from the beam splitter to mirror one where it would then be reflected back to the beam

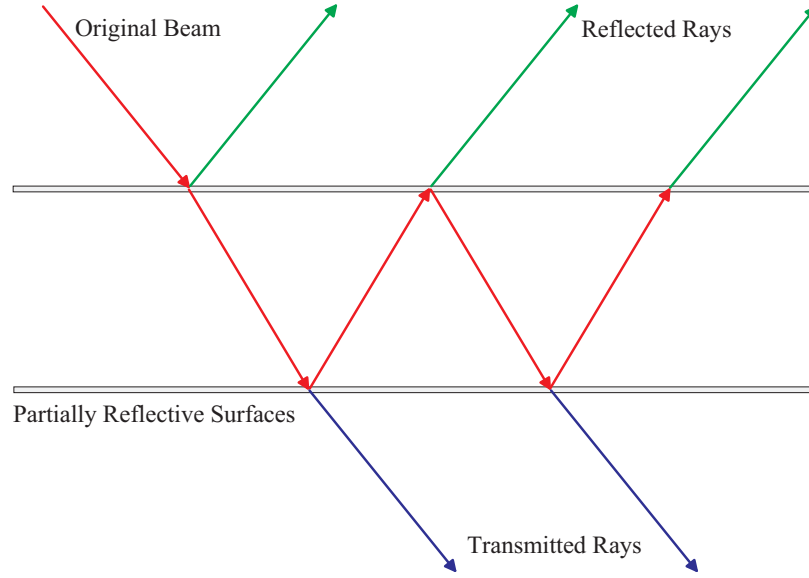


Fig. 2.4. The Fabry-Perot, commonly used to measure the wavelength of light.

splitter. At this point, the light would partially be reflected back into the laser source, referred to as retro-reflection (not shown), and the remainder would travel through the beam splitter to the observation screen or detector. In this case, the optical phase of the wave propagating this path can be represented as:

$$\Phi_1 = \frac{2\pi}{\lambda} n_1 L_1 \quad (2.1)$$

where λ is the wavelength of the light, n_1 is the index of refraction of the medium through which the light propagates, and L_1 is the distance from the beam splitter to mirror 1. Arm two can be described in the exact same manner where the subscripts in Equation 2.1 then describe the characteristics of path two. In the event that a physical displacement of the mirrors is to be measured, it is often more convenient to describe the phase difference between the paths in terms of a physical path length difference, δ . Initially, this can be expressed as:

$$\delta = 2L_2 - 2L_1 = 2\Delta L \quad (2.2)$$

To find this value interferometrically, one must recall that each fringe represents a path length equal to one wavelength of the light being used. Therefore, the number of fringes, m , multiplied by the wavelength provides the physical path length difference ΔL . When multiplied by two we are left with the classical formula for optical metrology given as:

$$\Delta\delta = \Delta m \lambda \quad (2.3)$$

Where $\Delta\delta$ represents the change in the path length difference, Δm describes the number of fringes to pass a given point on the observation screen during a fringe

shift event. The technique for counting fringes to quantify path length differences is described in greater detail in Section 6.1.

Additionally, the visibility of the fringes, V , used in optical analyses can be important to one's ability to accurately quantify information. This is expressed most simply as:

$$V = \frac{I_{max} - I_{min}}{I_{max} + I_{min}} \quad (2.4)$$

Where I_{max} and I_{min} are the maximum and minimum intensities, respectively, found from the relationship [7]:

$$I = I_1 + I_2 + 2\sqrt{I_1 I_2} \cos \theta \cos \Delta\Phi \exp \frac{-\Delta l}{l_c} \quad (2.5)$$

where I_1 and I_2 are the measured intensities of the beams from arms one and two (typically a voltage output from a photo sensitive diode or detector), $\Delta\Phi$ can be found using Equation 2.1 and θ is defined as the angle between the polarization vectors. That is to say, the original beam may have polarization modes in several directions, typically perpendicular to one another, giving θ a value of 90° . Finally, $\Delta l = L_1 - L_2$ and l_c is defined as the coherence length, where:

$$l_c = \frac{\lambda^2}{\Delta\lambda} \quad (2.6)$$

In 2.6 λ is the wavelength of the light and $\Delta\lambda$ is the variation in the wavelength of the signal. From 2.6 one can see why coherent light is preferable for interferometry since it is primarily a single wavelength resulting in a small $\Delta\lambda$ and thus more visible fringes.

The Fabry-Perot interferometer requires the inclusion of an incoming beam angle, θ , to represent the phase difference. Therefore, equation 2.1 becomes [9]:

$$\Phi = \frac{2\pi}{\lambda} 2nt \cos \theta \quad (2.7)$$

where λ is once again the wavelength of the light, n is the RI of the medium separating the plates, t is the plate separation, and θ is the angle of the incoming beam measured from the normal of the inner surface. Here the additional two is from the fact that reflected rays travel twice (or a multiple of two) through the sample before exiting the device as shown in Figure 2.4. The transmission equation of the device is then found to be [9]:

$$T = \frac{(1 - R)^2}{1 + R^2 - 2R \cos \phi} \quad (2.8)$$

where R is the reflection coefficient of the planar surfaces. Knowing the transmission of light through the interferometer, one can plot this value as a function of wavelength to determine the wavelength of the incoming illumination source since, as discussed earlier, the transmission will be maximum when the optical path length difference between the transmitted beams is an integer multiple of the wavelength. In this case, the path length difference would be given by:

$$\delta = 2nt \cos \theta \quad (2.9)$$

Using these relationships one can therefore use the maximum transmission value, T_{max} , from Equation 2.8 to find the wavelength of light entering the interferometer. Commonly referred to as a wavemeter, this configuration is most frequently implemented for accurate measurement of the wavelength produced by coherent light sources, such as lasers. In knowing the wavelength of the light being used, Equation 2.9 in combination with Equation 2.3 can then be applied to study RI changes or plate separations based on a fringe shift value. A procedure very similar to this will be utilized to quantify such values in later chapters.

3. BACKSCATTERING INTERFEROMETRY

3.1 *The History of Backscattering Interferometry*

Micro Interferometric Backscatter Detection (MIBD) was first developed in the early 1990's by Dr. Daryl Bornhop of Texas Technological University as a method of determining refractive index (RI) changes in very small fluid volumes (as low as 10^{-12} liters) for use in chemistry and biochemistry based settings [2, 3, 10]. The technique was patented in 1994 as a new form of interferometer and has displayed excellent sensitivity for examining micro scale systems and equally small volumes of fluid. Since the emergence of the MIBD technique it has shown outstanding promise as a detection mechanism for changes of system parameters. However, it has lacked in quantification of these values as well as repeatability between measurement systems presenting a need for constant in-situ calibration.

Since its inception, MIBD has been refined by Bornhop and others to show in-situ RI measurements with sensitivity on the order of 10^{-9} as well as corresponding temperature relationships based on detection of the change in RI [3, 10, 11]. The setup has also been modified to provide flow rate measurements through the use of a heated slug of fluid created by impingement of an infra-red laser source [12]. In addition, the technique has proven to be useful in detection of concentration, solute, and impurity levels. This has been confirmed to be highly applicable to bedside blood analysis and protein binding experimentation [10]. Despite the demonstrated improvements and capabilities of this technique, it has not yet been shown to provide results for flow rate or pressure quantification within these channels.

3.2 *The MIBD Technique*

The method uses a coherent light source, such as a laser, to impinge a small fluid filled channel, which in turn reflects the high intensity light from its inner and outer surfaces resulting in light interference fringes as seen in interferometry [13]. This reflected light can then be detected using any light sensing device, although photodetectors and camera sensors are most commonly implemented for this purpose. The experimental apparatus, shown in Figure 3.1, has several variations, but most commonly uses a HeNe laser to reflect light from a small channel either mounted to a solid surface or molded into a PDMS or silicon chip. The only stipulation to the technique is that the beam must be larger than the channel diameter. Without this criterion, the apparatus forms the more common etalon or Fabry-Perot interferometer as was discussed in Section 2.1. The reflected light, referred to as backscatter, forms an arc unique to the

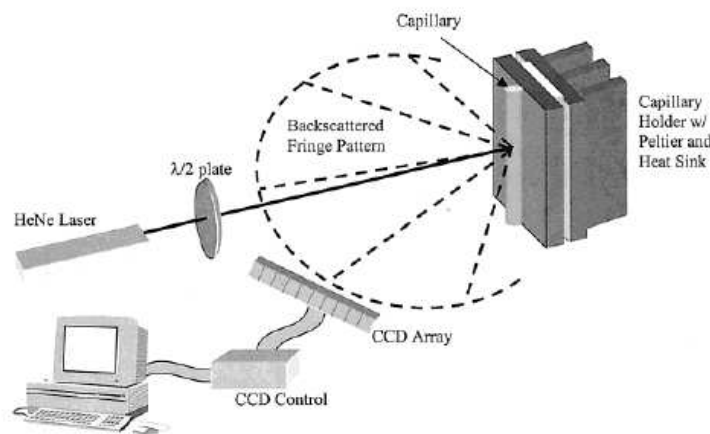


Fig. 3.1. The MIBD experimental setup in which an unfocused laser beam is reflected from a capillary tube resulting in a backscattered arc of interference fringes [2].

MIBD technique which contains the interferometric fringe pattern observed to shift with changes in RI of the fluid inside the channel. A portion of this backscattered arc is then captured for interrogation by a CCD camera or photodetector as shown in Figure 3.1.

Although the backscattered arc is unique, it inherently makes quantification of fringe data more difficult than the traditional interferometric methods discussed in Chapter 2. Figures 3.2 and 3.3 show the backscattering effect resulting in the emission of light 360° around the channel from a cross-sectional and top view, respectively. These theoretical ray trace models are helpful in realizing the complexity of the fringe pattern produced and provide a great deal of understanding of the behavior of light rays upon impingement of the channel. In both cases, the beam impinges from the right and several rays are selected to be representative of the typical backscattering behavior. For example, nearly all rays experience multiple reflections in the channel before exiting. This multi-pass characteristic acts as an amplification mechanism for the interferometric signal. Essentially, a backscattered ray of light has experienced at least twice the phase lag that a typical pass-through ray would experience such as in the case of the Mach-Zehnder interferometer described in Section 2.1. As a result, this technique has double the sensitivity for rays directly backscattered when compared to a single-pass beam acting on a channel of the same size.

The sensitivity of fringes formed by the backscattered light decreases as the backscattered angle (the angle between a backscattered ray and the incoming beam) increases. This is because those rays not directly backscattered travel less distance through the channel and in turn experience less phase lag. This phenomena was first observed extensively by Sorensen who visualized the effect showing lesser fringe shifts at greater backscattering angles [10].

As discussed earlier, a CCD camera is often used for fringe shift observation and will be discussed further in the coming chapters. Another commonly reported technique is known as the bicell method. Here, a bicell photodetector is centered over a fringe of interest as shown in Figure 3.4. Here the two white rectangles represent

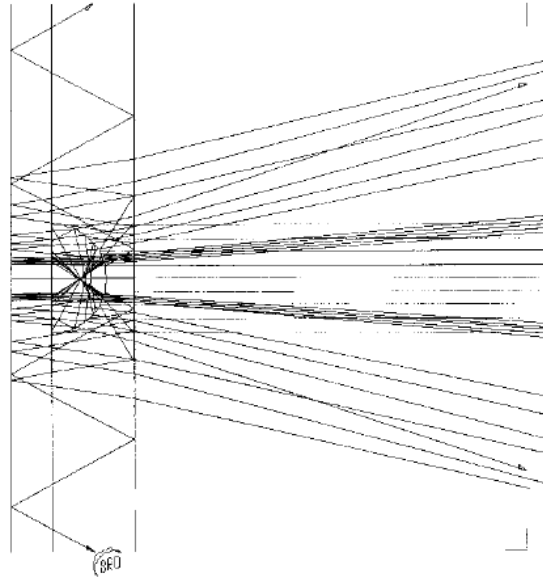


Fig. 3.2. Ray trace of the light path through a circular channel resulting in multiple reflections. The vertical lines represent the side walls of the channel [3].

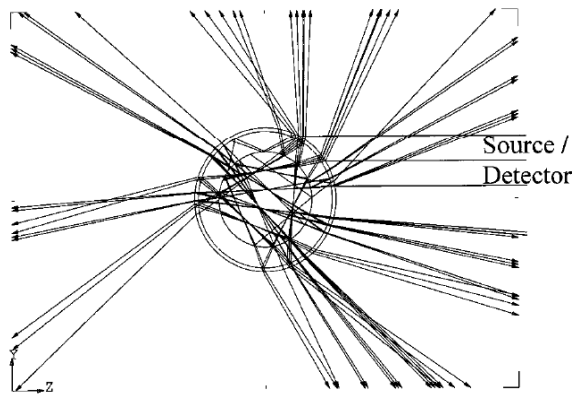


Fig. 3.3. Cross sectional view of ray trace through a circular channel resulting in a 360° backscattered arc [3].

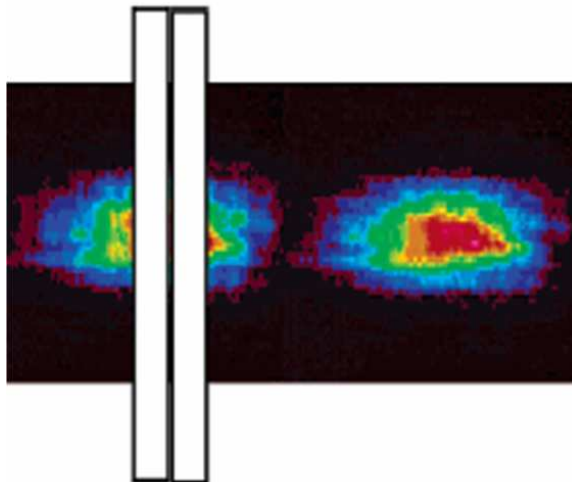


Fig. 3.4. The use of a bicell photodetector for detection of fringe shift. The detector consists of two photo-sensitive sectors represented by the white rectangles over the left fringe [1].

the two sides or cells of the detector. It is important to note that the fringes are shown in false color representation with the greatest light intensity at their centers. Each cell of the apparatus has light detecting ability and the intensity produces a voltage which is averaged over each side of the cell. The output signal is given as:

$$S = \frac{A - B}{A + B} \quad (3.1)$$

Where S is the signal of the detector in volts, A is the voltage average of one side, and B is the voltage average of the other [1]. Using this differential voltage, the movement of a fringe in the horizontal direction can be quantified. Depending upon fringe magnification and detector size, this method has the potential to track movements as low as 10^{-6} meters. This highly sensitive tracking capability provides tremendous detection potential, however, since the thickness of the fringe is not known, quantification is unfortunately limited to in-situ calibrations as reported in the results of Bornhop et al. [1, 14].

3.3 Scientific Advancements from MIBD

As discussed in Section 3.1, the sensitivity of the backscatter technique gives it wide applicability for the measurement and detection of parameters depending upon RI. In 2002, Dmitry Markov and Bornhop successfully measured refractive index changes beyond 10^{-7} RIU in fluid volumes as small as 10^{-9} liters [2]. Such a feat was not possible with previous techniques since such small fluid volumes inherently present a very short distance of light travel and causing only small phase differences between arms of an interferometer. Traditionally, this kept detection limits at or below 10^{-7} RIU.

Due to the unprecedented ability to detect changes in RI as well as perform in-situ measurements, MIBD (or OCIBD, the on-chip version) has also been shown to detect temperature changes as low as 10^{-6} °C [1]. As a result, “the extent of Joule heating in chip-scale capillary electrophoresis” was measured for the first time [14]. In this experiment, a silicon chip with isotropically etched channels was used in the backscattering setup to capture the heating effects of capillary electrophoresis proving that present theoretical models in the field were not yet adequate and underestimated the values measured in-situ.

Finally, the technique has also been expanded to include two channels and two photodetectors side-by-side [1]. With this apparatus, one channel acts as a reference for the other thus aiding to eliminate the effects of errors such as mechanical vibrations, laser intensity fluctuations, and thermal drift. Using this technique, referred to as DCDB MIBD, a detection limit of 6.9×10^{-9} RIU is achieved for temperature ranges between 24 and 30°C, opening the door to a myriad of new chemistry and biochemistry applications.

4. RELATED SCIENTIFIC WORK AND MEASUREMENT TECHNIQUES

4.1 *RI Measurement Methods*

Numerous RI measurement techniques currently exist, most of which use coherent laser light and interferometric methods to compare the phase lag between an unaltered beam and one traveling through a medium of interest. As discussed in Chapter 2, the Mach-Zehnder and Fabry-Perot interferometers are two optical instruments commonly used to perform RI measurements via correlation to fringe shift. Similarly, in Chapter 3 it was noted that MIBD can be used as a highly sensitive detector to changes in RI using fringes created by light reflection from channels with micron-scale cross-sections.

Aside from those methods previously discussed, many important methods exist for measurement of RI presenting a wide range of applicability with sensitivities as low as 10^{-6} RIU. Direct measurement of the index of refraction of air has been proven using an evacuable cell and a Fabry-Perot interferometer [15]. By placing the cell between the plates of the interferometer and slowly evacuating the air with a vacuum pump, the optical resonance can be utilized to determine the change in RI of the air within the cell. In the context of the discussion in Section 2.2, the transmission maximum changes position leading to the appearance of fringe shift which can be counted throughout the evacuation process. Similarly, a permanently evacuated cell can be placed within part of a Fabry-Perot interferometer. Upon comparison of the wavelengths causing resonance in the evacuated and non-evacuated parts of the cell, one can determine the absolute RI of the air. These results were verified with the Edlén formula indicating a measurement range of 2×10^{-6} RIU for a laser tuning range of 1 GHz [15].

Another RI measurement method is referred to as the laser-cube-capillary technique. This instrument uses a glass cube through which a 1.0 mm hole is bored. Using a laser beam with a diameter of 0.8 mm to directly impinge a flat face of the cube, light is directed through the bored channel perpendicular to its axis. The wall thickness is chosen to be significantly thicker than that of the hole diameter to act as a thermal mass and allow RI measurements under pressure [16]. It is noted by Menn and Lotrian that the fragile nature of capillary tubes deems them un-usable for RI measurements under pressures different than atmospheric, a conjecture proven only partially true by the work in this thesis.

The capillary cube method uses the detection of an interferometric fringe shift to quantify fluid RI changes. Upon passing through the bored channel, the light

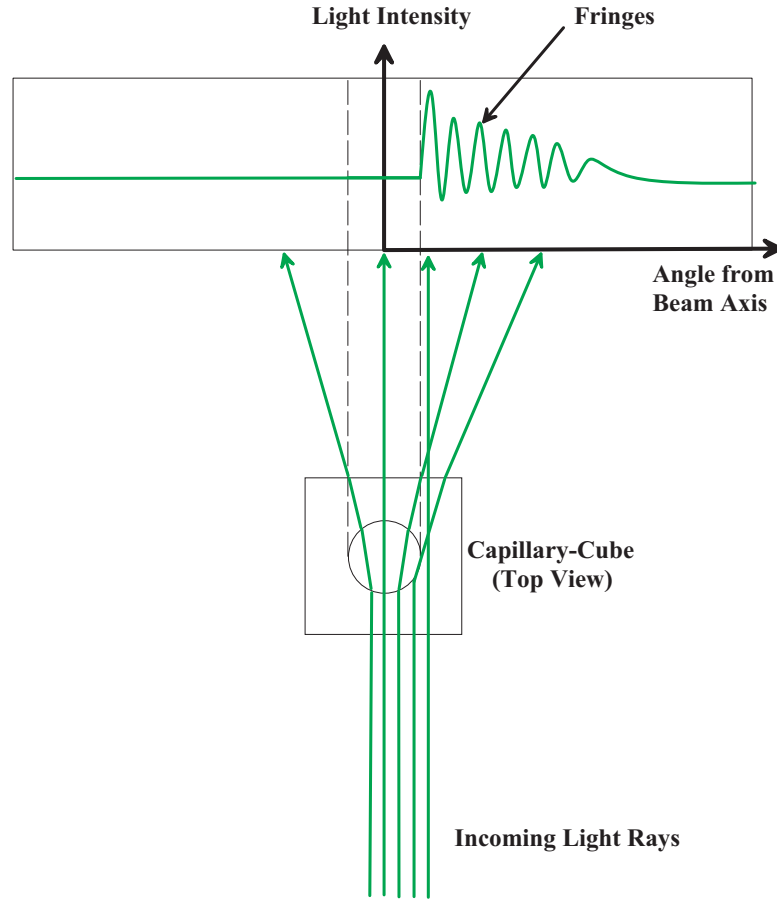


Fig. 4.1. Experimental setup for the laser-capillary-cube technique showing interference due to reflection and refraction of incoming light rays.

is bent slightly away from the axis of the bore when the RI of the fluid inside the channel is lower than that of the capillary cube. This is because the light will always bend toward the medium of highest RI. Since the bore is circular, this bending is exaggerated such that a portion of the light travels beyond the cross section of the channel thus interfering with reflections of its outer wall resulting in fringes as shown in Figure 4.1 [16]. Although this technique has similarities to the adapted backscattering technique, it differs in several areas. First, it is a single pass-through technique which results in only half the sensitivity of the double pass-through MIBD technique under the same experimental parameters. In addition, this technique is not directly applicable for the study of flowing systems and requires a specialized cell to acquire RI information. Finally, the channel dimensions are relatively large in comparison to the backscattering technique, an undesirable feature for studying fluid behavior in small systems.

A final mechanism for the measurement of RI is capable of quantification to ± 0.0002 RIU in liquids such as water and hexane. Using two quartz plates separated by a thin layer of air one may submerge the apparatus in a liquid medium of interest. Upon passing a monochromatic beam through the liquid of interest as well

as the sandwiched plates, one can determine the absolute RI of the liquid. This is done by carefully rotating the plates until the critical angle of the glass is reached and the beam no longer exits the apparatus. Assuming the critical angle of the glass as well as the RI of the glass and air are well known, one can geometrically solve for the RI of the liquid. The accuracy of the solution depends primarily on one's ability to determine the angle of the plates. Results from this technique have been proven to match the results of others for the temperature dependency of liquid RI to as low as 10^{-4} RIU [17].

4.2 *Related Measurement Techniques*

Several other techniques for pressure and flow rate measurement related to the adapted backscattering setup also exist. One very important technique is the use of a refractive index detector (RID) as a pressure transducer for online viscometry in exclusion chromatography [18]. In this method, a standard differential refractive index detector is used to measure the pressure drop in capillary tubes via changes in RI to determine fluid flow rate and viscosity. Under temperature controlled conditions in a capillary of known dimensions, Poiseuille's formula for laminar flow may be used to confidently calculate fluid flow rate or viscosity based on a measured pressure drop provided one of the parameters is known.

In the experimental apparatus for this method, the RID is plumbed to the inlet of the capillary and the exit is open to a waste container. The RID is a differential unit which utilizes a reference or non-pressurized fluid cell in addition to the pressurized fluid cell and provides a signal of the change in RI between the two. This technique has been reported to provide RI changes on the order of 10^{-6} RIU and pressure measurements on the order of hundreds of Pascals [18]. Typically liquid refractive index changes approximately 10^{-5} RIU per atm indicating a much higher pressure at the inlet of the capillary in addition to the pressure drop. This work is not non-intrusive as in the case of the adapted backscattering technique since the detector must be plumbed into the capillary system. In addition, the detection scheme uses existing RID technology which is limited to measurements of 10^{-6} RIU changes whereas MIBD is capable of detection three orders of magnitude lower.

Optical techniques have also been developed for the measurement of pressure and skin friction [19]. In this technique a surface stress-sensitive film is deposited on a part to be tested in a wind tunnel. Based upon the deformation of this film, the surface stresses and pressures can be calculated. The technique utilizes a specialized light source and dedicated data acquisition and processing unit. Although computationally intensive, the method has proven to produce comparable results to those found using pressure sensitive paints, pressure taps, and CFD [19]. Due to the versatility of this technique, it could be used to measure the deflection of a capillary channel under pressure and thus deduce the flow rate and pressure levels within the channel.

An alternative pressure measurement apparatus for micro-scale systems is the use of optical fibers. Micromachined drum-like membranes can be attached to the end of such fibers in order to create optical interference effects based upon deflections in the

membrane. These devices are attached to optical fibers via a RI matched cement. The micromachined device consists of an index matched bowl shaped sheet of glass to which silicon nitride or polysilicon films are attached. The films act as a highly sensitive deflectable membrane which is able to detect changes in temperature and pressure when attached to a surface of interest [20]. Although exact sensitivities of this technique are not yet known, it is an excellent alternative to the problem of micro-scale pressure measurements.

A similar technique utilizes two optical fibers and a reflecting diaphragm to make pressure measurements as an optical microphone. In this case the minimum detectable pressure was found to be 680 micropascals per root hertz providing a dynamic range from 0.01 Hz to 20 kHz, a span beyond that of the human ear [21]. Although this device is too sensitive to make bulk fluid pressure measurements, it is yet another interesting alternative for pressure measurement in microsystems.

5. EXPERIMENTAL DESCRIPTION

5.1 *Adapted Backscattering Setup*

A 5 mW green HeNe laser beam (543 nm wavelength) is passed through a neutral density filter then directed downward using a mirror where it impinges a fluid filled capillary scale tube at an angle between 7° and 30° from the surface normal. Light is then reflected off the inner and outer surfaces of the tube, as shown in Figure 5.1, resulting in high contrast interference fringes which shift with the changing path length difference of the light. This reflected light pattern is then expanded using a -25 mm focal length (divergent) lens, passed through a linear polarizer, and captured using a CCD sensor as displayed in Figure 5.2. A schematic of the entire setup can be seen in Figure 5.3. Using this technique, both square and round capillaries were observed, ranging in size from 0.341 to 0.9375 mm round inner diameter and 200 to 500 micron square inner dimensions. The entire optical train forms an interferometer, similar to a Fabry-Perot or parallel plate interferometer, and creates an arc of interference fringes unique to the MIBD setup. It should be noted that the channel orientation is slightly different than that depicted in Figure 3.1 for the MIBD setup. This changes the behavior of the light slightly, however, fringe formation acts on similar principles and becomes much easier to visualize and control.

The channel is fixed to a stainless steel X-Y translational stage using a pair of padded clamps to minimize deflection of the detection area during testing. The channel is a drawn glass round or square pipette, 10 cm in length, connected to a 50 cc Hamilton syringe (model number 1050) using polyethylene tubing of the corresponding size. The channels were connected using wax, super glue, or plastic couplers depending upon size, geometry, and the flow rates being observed. Fluid was forced through the system at various velocities using a Model 975 Harvard Apparatus compact infusion pump. A listing of these flow velocities along with the corresponding pump settings can be found in the pump calibration in Appendix A.

When the laser is adjusted to impinge the channel and the CCD sensor is properly positioned, interference fringes are displayed on a monitor. To properly position the camera, the top and bottom reflections from the tube, rays b and d in Figure 5.1, must overlap as illustrated in Figure 5.4. The result of a partial overlap between the rays backscattered from the top and bottom of a round channel can be seen here where the contributions from the top and bottom reflections are bounded by the red and black rectangles, respectively. One can observe a movement in these fringes when flow is introduced into the system. This shift occurs due to an index of refraction variation in the liquid as well as a deflection in the channel walls. An analysis of the contribution of each of these signals is left for the discussion in Chapters 7 and 8.

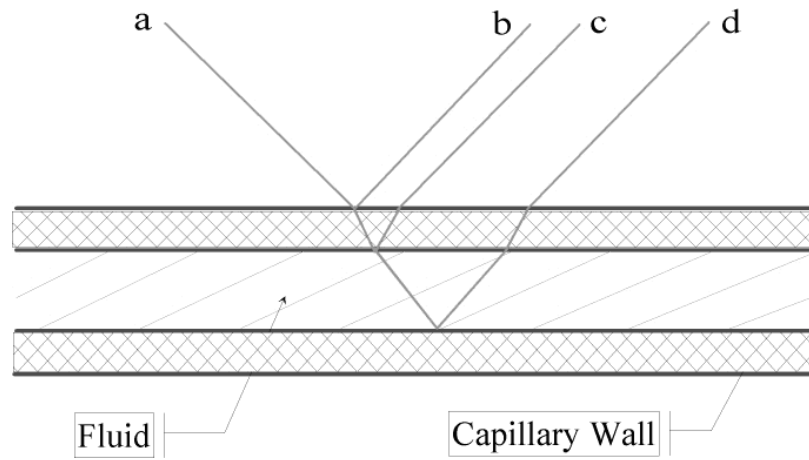


Fig. 5.1. Simplified ray trace of the light path through a capillary scale channel from the side view.

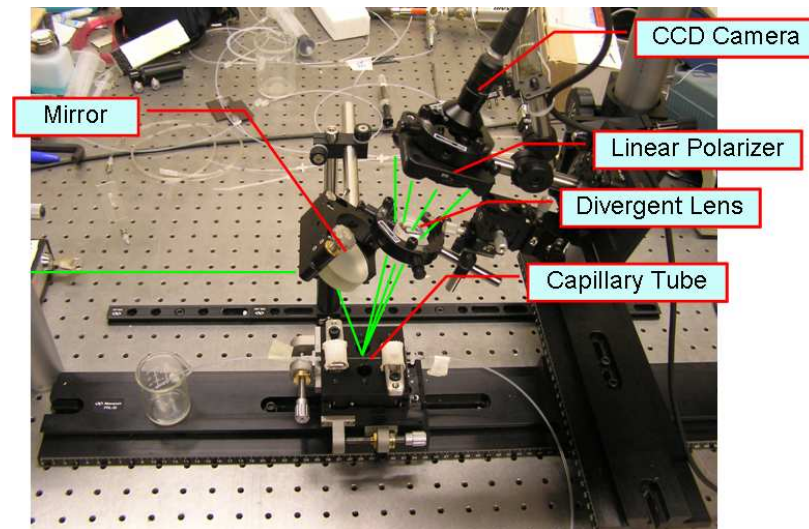


Fig. 5.2. Capillary tube and fringe acquisition apparatus showing beam behavior as series of green lines superimposed on the image.

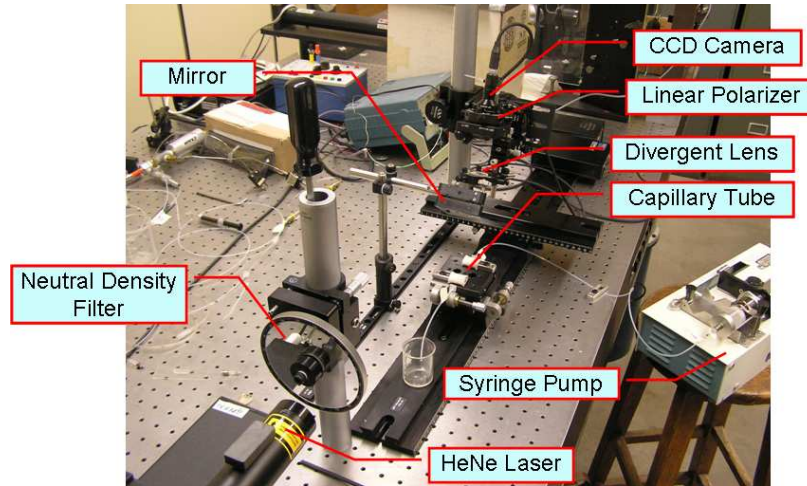


Fig. 5.3. Experimental apparatus used in flow testing.

These detectable variations are caused, in part, by a minute pressure drop over the length of the channel, created by the flowing liquid. This pressure change can be described mathematically using the Hagen-Poiseuille solution for steady, incompressible, laminar flow and will be expanded upon in Section 7.1.

The camera output was recorded using a PC and an EPIX framegrabber in XCAP for Windows, an image analysis program. The video frames for each test were saved as a series of .tif images to be processed and examined later in more detail. The post processing techniques used in the analysis of this data are left for discussion in Section 6.2.

5.2 Experimental Parameters - Thin Walled Channels

The primary experimental apparatus used in testing of thin walled channels has been described in Section 5.1, however, there are several characteristics specific to the testing technique used on these channels. First, fluid flow was used in all thin walled channel testing to induce pressure gradients caused by pumping a fluid through the system. In all flow testing described here the working fluid was distilled water at room temperature, however, silicon oil was also used producing similar results. The system was aligned by tilting the mirror over the channel (shown in Figure 5.2) until the top and bottom channel reflections were observed to overlap. This typically required an impingement angle less than 30° depending upon channel size since smaller channels result in much closer reflections. The CCD camera was mounted on an adjustable arm to allow interrogation of the entire backscattered arc and was typically placed within twelve inches of the channel impingement point.

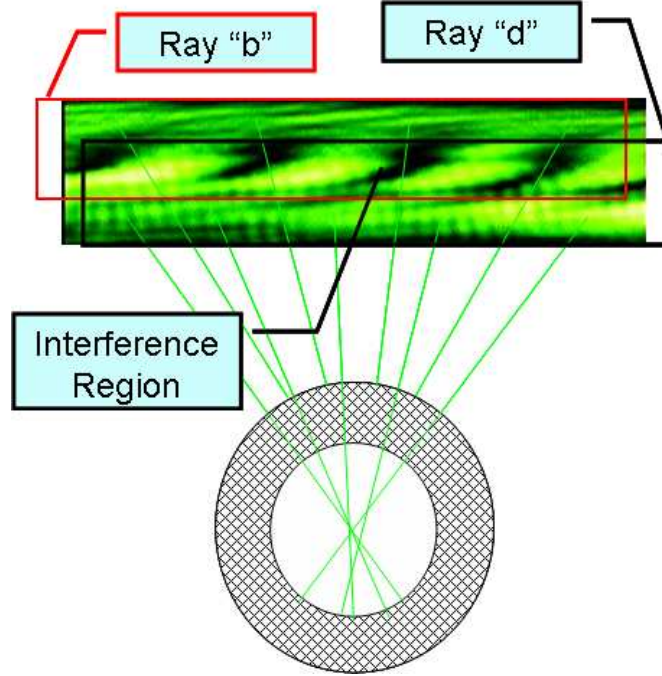


Fig. 5.4. Formation of fringes caused by primary reflections from glass surface at top and inner wall of a capillary tube (rays b and d from Figure 5.1).

5.3 Experimental Parameters - Thick Walled Channels

Next, modifying the experimental apparatus to study fringes produced by thick walled channels (both round and square cross-sections) completed the adaptation of the device from the original MIBD apparatus to achieve pressure measurements. The optical train remained virtually unaltered with the exception of the channel which required camera and impingement angle changes. Due to startup issues with the green HeNe laser, a comparable 1.5 mW red HeNe laser with 633 nm wavelength was used during some of the testing of thick walled channels. This modification causes minor changes in the results, but has no unique effects on the apparatus itself. To perform testing on thick walled channels where deflection was drastically reduced, both flow and static tests were performed. For flow testing, the channel was plumbed using flexible Tygon tubing which was stretched over the inlet and outlet ports to produce an air tight seal. To produce adequate fringe patterns, the impingement angle was adjusted to be between 10° and 20° from the surface normal. The divergent lens was replaced by a 5x microscope objective lens which was placed at varying distances between the channel and the CCD depending upon the desired magnification. For rectangular channels in which a backscattered arc was not produced, the camera was mounted directly in line with the plane of the beam path which was in turn perpendicular to the plane of the table. When circular thick walled channels were used, the arc was interrogated as in the case of the thin walled channels.

As stated, static testing was also performed using thick walled channels. A diagram of the experimental apparatus used in this testing is shown in Figure 5.5. Here,

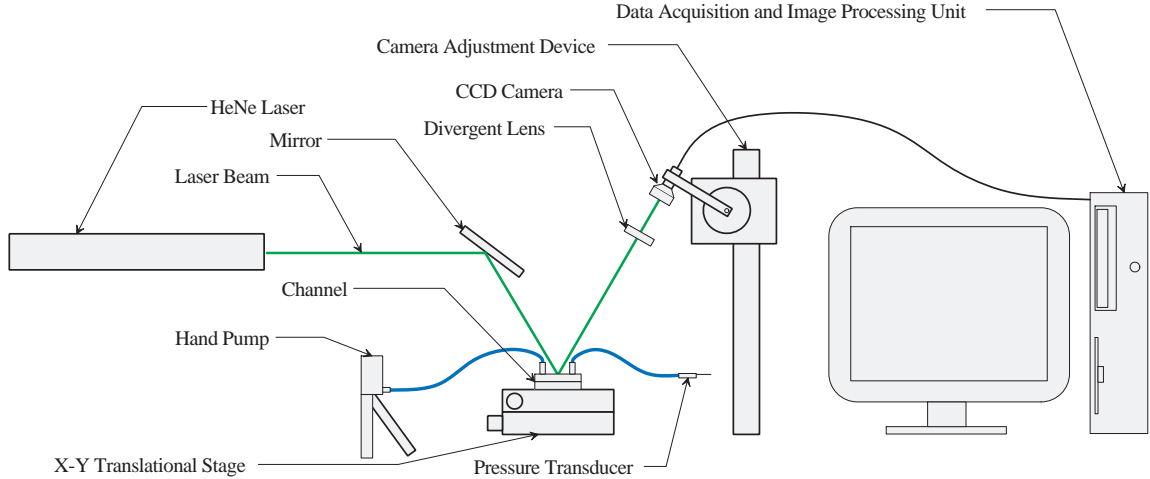


Fig. 5.5. Diagram of experimental apparatus used in static pressure tests of the thick walled channels.

a miniature pressure transducer was plumbed to the outlet of the cell and a hand pump was connected at its inlet. The transducer was wired to a Keithley 2700 Multi-meter / Data Acquisition System data acquisition system which transported data to an Excel spreadsheet in real time during testing. The calibration of this transducer was verified using an inclined manometer, the results of which can be found in Appendix B. Using the hand pump, the cell could be pressurized to a desired level to study the corresponding fringe shifts.

5.4 Fringe Formation

To better explain how the fringe formation occurs, one can first consider two beams of light as two point sources. In the case of coherent light, such as that from a laser beam, it is a good assumption to assume the light propagates as planar waves where there are equally spaced fronts of equal intensity. This scenario is sufficient to describe, for example, rays b and d from the capillary tube. Therefore, if the red point sources shown at the left of Figure 5.6 are considered to emit planar waves as shown, one can observe the interference effects between the wavefronts. As these waves are emitted, they tend to interfere with one another to form the light and dark bands, which are widest at the vertical and move closer together as they reach the horizontal. These light and dark bands are representative of the regions of constructive and destructive interference, respectively.

As described by Figure 5.4, fringes are primarily formed by the combination of light rays backscattered from the top and the bottom inner surface of the channel in the case of capillary tubes with relatively thin walls. This type of interference is primarily from two sources, although additional fringes are formed from other reflection combinations such as rays b and c or rays c and d. These interference combinations are responsible for the smaller fringes seen outside the primary interference region in Figure 5.4.

In the case of the thick walled channels, the beams are separated a significant amount and the fringe formation explanation from Figure 5.4 is no longer valid. As a result of this large separation, the backscattering angle can be increased such that the reflection from the top of the channel is no longer a part of the interferometric signal. This occurrence has been depicted in Figure 5.9 where only the reflections caused by the channel are included in the signal thus drastically simplifying the interference pattern. In the case of Figure 5.9, the fringes are arbitrarily shown as diagonal, although the orientation is heavily dependent upon beam alignment.

When compared to the image formed from the impingement of a 500 micron square capillary tube as shown in the upper right of Figure 5.6, one can clearly see the resemblance due to the common formation mechanism. The frequency of the fringes is a direct function of the source spacing; this observation will be utilized in later analysis to detect the presence of transverse channel deflection. Finally, the image in the lower right of 5.6 displays an instance where multiple source interference is dominant, causing a criss-cross of fringes in opposing directions.

From this discussion, it is made clear how fringe formation from a microchannel can become very complex depending on the alignment of the system and channel orientation. The intricacy of fringe formation in microchannels has been addressed in the literature [22], however, for this application the solutions are insufficient since the geometry of drawn glass does not have sufficient uniformity at these scales resulting in unacceptable prediction error. To illustrate the extent of this complexity, Figure 5.7 shows a variety of fringe patterns captured using several channel types and orientations. It is important to note that the red arrows represent the direction of fringe movement upon an increase in RI. The magnitude of this shift is dependent upon factors such as temperature, channel geometry, fringe magnification, fluid flow rate, and pressure. Three of the pictures shown were captured from a capillary tube of circular cross section and 1 mm inner diameter. The two on the left are from the same orientation, however, the top one is at a significantly higher magnification and has been inverted causing the fringe shift to appear in the opposite direction. The photo at the lower right is from the same channel rotated 90° to meet the MIBD impingement criteria. Although shifts are still observed, one can begin to see the clear advantages of the orientation in the adapted technique, not only for explaining fringe formation, but also in the symmetry and clarity of the fringes.

Figure 5.7 also shows fringe patterns formed by square and rectangular channels. In the case of the square channel the central fringe is shown. This fringe is important since its behavior is very close to the behavior of fringes where the beam diameter is less than the channel cross section. Correlations for this will be discussed later in this section and it should be realized that these correlations only hold for the central fringe of the backscattered arc (that fringe positioned directly above the channel) such that the parallel plate assumption is sufficient to describe the fringe behavior. Finally, the rectangular channel is constructed of optically flat, fused quartz plates and therefore creates a very uniform fringe pattern in comparison to more cost effective drawn glass channels.

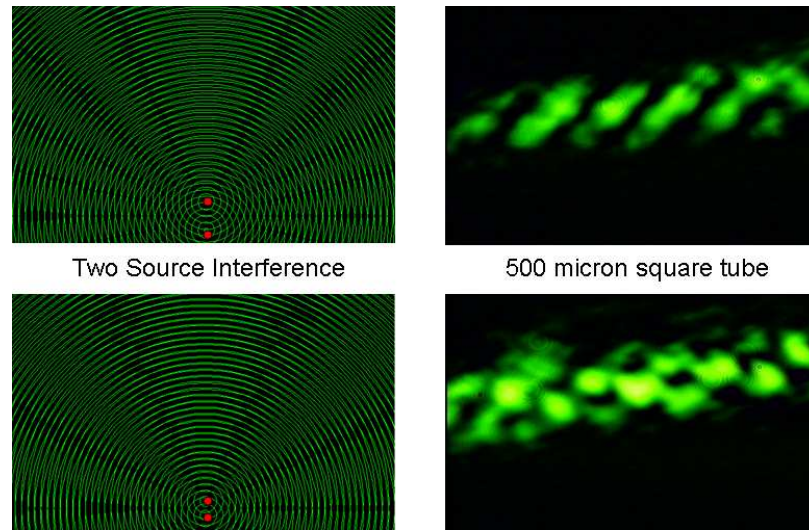


Fig. 5.6. The formation of fringes from planar light waves emitted from two sources (planar waves appear spherical at macro-scale).

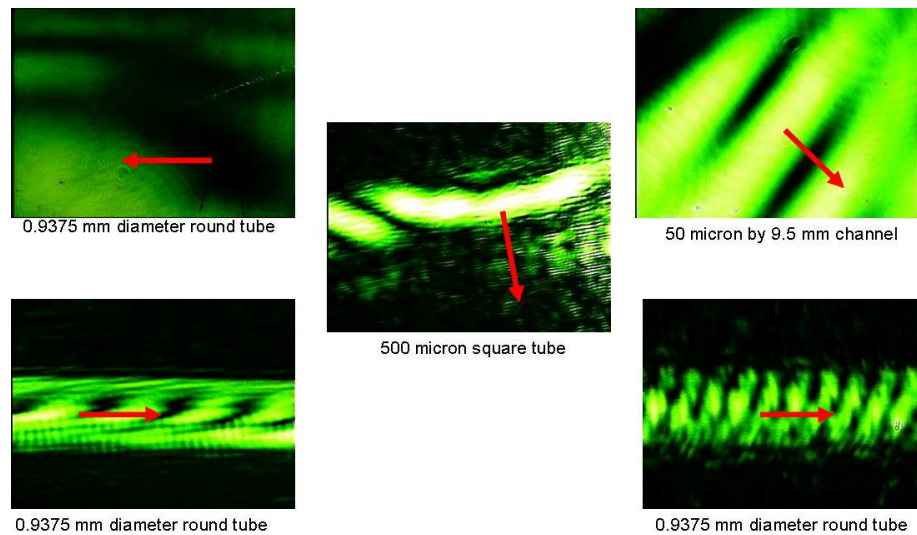


Fig. 5.7. Typical diversity of fringe types produced from different channel sizes and geometries. Note that red arrows denote fringe shift direction.

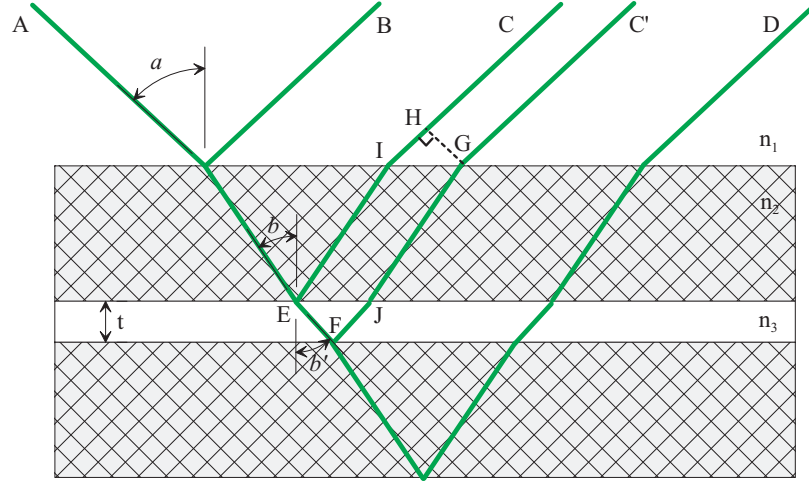


Fig. 5.8. Ray trace of a beam through the thick walled rectangular channel used in derivation of the path length difference relationship.

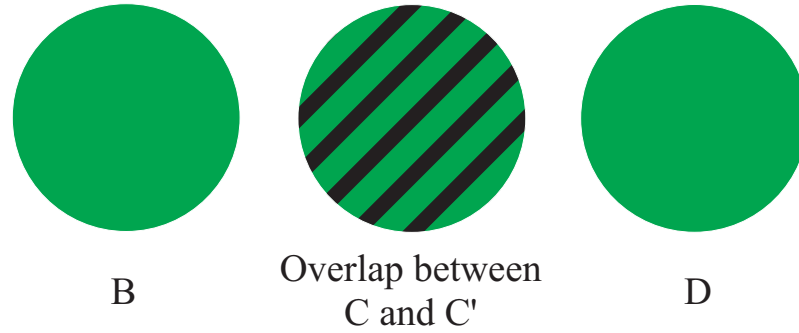


Fig. 5.9. Formation of fringes from the thick walled channel shown in Figure 5.8

5.5 Geometric Path Length Derivation

As described in previous chapters, knowing the path length difference of the light is critical in the quantification of fringe shift information. The most general expression for path length difference, Equation 2.3, utilizes a fringe shift to describe the changing phase or light path, referred to as the change in path length difference, $\Delta\delta$. However, if quantification of RI or channel deflection are desired, a more detailed understanding of light ray behavior is required. Figure 5.8 gives a comprehensive explanation of the primary path of a laser beam through a thick walled channel. It will also be observed later that internal reflections (like those in the Fabry-Perot configuration or etalon) play a role in the formation of the fringe pattern.

Snell's Law is commonly used to describe the refraction of light caused by a change in RI as light travels between two mediums of differing optical densities. Considering one medium is of refractive index n and the other is of refractive index n' , one can relate the angles formed by a ray of light at the material interface by the following equation:

$$\theta' = \arcsin \left(\frac{n'}{n} \sin(\theta) \right) \quad (5.1)$$

Where θ and θ' are measured from the surface normal. Applying Snell's law to the air-glass interface in Figure 5.8:

$$a' = \arcsin \left(\frac{n_2}{n_1} \sin(a) \right) \quad (5.2)$$

Using Figure 5.8 once again we may calculate the path length difference δ between rays AEIHC and AEFJGC' geometrically. By observation, one can determine that rays C and C' are identical until point E where they separate. In addition, by further inspection, it can be agreed upon that the difference in phase between rays C and C' is constant after point H on C and point G on ray C'. Therefore, the difference in phase can be determined by the physical path length difference between these locations. In terms of geometric ray segments this can be described as

$$\delta = (n_3 EF + n_3 FJ + n_2 JG) - (n_2 EI + n_1 IH) - \frac{\lambda}{2} \quad (5.3)$$

where the $\lambda/2$ term is a result of a half wavelength advance in phase experienced by the longer leg due to a reflection from a surface of higher RI than the current medium [8]. This phase shift effectively lowers the phase difference since it occurs on the slower leg and therefore appears as a negative term in Equation 5.3. Considering that EI and JG are of equal length, these paths are found to cancel. In addition, since n_1 is air in this case, it can be assumed to be very close to one. Finally, since EF is of equal length to FJ, Equation 5.3 simplifies to:

$$\delta = 2n_3 EF - IH \quad (5.4)$$

Since the segments are related to the thickness of the channel, t , they can be calculated geometricly and are found as follows.

$$EF = \frac{t}{\cos b'} \quad (5.5)$$

$$IH = IG \sin a \quad (5.6)$$

$$IG = 2t \tan b' \quad (5.7)$$

Where IG is observed to be of equal length to EJ which is twice the geometric length of the projection of segment EF onto the inner surface of the channel. Substituting 5.7 into 5.6 and placing this result along with 5.5 into 5.4 we find

$$\delta = \frac{2n_3 t}{\cos b'} - 2t \sin a \tan b' - \frac{\lambda}{2} \quad (5.8)$$

Upon recognition of that fact that $\sin a$ is equivalent to $n_3 \sin b'$, the trigonometric identity $\sin^2 b' + \cos^2 b' = 1$ can be used to simplify Equation 5.8 to the following form.

$$\delta = 2n_3t \cos(b') - \frac{\lambda}{2} \quad (5.9)$$

Equating 2.3 with 5.9 and simplifying:

$$\Delta m = \left| \left(\frac{2n_3t \cos(b')}{\lambda} \right)_1 - \left(\frac{2n_3t \cos(b')}{\lambda} \right)_2 \right| \quad (5.10)$$

Where the subscripts denote an initial and final state before and after the fringe shift event. As a result, a dimensionless fringe shift, Δm , can effectively be correlated to changes in channel geometry and RI. It should be noted that the angle b' in Equation 5.10 depends on the value of n_3 and therefore the equation cannot readily be written explicitly for a value of the RI. As a result, the solution is often solved for numerically, as will be done in Chapters 7 and 8.

6. DATA PROCESSING PROCEDURES

6.1 *Counting Fringes*

To quantify fringe shift information into pressure, flow rate, and deflection values, it was required that the fringes be accurately counted and measured. Interferometric fringes are related to the physical path length difference of the light, δ , such that each fringe represents a half wavelength path length difference. Traditionally, when counting fringes, quantification is performed by counting the number of fringes to pass a given point on the observation screen over time. Using this method, the observer counts only light or only dark fringes, resulting in a path length measurement to the nearest fringe or nearest wavelength of the light being used. In the case of monochromatic light, such as that of a laser, the wavelength of the light can confidently be assumed to be a single value. In the case of the experiments performed here, a green HeNe laser with a wavelength of 543 nm and a red HeNe laser of wavelength 633 nm were used. Therefore, each fringe to pass a chosen point on the screen represented a physical path length difference equal to 633 nm or 543 nm depending upon the laser used.

Since the fringe shifts observed were very small (often less than one fringe) it was important to quantify this shift value and divide it by the width of a light and dark fringe. Doing this not only allowed for non-dimensionalization of the fringe shift, but also allowed for quantification of Δm , the number of fringes to pass an observed point over time. The widths of subsequent light and dark fringes were used since camera contrast and brightness could be adjusted such that one fringe is much wider than the other. For example, if the camera is adjusted such that the light fringes are much wider than the dark ones, then each light and dark fringe no longer represent $\lambda/2$, however, their sum is still physically representative of λ , the wavelength of the light. Therefore, during the fringe counting portion of the data collection and analysis, it was important to quantify both fringe thickness and shift. The fringe morphology was captured using a CCD camera and framegrabber and the data was quantified using pixel values. The number of fringes to pass a chosen point is then the dimensionless quantity of the fringe shift in pixels divided by the fringe thickness, also measured in pixels. Although digitization of the images makes it easy to quantify and post process data, it places limitations on this quantification based on the number of pixels used. This will be discussed further in Section 9.3. The data was processed using primarily two methods which will be discussed in the following sections.

6.2 Fringe Tracking in Spotlight

To post process the fringe shift data of early experiments, a program developed at the NASA Glenn Research Center, Spotlight 1.2, was used. This program is able to filter out undesired pixel intensities and track a region of preferred intensity across the screen as in the case of the laser interference fringes. Since the glass channels used in these experiments were made of drawn glass, they were not optically flat which resulted in an asymmetric interference pattern as seen in Figure 6.1. This problem was overcome using a series of pixel filtering options in Spotlight 1.2. First, the image was blurred twice, then it was smoothed and finally a threshold was performed to split the screen into essentially two pixel intensities, light and dark (Figure 6.3). This light to dark transition, the threshold between the regions of constructive and destructive light interference, can easily be tracked by spotlight. Processing the data in this manner helped eliminate the speckle noise and asymmetry at the threshold, giving a smoother line and thus increasing the accuracy of the tracking process. To track the fringe threshold, eight areas of interest (AOI) were used. These AOI's were set to follow a line in the direction of the fringe shift (horizontal in the case of Figures 6.2 and 6.3) and record the pixel value of the center of the box, also the light to dark transition line, after each frame. The tracking results were output as a text file providing the pixel location of the light to dark transition, essentially tracking the fringe movement over time. Since the data was recorded in a series of .tif images and the frame capture rate was known, the fringe movement data could easily be related to shift velocity, creating a fluid acceleration and velocity measuring device.

This technique, unfortunately, is very time consuming to implement. Each area of interest must be manually placed on the image, a process sequence of blurring and smoothing (low pass filtering) must be applied, and finally an intensity threshold must be specified. This leaves a great deal of room for error in selecting identical parameters between tests since there is no simple way to ensure they are the same. Finally, this method gives little insight as to what type of fringe morphology is occurring and only effectively tracks eight of 480 rows and two of four possible fringe edges.

6.3 Fringe Tracking in Matlab

The new fringe tracking method required fast, autonomous, and reliable processing in addition to the ability to observe the morphology of all parts of each fringe in an image. To do this the Matlab image processing toolbox was used to create a program to loop through each image in a tagged image file (.tif) series. In setting up an automated tracking program, each image in the file could be processed in the same manner. In addition, each test (resulting in a series of images) could be processed in the same manner since the processing options were directly accessible to the user. This method is already a great benefit over previous methods since it allows the user to choose processing parameters with greater precision, processes each set of images exactly the same, and less time is required since the user only has to specify the parameters once for the program to execute indefinitely.

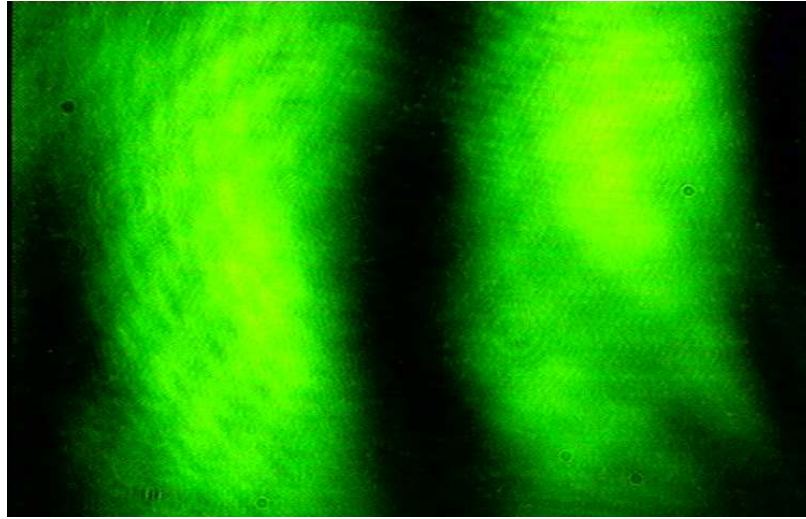


Fig. 6.1. Typical fringe pattern captured from a 500 micron square glass capillary.

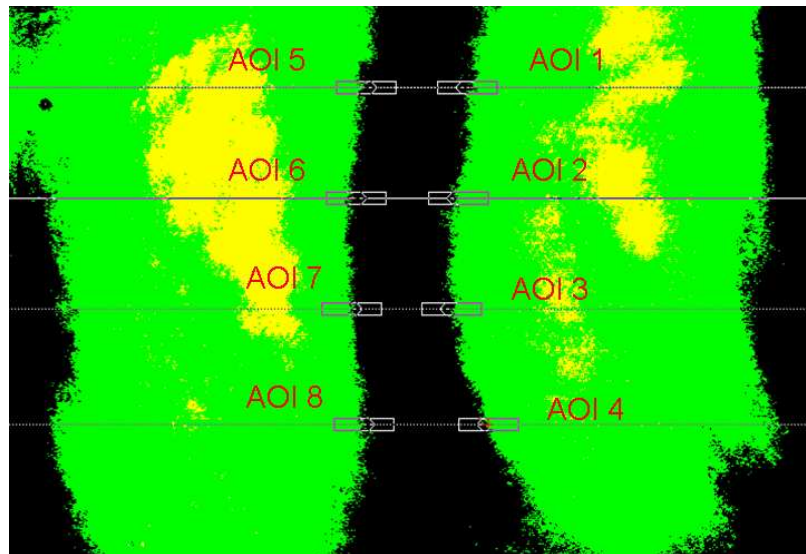


Fig. 6.2. Eight areas of interest manually placed on the intensity threshold used for interface tracking in Spotlight.

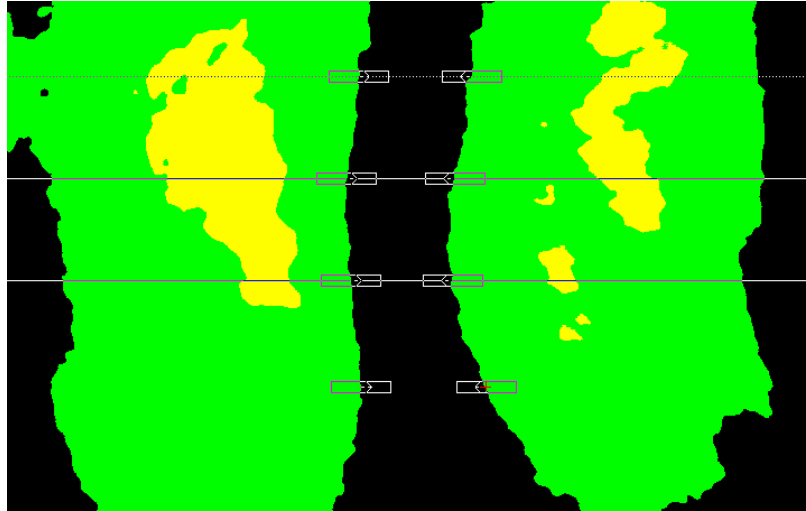


Fig. 6.3. Filtered fringe image used to smooth laser speckle at edges and increase tracking accuracy.

The flow of this tracking procedure is represented in Figure 6.4 where the original image was changed to a grayscale image, filtered using a Gaussian low pass filter and then changed to binary using an intensity threshold function. The original image was 8 bit RGB, as a result it is constructed of three matrices (one for each color) with sizes corresponding to the number of pixels in the image. Since a CCD camera was used, pixel saturation overflowed to surrounding pixels, a characteristic common in CCD sensors, thus the red and blue components contained some intensity information as well. Rather than discard this information and process only the green matrix (since green light was used), the image was converted to a single 8 bit grayscale image, a much faster alternative than processing all three matrices separately.

To eliminate the noise and high frequency content present in the grayscale image, it was converted into the frequency domain via the fast fourier transform (FFT). This was necessary since the rough edges of the fringes have continuously been problematic for accurately tracking the shift and shape change of these types of fringes. It is not evident from the photos, but when the images from a test are combined into a movie the camera interlacing causes this rough area to move much like static on a television screen making accurate tracking nearly impossible. When a low pass filter is multiplied by the FFT, the high frequency noise in the images is attenuated leaving only the two bright areas of interest as shown in Figure 6.4. The program which performs these tasks and ultimately tracks the movement of these fringes is available with full commenting in Appendix F and an alternative version used in static pressure testing can be found in Appendix G.

Performing the FFT on the grayscale image involves the use of the 2D FFT. This uses the same principles as taking the FFT in one dimension. Matlab performs the FFT of each row in an image and replaces that row with the FFT vector. It then takes the FFT of each column in the image, essentially completing the FFT of all the FFT results from the other direction one frequency line at a time. The result of

this process is clearly shown in Figure 6.5 where the grayscale image shown in the upper left is “moved” to the frequency domain via the FFT. At this point the FFT is un-centered; this means that frequency is highest at the center and decreases in any direction outwards toward the corners where it is lowest. The image is displayed in this manner simply due to the math required in performing the discrete fourier transform (DFT) and the placement of the origin for the displayed image. For ease in viewing, the FFT is then shifted to the center meaning the origin, or point of zero frequency content, is at the center of the FFT image and frequency increases as one diverges from this point.

This image, shown in the lower right of Figure 6.5, gives a great deal of insight on what is occurring in the spatial image. Noting that the image is split into four quadrants with the first being positive-positive and the others following mathematical sign convention, one can determine how many of the features of the FFT relate back to the original image. Most importantly when viewing the zoomed area from the center of the image shown in the lower left of Figure 6.5, one can see two bright pixels along the horizontal axis. These bright spots denote a great deal of energy and are caused by the two fringes in the image, the dominant frequency in the horizontal direction. This observation is determined by drawing an arrow from the center of the FFT to the point of interest. Since the arrow is horizontal it shows that this frequency occurs in the horizontal direction, and since the spots are very close to the center, it is known that they come from a very low frequency. Another feature of interest is the lines on the FFT which can be explained by leakage present in the image since the frequencies present are far from periodic with respect to the image size. The concept of leakage refers to the need for high frequencies to reproduce events in an image which are non-periodic with respect to the image dimensions. Finally, the light spots located at different areas on the FFT can be related to the frequencies of the lighter lines present in the fringes themselves. This can be verified by once again drawing a vector from the center of the FFT to these spots; the direction of this line provides the direction of the frequency content in the image. This subject will be covered in greater detail in Section 6.4.

Once the FFT has been analyzed for energy content, a low pass filter just outside the frequency of the fringes in the image eliminates all the unnecessary frequency content in the image. This low pass filter, shown in Figure 6.6 (both in 2D and 3D) is sized using the distance of the frequency of interest as a percentage of the total image size. The filter is a Gaussian distribution and its size and sharpness are controlled in terms standard deviations from the center of the filter. In short, fewer standard deviations give a smaller filter. The low pass filter essentially acts to blur the image, resulting in the filtered image shown in the lower right of Figure 6.6. This image is ideal for tracking since its histogram is highly sinusoidal in the horizontal direction and can be given sharp edges using a threshold function.

Once the image is properly filtered, a threshold value is assigned to it based on the range of pixel intensities present. Matlab can be configured to calculate this threshold value automatically, further automating the program and improving it against the use of a slider bar in the past method which proved to be inconsistent. The binary image is the final point in the image processing cycle and at this point the fringes are tracked

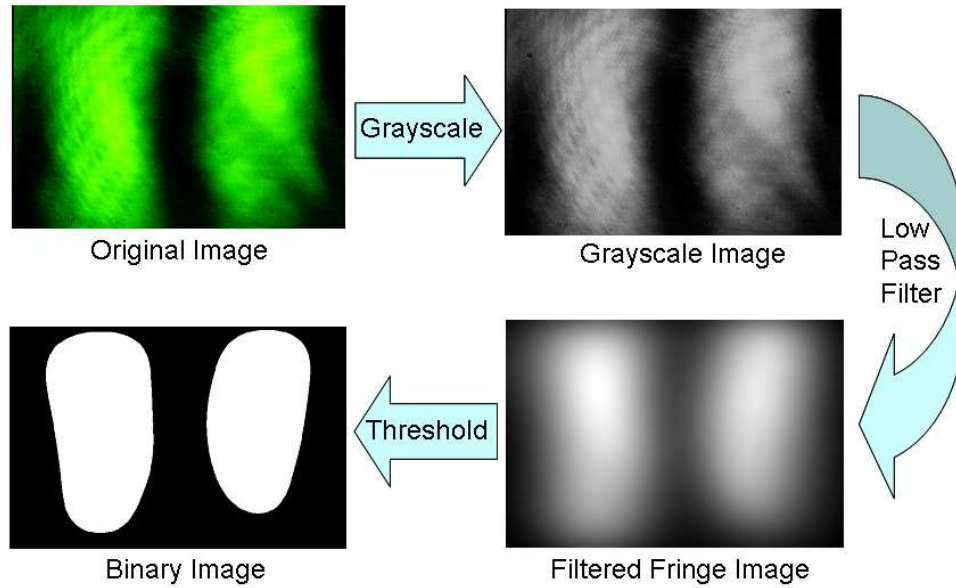


Fig. 6.4. Flow of image processing which occurs in the program to prepare fringe images for tracking.

through each frame.

To track the fringes, a series of “if” statements were used to find the indices where the image turned from black to white and from white to black. These “if” statements are placed within a series of “for” loops to search for the edges of the fringes in each frame. Using this data for each frame, the shift and thickness of each fringe in the image can be calculated. For more detail on Matlab syntax utilization, fully commented versions of the codes used in fringe shift tracking can be found in Appendices F and G.

6.4 Relating the FFT to Spatial Images

One interesting and useful feature of the FFT is that periodic features, such as fringes in the case of this project, can be related to points or groups of points in the frequency domain (leakage appears as lines, usually of varying intensity perpendicular to their direction). As shown in Figure 6.8, the periodic lines which construct an image have very predictable FFT results. As in the case of the fringe FFT analyzed earlier containing two small bright spots and a series of larger dimmer spots, the slanted lines cause a series of dots at a given frequency on the FFT. To relate this data to the images, several different patterns and their FFTs have been included. To find how a feature of the FFT relates to its corresponding image, a vector can be drawn for the zero frequency point (origin) to the point of interest. As was the case in Figure 6.5 of the actual test data, the magnitude and direction of this vector directly correspond to the size and direction of the feature of interest in the image. More specifically, the FFT is divided into four quadrants which follow standard mathematical sign convention. The axes represent frequency in the horizontal and vertical directions

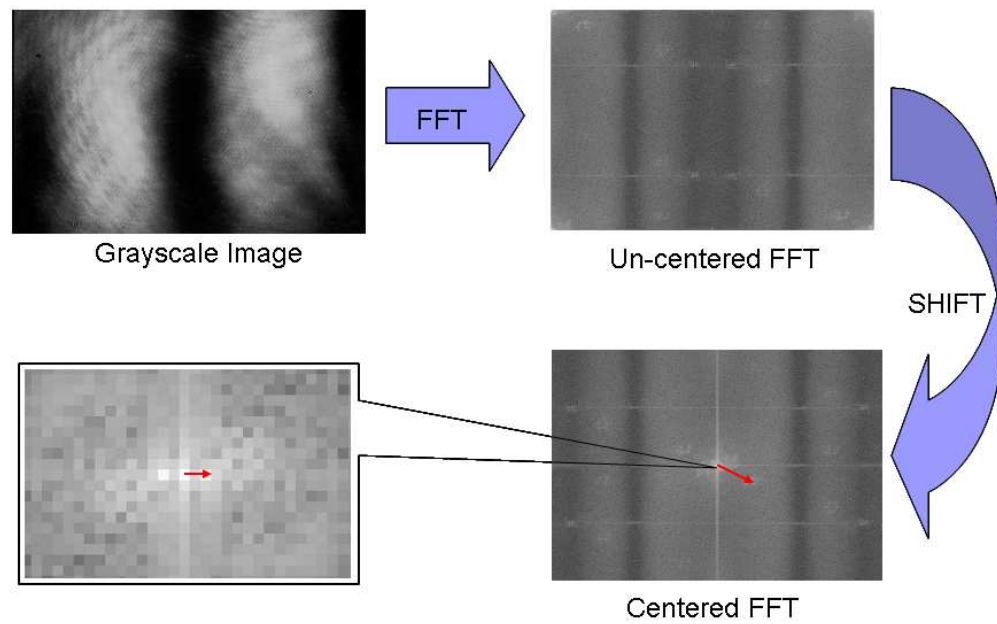


Fig. 6.5. FFT produced from the grayscale image. The centered FFT is characterized by low frequency content at its center. Upon zooming of this area one can distinguish the energy (white spots) associated with the fringes.

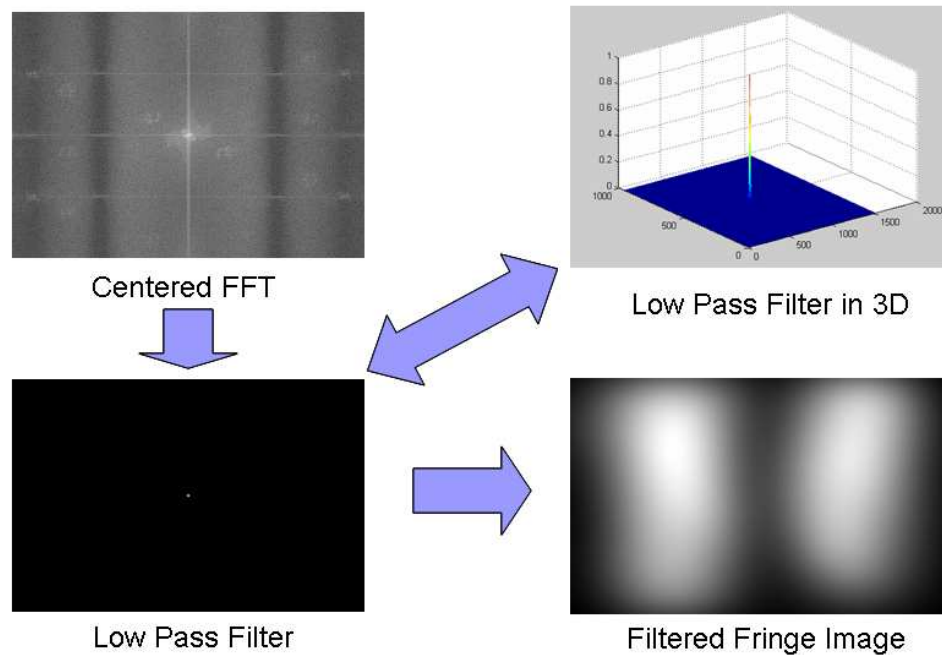


Fig. 6.6. Multiplication of FFT and Gaussian low pass filter in the frequency domain resulting in a filtered fringe image. Note that the filter is shown in both 2D and 3D for ease in viewing.

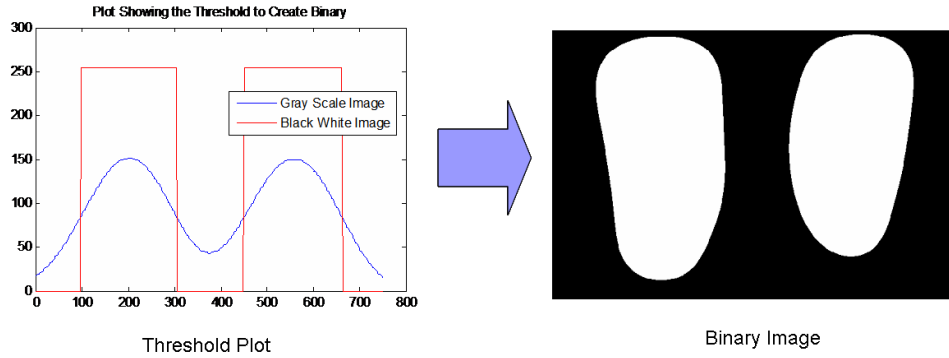


Fig. 6.7. Threshold of filtered image set at about half the range of intensities present. The eight bit images have pixel intensity values of zero to 255, thus all areas above the max threshold value are set to white (255 in the case of eight bit and one in the case of binary) resulting in the black and white image shown at the right.

with up and right being positive as previously stated.

Assigning a meaningful number scale to the frequency axes can be simple when the image dimensions and feature sizes are known. This method was examined, however, it was not implemented in this research since feature sizes are a function of magnification and it is more convenient to size the filter based on the position of the dominant frequencies in the FFT. Using this method, the numerical value of the frequency is not necessary thus simplifying the process of determining the filter size to properly process an image. From Figure 6.7, it is shown from a histogram of one row of the filtered fringe image (lower right of Figure 6.6) that the frequency has been reduced to that of the fringes within the image. This is confirmed by the sinusoidal nature of the histogram which presents waves of equal period and amplitude. Since only this frequency is present, only the information used in creating the two prominent fringes remains in the image. Therefore, when tracking the movement of these fringes in a video, the effects of speckle noise and secondary reflections is eliminated resulting in more accurate fringe position quantification.

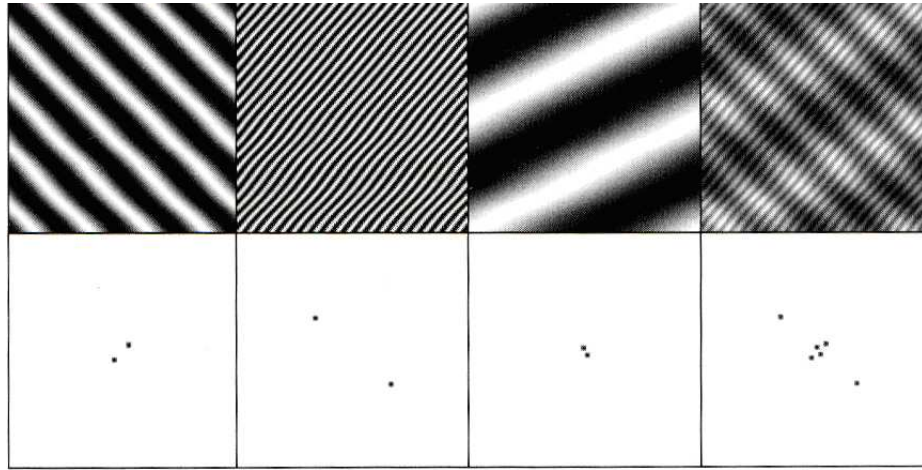


Fig. 6.8. Generic line patterns and their corresponding FFTs. The pattern at the right is a sum of the previous three showing the frequency domain result of having periodicity in three directions [4].

7. EXPERIMENTAL RESULTS

Experiments were performed under a variety of conditions using channels both wider and narrower than the diameter of the laser beam. A full listing of the channels tested is provided in Table 7.1. Results were found to show similar data trends where deflection of the channel walls played the largest role in the differences in sensitivity and detection capabilities. To isolate channel wall deflection, a variety of thick and thin walled channels were used with channel cross-sectional dimensions both larger and smaller than the laser beam diameter. Thick walled cells were defined as having wall thicknesses greater than 1 mm. The results observed from testing of each type of channel are reported in the following sections.

7.1 *Channel Cross-Section Less than Beam Diameter*

7.1.1 *Capillary Tubes*

Using the flow rates calculated from the pump speed at each flow rate selection, the pressure drop across the channels could be estimated using the Hagen-Poiseuille formulas for circular and rectangular channels (equations 7.1 and 7.2) [23]. The linear pump speed was verified under load using length and time measurements to an accuracy of 0.1 mm and 0.1 second, respectively. The results of this verification, provided in Appendix A, proved the pump manufacturer's flow rate chart was incorrect for the syringe in use, but allowed for the calculation of actual flow rate values through the system based upon syringe dimensions from the manufacturer (Hamilton Co.).

Equations 7.1 and 7.2 describe the flow rate to pressure relationship within the system using both round and rectangular channels [23]. In this case, Q represents the volumetric flow rate, R is the inner channel radius, μ is the dynamic viscosity of the liquid, ΔP is the pressure change over the length of the channel, and l is the channel length. In the case of Equation 7.2, a and b are the nominal inner dimensions of the rectangular channel where a represents the width and b represents the height.

$$Q = \frac{\pi R^4}{8\mu} \frac{\Delta P}{l} \quad (7.1)$$

$$Q = \frac{4ba^3}{3\mu} \frac{\Delta P}{l} \left\{ 1 - \frac{192a}{\pi^5 b} \sum_{i=1,3,5}^{\infty} \frac{\tanh\left(\frac{i\pi b}{2a}\right)}{i^5} \right\} \quad (7.2)$$

Using the experimental procedure described in Sections 5.1 and 6.2, the apparatus is able to detect average flow velocities as low as 1.8388 mm/sec in a round capillary tube of 0.9375 mm inner diameter and 0.1317 mm/sec in a 500 micron square capillary

Tab. 7.1. Various channel cross-section geometries and sizes used in testing.

Geometry	Inner Dimension	Outer Dimension
Square	0.20 mm	0.40 mm
Square	0.50 mm	0.80 mm
Square	1.00 mm	1.60 mm
Square	0.25 mm	4.00 mm
Circular	0.3410 mm	1.0947 mm
Circular	0.3410 mm	1.0947 mm
Circular	0.9375 mm	1.3868 mm
Circular	0.008 in	0.250 in
Rectangular	9.00x0.05 mm	12.50x2.60 mm
Rectangular	9.00x0.10 mm	12.50x2.60 mm
Rectangular	9.00x0.50 mm	12.50x3.00 mm
Rectangular	9.00x0.05 mm	12.50x10.00 mm

tube. These velocity detection limits are defined as the fluid velocities at which the fringe shift magnitude (in pixels) overcomes the experimental shift error of plus or minus two pixels; other errors affecting the detection limits will be described in Section 9.1. The detection limits correspond to pressure drop values of 6.7 Pa for the round capillary and 0.094 Pa for the square capillary using Equations 7.1 and 7.2, respectively.

Before the sensitivity of this technique can be put to use, the predictability of the fringe shifts must be refined to provide a much smaller experimental error, namely, channel deflection and fringe formation must become more predictable. It has been shown that different flow rates can be detected using the movement of interference fringes [24], however, the repeatability and predictability of the technique have always remained a problem. A series of tests were performed using the described procedure for flow rate testing on a square channel to better quantify the shift effects when flow was introduced. The shift results for three separate test sequences performed on a 500 micron square capillary tube are shown in Figure 7.2. This plot depicts the physical fringe shift to flow rate relationship expressed by the system at various pump speeds. It is readily observed from this plot that shift sensitivity to fluid flow rate decreases rapidly as flow rates are increased. Based upon the results of later work described in Section 7.2.2, this trend was found to be, in part, a result of channel deformation, the main cause of the spread between test sequences. The data from Figure 7.2 has been converted to a theoretical pressure drop using Equation 7.2, demonstrating an ability to achieve sub-pascal pressure resolution for this configuration.

The data points were calculated using an average pixel shift value of the eight threshold tracking AOI's shown in Figures 7.3 and 7.4. This same trend is also seen with round capillary tubes as shown in Figure 7.6. Detection capabilities differ substantially from those reported for the square channels due to differences in channel geometry and wall thickness. Table 7.2 provides a key for fluid flow velocity, as well as calculated pressure drop, based upon the flow rate settings of the pump. Here,

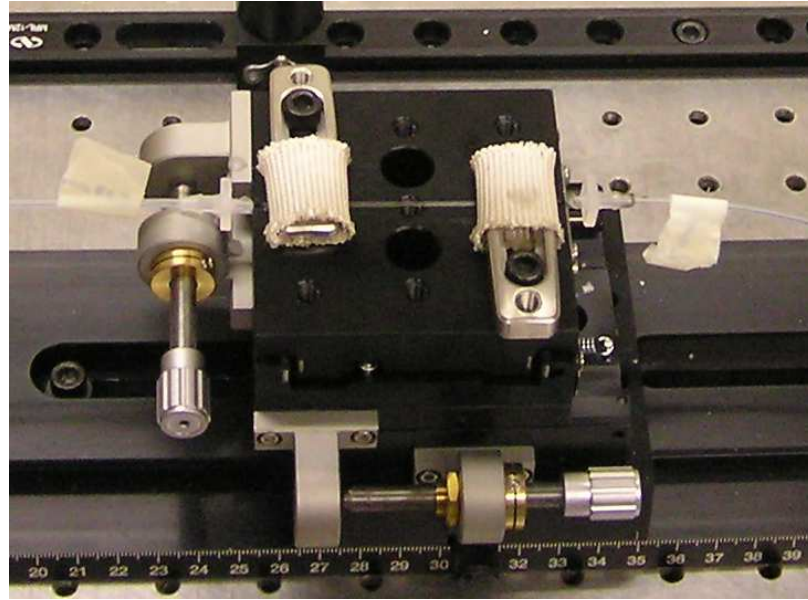


Fig. 7.1. Typical thin walled capillary tube mounted with padded clamps in preparation for flow rate testing. Note that the channel is plumbed using plastic couplers which can be melted around in the inlet and outlet of the channel. The outlet is open to atmospheric conditions to facilitate pressure estimations from pressure drop calculations.

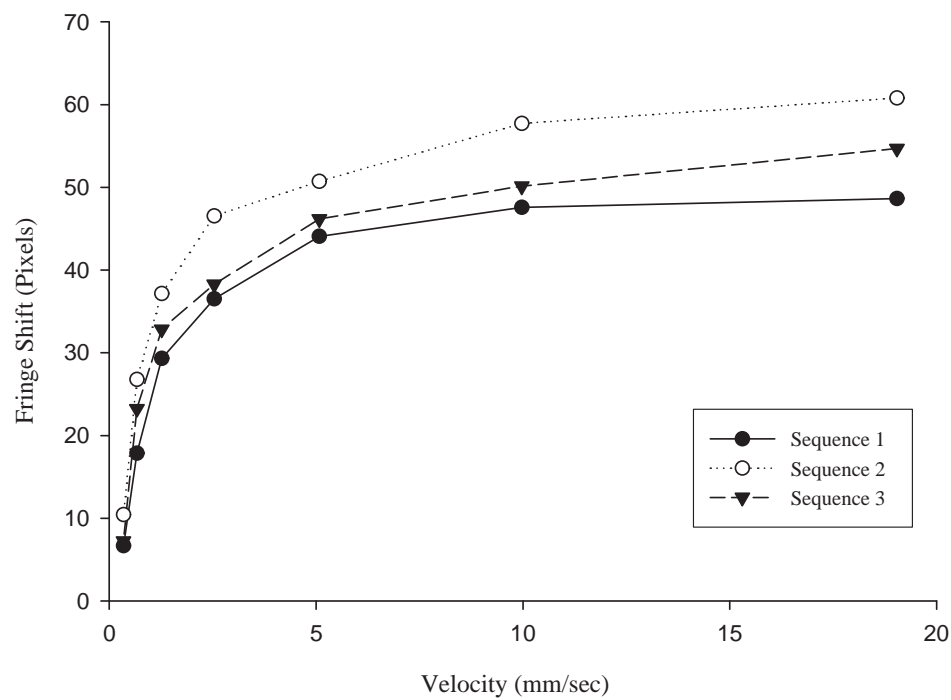


Fig. 7.2. Plot of fringe shift due to fluid flow at various velocities in a 500 micron square microchannel.

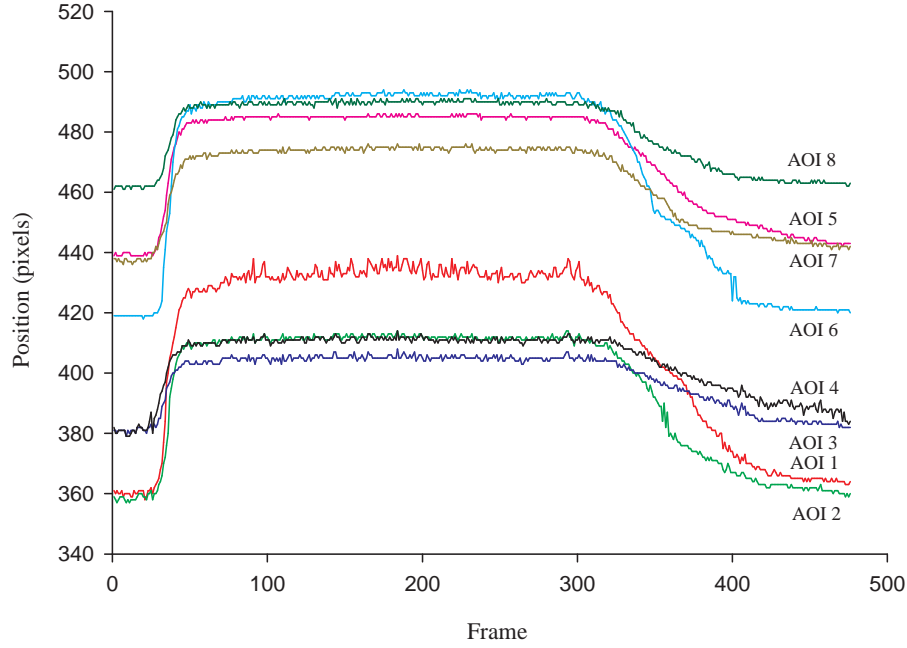


Fig. 7.3. Plot showing fringe shift tracked by the eight AOI's shown in Figure 6.2.

as in the case of the square capillary described previously, several AOI's are used to track the fringe shift. The shift values are then averaged to achieve a final shift magnitude in pixels. The results of the tracking of each of these AOI's, in addition to the their average, have been displayed in Figure 7.6 to demonstrate the difficulty in accurately quantifying pressure and flow rate using fringe shift data from capillary scale channels.

Although this data proves the feasibility of the technique in detecting flow rate, and consequently predicting pressure and pressure drops within capillary scale channels, there were several problems which required exploration before the technique could be used confidently in making flow rate or pressure measurements. First, as the fringes shift they slightly change in shape, later found to be primarily a result of channel geometry changes or deflections. The change in fringe morphology is one factor which complicates the refinement of MIBD. Data for the 500 micron square capillary, shown in Figures 7.3 and 7.4, demonstrates that as the fringes shift over time, the thickness of different areas of the fringe also change.

It is depicted in Figures 7.3 and 7.4 that the change in fringe position as a result of flow causes a significant change in fringe thickness, nearing almost half the shift of the AOI in some cases. Since this fringe morphology has low predictability, it is the goal of the following sections to isolate this effect, making pressure measurements possible.

In addition to the problem of fringe morphology in creating a predictive model for pressure measurement, other problems also complicate the adaptation of MIBD for use in pressure applications. These include the position of the camera sensor along the

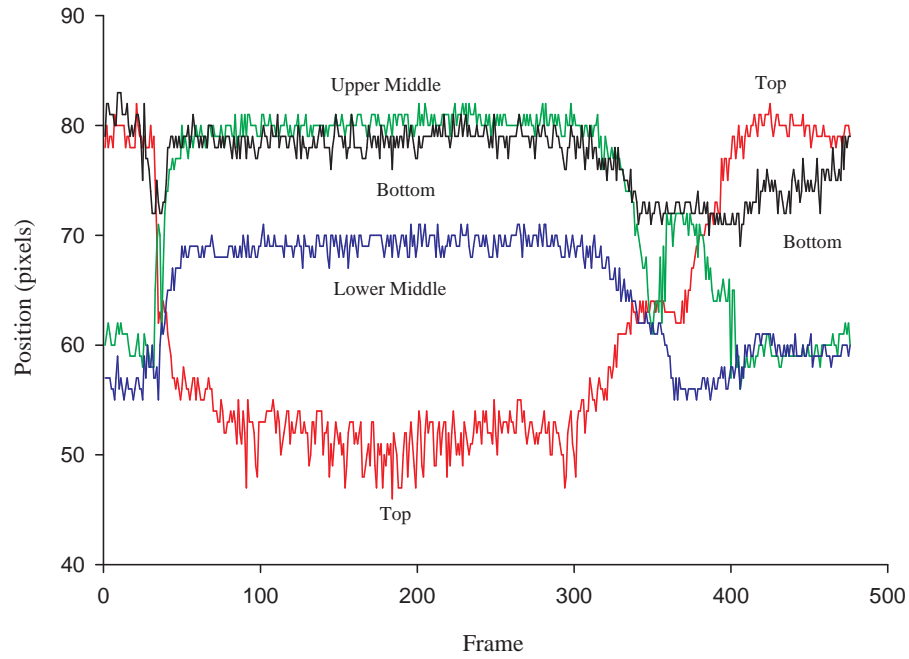


Fig. 7.4. Plot showing fringe thickness tracked by the eight AOI's shown in Figure 6.2.

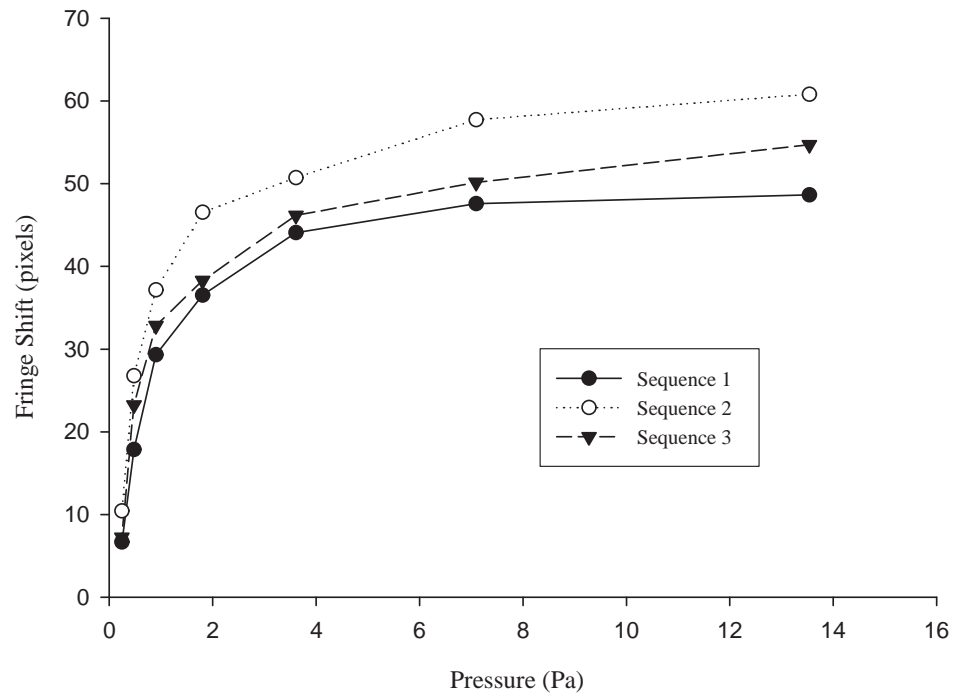


Fig. 7.5. Plot of fringe shift with respect to an implied pressure drop in a 500 micron square microchannel. Note that the outlet is open to atmospheric conditions.

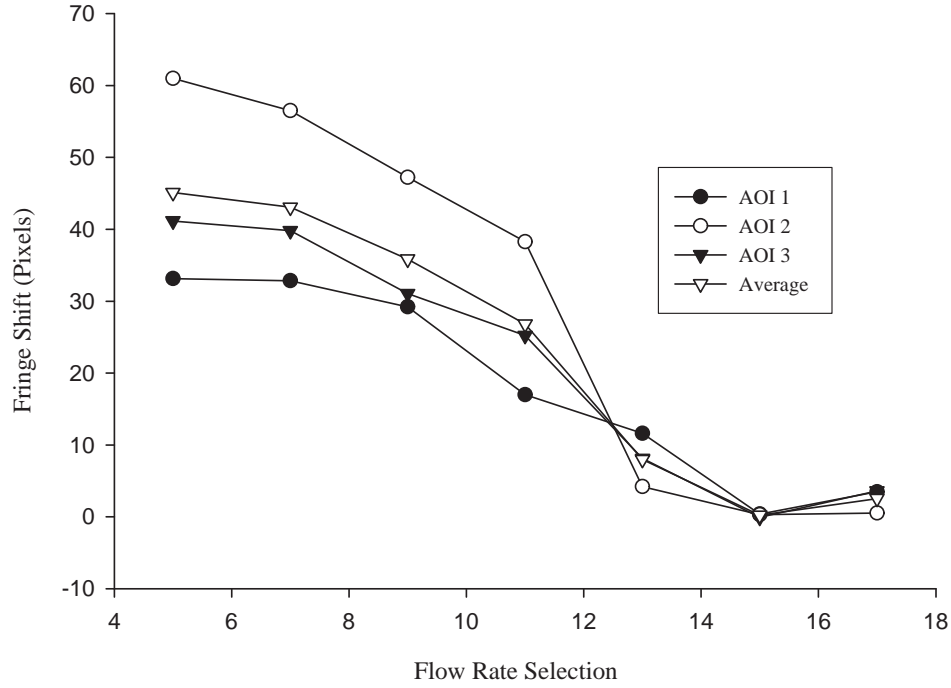


Fig. 7.6. Plot showing results of fringe tracking for three AOI's on a round glass capillary of 0.9375 mm inner diameter. The pump was not properly primed at the point where no fringe shift occurred.

backscattered arc, structural vibrations, laser intensity fluctuations [1], impingement point on the channel, optical quality of the channels, variations in pump output (Appendix A), and air currents and temperature fluctuations within the room.

To explore trends in the fringe morphology observed in fluid flow testing within square and circular capillary tubes, the Matlab program illustrated in Section 6.3 was implemented. Using this program, the entire light to dark interface was interrogated on each fringe through the duration of a shift event. For example, when considering the fringes shown in Figures 6.2 through 6.7, upon completion of the image processing procedures their edges were tracked as depicted by Figure 7.7. In this case, positions of the edges highlighted in red and green were stored for each fringe within each image or video frame (two in this case). Using this analysis, fringe morphology could accurately be monitored and quantified for each test while simultaneously tracking fringe shifts.

The results of the fringe morphology tracking are presented in three dimensional form as per Figures 7.8 and 7.9. In Figure 7.8 the shift of the interface highlighted in red in Figure 7.7 is effectively tracked through a series of 460 frames taken at a video capture rate of 3 fps. The vertical scale aligned with the image in Figure 7.7 is synonymous with the y-axis in Figure 7.8, which provides the vertical position of the fringe in pixel rows from the original image. Finally, the vertical, or z-axis, represents the magnitude of the fringe shift. From Figure 7.8 it is observed that

Tab. 7.2. Fringe shift results for flow rate selections 3-17. Areas of interest 2, 3, and 4 were placed at the top, middle and bottom of a light-dark interface, respectively.

Flow Selector Position on Pump	Calculated Velocity (mm/sec)	Theoretical Pressure Drop (Pa)	AOI 2	AOI 3	AOI 4	Average
3	788.0734	2.869E+003	42.73	58.24	60.95	53.98
5	394.0367	1.435E+003	33.15	60.98	41.15	45.09
7	203.5856	7.412E+002	32.85	56.51	39.80	43.06
9	101.7928	3.706E+002	29.22	47.22	31.05	35.83
11	52.5382	1.913E+002	16.98	38.27	25.22	26.82
13	26.9258	9.803E+001	11.61	4.20	8.12	7.98
15	13.7913	5.021E+001	0.39	0.29	-0.07	0.20
17	6.8956	2.511E+001	3.46	0.54	3.59	2.53

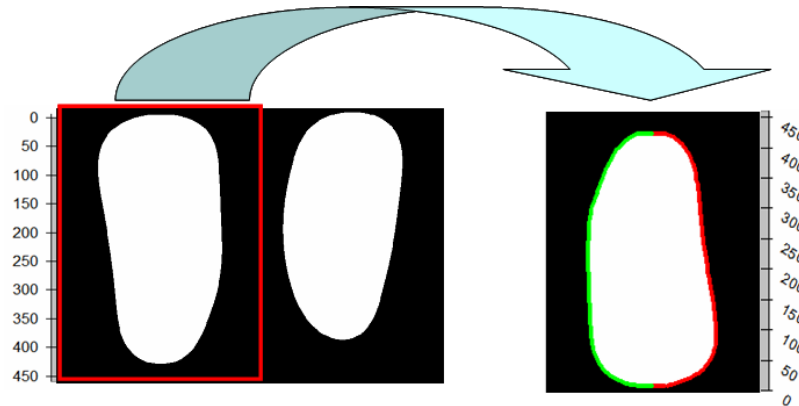


Fig. 7.7. Fringe tracked by Matlab program described in Chapter 6 to study fringe morphology. Red and green borders denote areas that are tracked by the program through each frame.

flow was initiated at frame 30 and extinguished at frame 300, as represented by the steep vertical slopes at these frame values. An interesting feature of this plot is the information it provides on fringe morphology. Upon observation of the y-axis, it can be realized that the shift magnitude decreased at lower values of the vertical position on the fringe, namely the top of the image. The large hump shown at larger vertical position values proves that the fringe shifted a significantly larger amount at the bottom than at the top. This presents an obvious problem for accurate tracking since this behavior follows the same general trend, but varies significantly in magnitude between channel types. This plot was created from a subset of the data presented in Figure 7.2 and therefore explains the large spread between the similar data trends exhibited by each test sequence.

Finally, Figure 7.9 continues to explore the fringe morphology exhibited by flow testing in these channels. In this figure, the thickness change of the same fringe

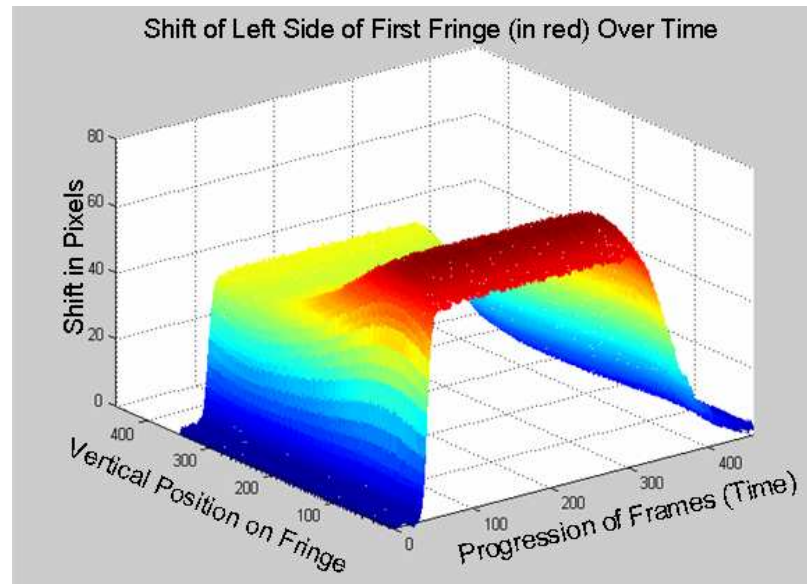


Fig. 7.8. Shift of interface shown in red in Figure 7.7 through a series of 460 frames. The z-direction shows the magnitude of the fringe shift. Flow was initiated at frame 30 and extinguished at frame 300.

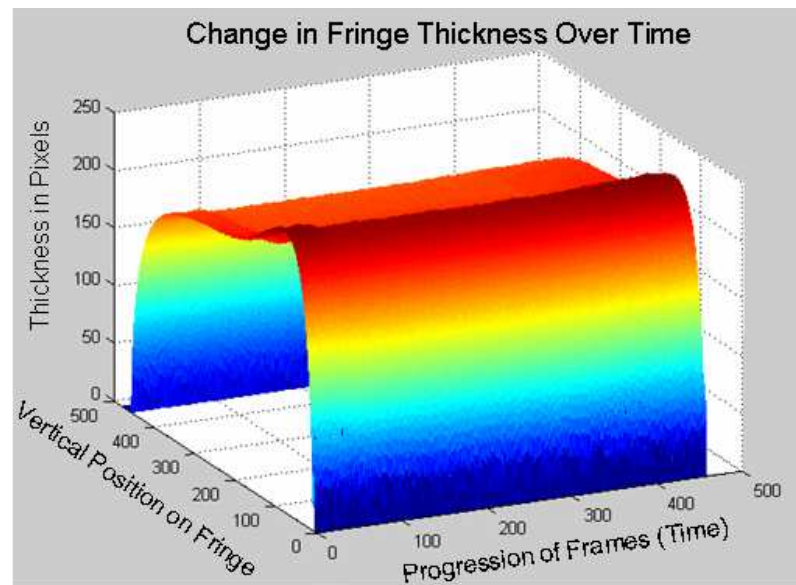


Fig. 7.9. Thickness change calculated from the difference between interfaces shown in red and green in Figure 7.7. The z-direction shows fringe thickness which decreases as the pump is initiated at frame 30 and increases to the original values and the pump is extinguished.

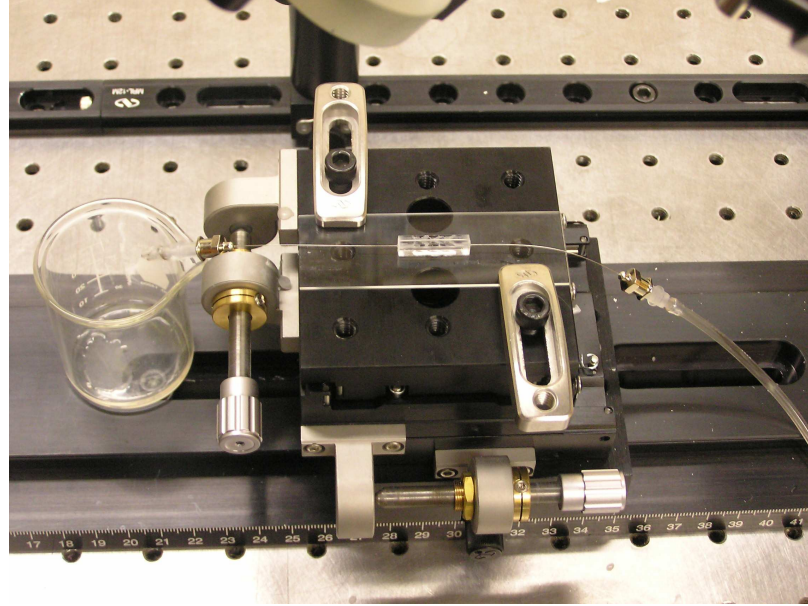


Fig. 7.10. Thick walled square microchannel used to study effects of RI change and channel wall deflection on fringe shift.

tracked in Figure 7.8 is observed. From this result, one can observe the distinct decrease in fringe thickness which occurs at frame 30 when the pump is initialized and an increase in fringe thickness to the original position when the pump is extinguished. This element of fringe morphology also represents a general trend which varies in magnitude between channel types and test sequences.

7.1.2 Thick Walled Microchannels

To isolate fringe morphology, the thickness of the channel walls was increased, leaving the inner dimensions virtually unchanged. Due to increased channel rigidity, the dependence of fringe shift on channel deflection could effectively be observed. This, in turn, resulted in an increased ability to study the effects of changes in fluid RI under cell pressurization and fluid flow conditions. Both round and square channel geometries were tested, a listing of which may be found in Table 7.1. Examples of the types of thick walled microchannels implemented in this study, as well as their mounting conditions, can be found in Figures 7.10 and 7.11. The channel shown in Figure 7.10 is of 0.25 mm square cross section in a glass cell of 4.00 by 4.00 mm outer dimensions. The round channel shown in Figure 7.11 has a diameter of 0.008 inches and has been bored through a quarter inch glass rod. In both cases, the channel walls are significantly thicker than in the case of the capillary tubes resulting in smaller deformations.

Using distilled water under flowing conditions, both the circular and square channel geometries were observed to produce fringe shifts. In the case of these channels, the shift sensitivity was found to be drastically lower than that reported in the previous section for round and square capillary tubes. Although no experimental data has

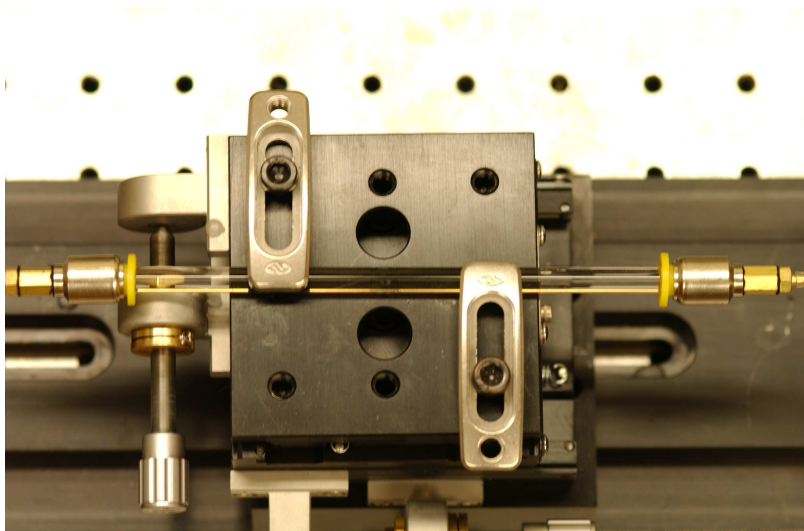


Fig. 7.11. Thick walled round microchannel used to isolate the effects of RI change and channel wall deflection on fringe shift.

been presented for the channels shown in Figures 7.10 and 7.11, from these observations, it was hypothesized that channel deflection played a large role in the magnitude of the fringe shifts. This conjecture will be proven correct by the thick walled channel results reported in the following sections. To simplify the interference signal, the channel geometry was then increased in one dimension such that the cross section was wider than the laser beam. This modification, in conjunction with the thicker cell walls, led to a more complete understanding of the interferometric signal and will be discussed in the remainder of this chapter.

7.2 Channel Cross-Section Greater than Beam Diameter

7.2.1 Thin Walled Rectangular Channels

A major criterion in defining a device as a backscattering interferometer is that the channel cross section must be smaller than the diameter of the laser beam. If this condition is not met, the apparatus forms a variation of the more commonly known Fabry-Perot interferometer described in Section 2.1. The major differences between MIBD and the Fabry-Perot interferometer are that in most cases, the walls of the channel are not parallel to one another (when using circular or drawn glass channels), in addition, the reflectivity of the glass is not high enough to cause the significant auxiliary reflections required to form a Fabry-Perot style interferometer. As a result, the use of a rectangular channel having parallel walls wider than the diameter of the impinging beam is neither entirely a backscattering interferometer nor entirely Fabry-Perot. It is understood that causing interference by reflection of light in this manner is not a new idea, and in fact, it is the known relationships from such a configuration, described in Section 5.5, which make this modification desirable in this study. Moreover, use of this technique for micro-scale pressure measurement

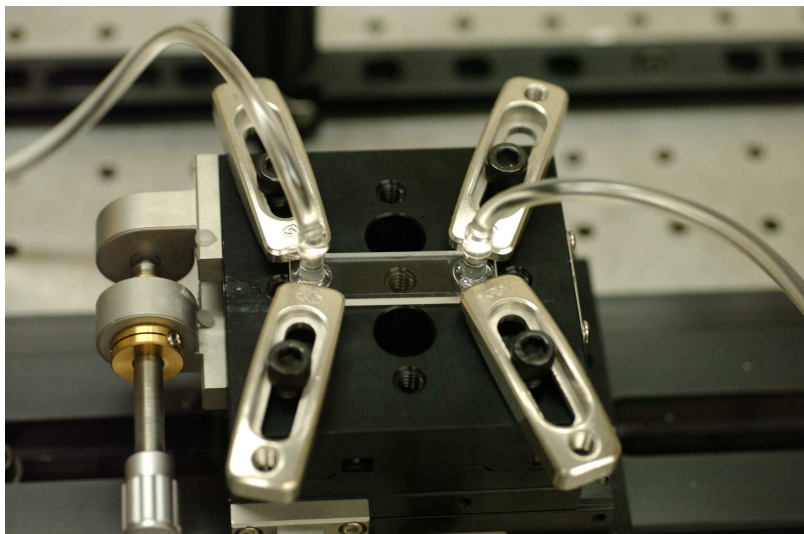


Fig. 7.12. Rectangular channel with relatively thin walls and channel width significantly larger than the laser beam diameter.

application has not yet been found to be demonstrated in any literature, making the solution a desirable scientific achievement.

To modify the channel to the described predictable geometry, the cross-section was made rectangular with dimensions of 9 mm by 0.05 mm. During initial testing, standard spectrometer cells were used, such as that shown in Figure 7.12, having viewing windows approximately 1 mm in thickness. The cell was secured using four metal clamps, as shown in the figure, which were tightened to the maximum amount without promoting fracture of the glass. Under this configuration, the cell was tested under both flowing and static conditions, allowing for fringe shift quantification based on both pressure and fluid velocity. Since the channel was now larger than the diameter of the laser beam, the backscattered arc was eliminated thus simplifying the interferometric signal.

The results of the fluid flow testing using distilled water in a 50 micron rectangular channel are shown in Figure 7.13. In addition, Table 7.3 has been provided as a key to show the theoretical pressure drop over the length of the channel as well as the pump flow rate setting for each of the tested fluid velocities. From Figure 7.12 one can see the results of two test sequences in which the fluid flow rate was set to various levels and the corresponding fringe shift was determined. The results are linear for the flow velocities below 25 mm/sec after which sensitivity begins to decrease. The significant spread in the data at flow velocities below 5 mm/sec are mainly a result of fringe tracking error (\pm two pixels for spotlight tracking used here) and the unpredictability of channel deflections, which will be significantly reduced through the efforts reported later in this thesis.

Although the thin walled rectangular channel displayed a common data trend between tests, just as in the case of the capillary tubes, the results were not reliable enough to allow for accurate quantification of fluid pressure. To study the phenomenon more closely, flow was eliminated from the system and static pressures were

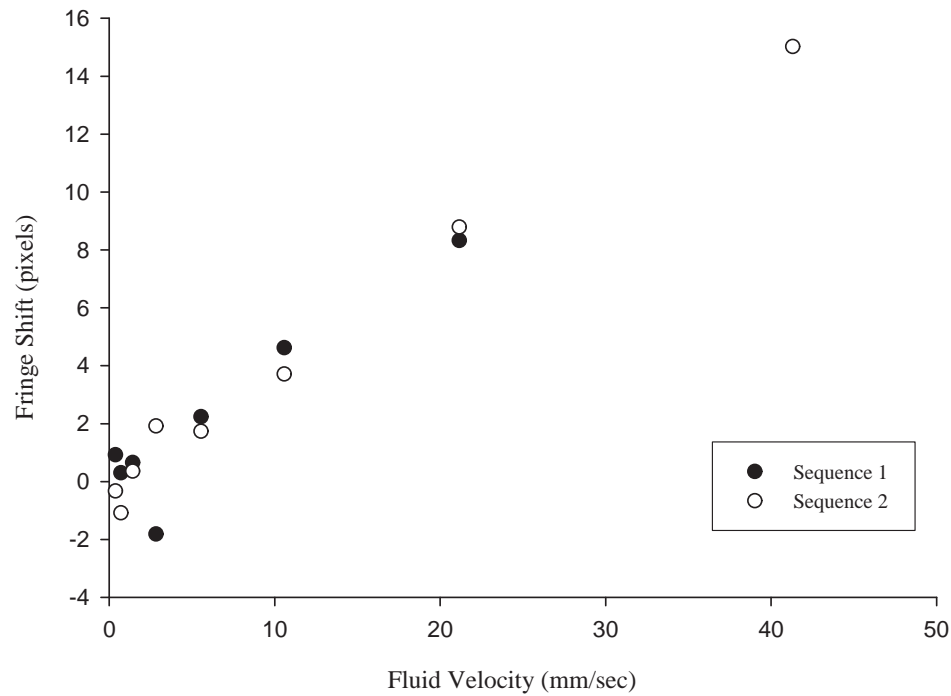


Fig. 7.13. Fringe shift at various fluid flow velocities for the thin walled rectangular channel shown in Figure 7.12.

Tab. 7.3. Fringe shift data as well as corresponding velocity and pressure drop values calculated using Equation 7.2. Negative fringe shifts represent experimental error in addition to instances where the pump was not properly primed for flow. Raw data indicated an error of plus or minus two pixels.

Flow Rate Setting	Test 1 Pixel Shift	Test 2 Pixel Shift	Theoretical Velocity (mm/sec)	Theoretical Pressure Drop (Pa)
13	N/A	15.0	41.3	49
15	8.3	8.8	21.2	25
17	4.6	3.7	10.6	13
19	2.2	1.7	5.5	6.3
21	-1.8	1.9	2.8	3.4
23	0.66	0.36	1.41	1.73
25	0.30	-1.08	0.71	0.881
27	0.92	-0.33	0.37	0.458

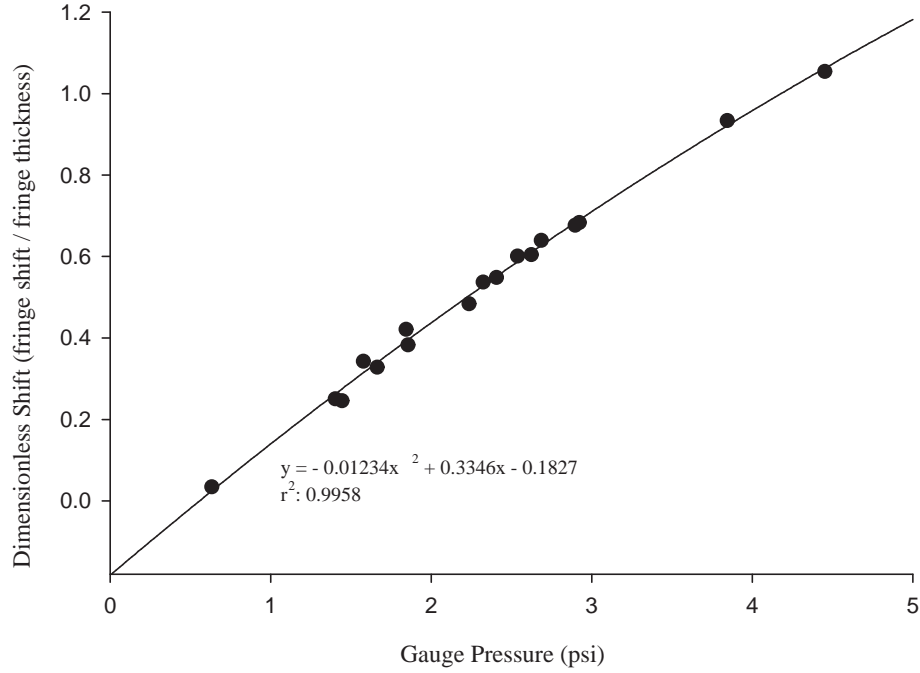


Fig. 7.14. Dimensionless shift at various static pressures for the thin walled rectangular channel shown in Figure 7.12. As channel deflects due to pressurization, the shift becomes non-linear.

measured using the modified apparatus shown in Figure 5.5. Air bubbles potentially trapped in the system, inlet tube flexibility, and pump inconsistencies were all found to be unquantifiable errors which could potentially have large effects on flow data, since the calculated velocity for a given pump setting did not necessarily correlate to average velocity within the cell. Using static tests, the data spread was significantly reduced as shown in Figure 7.14. Increasing to pressures beyond those experienced by the cell during flow testing, the results were found to deviate from linearity as was eluded to by the results in Figure 7.13.

The dimensionless fringe shift, plotted as a function of gauge pressure in Figure 7.14, was determined by dividing the fringe shift, measured in pixels, by the fringe thickness, also measured in pixels. In doing this, the number of fringes to pass a given point on the observation screen are effectively tracked, thus giving a value of Δm for the physical relationship to changes in beam path length difference. The dimensionless shift was found to be closely estimated by a second order polynomial with no significant fringe shifts occurring below a pressure of 0.5 psi. Below this value, the apparatus cannot detect shift caused by pressurization due to the physical limitations in the CCD array. Essentially, a pressure below this minimum value causes a shift of less than one pixel on the CCD for the fringe magnification used here. In the event that magnification is increased, the detection limit is also increased. However, it is important that the thickness of the fringes can also be measured to

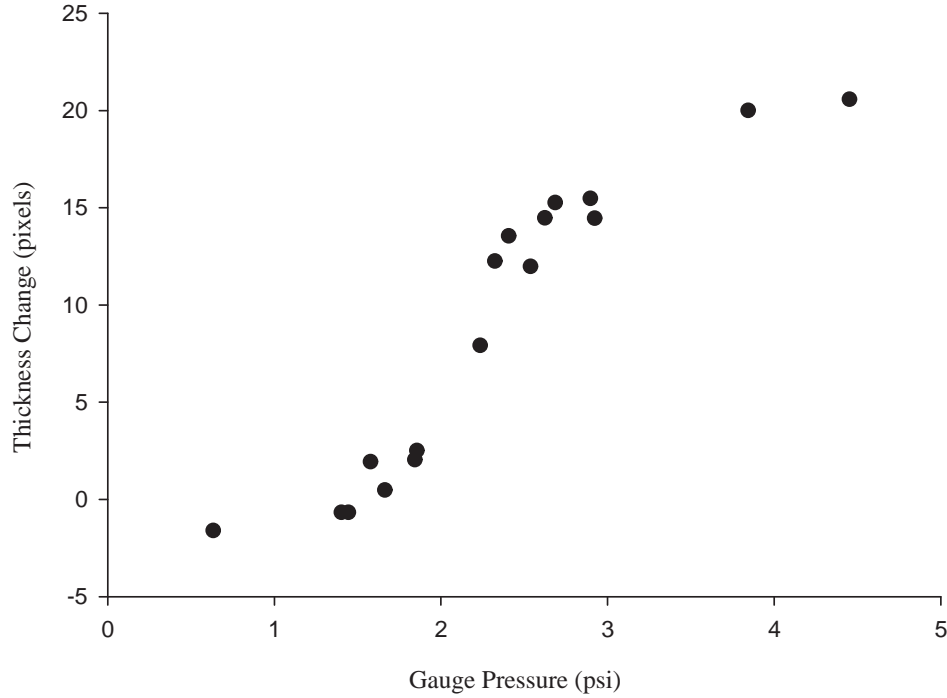


Fig. 7.15. Thickness change of a bright fringe at various static pressures for the thin walled rectangular channel shown in Figure 7.12.

non-dimensionalize the results. In practice this places a limitation on the maximum allowable magnification, a value directly dependent upon the physical dimensions of the CCD array.

Finally, the thickness change in the fringes was calculated for those tests in which a positive fringe shift was observed. For low pressures, experimental errors such as laser intensity fluctuations resulted in slightly negative thickness changes since cell deformation was very low. These results, depicted in Figure 7.15, show negative thickness values at low pressures and an increase in fringe thickness as cell pressure was increased. This thickness change is a product of primarily due to channel deformations, but also can be caused by large changes in RI as the impingement angle deviates from the surface normal. An increase in wall separation results in thicker fringes due to a larger horizontal separation in the reflecting beams. In the event that the beam is not directly in the center of the cell (at the apex of the deflection zone), there is also a change in fringe geometry, an effect of a tilting in the upper surface of the channel.

7.2.2 Thick Walled Rectangular Channels

To further reduce channel deformations, a custom variation of NSG Precision Cells model Type 48 with 5 mm thick viewing windows was used. The interior cross-sectional dimensions of this cell were identical to the inner dimensions of the thin

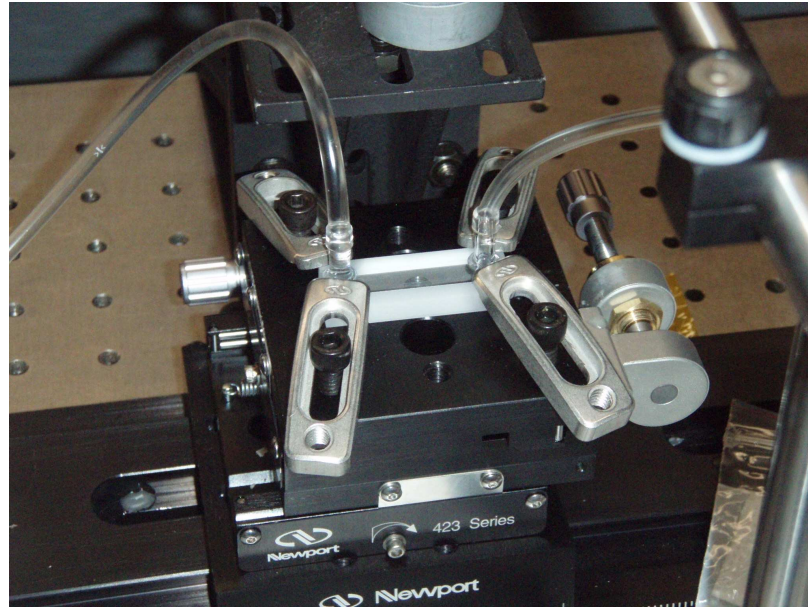


Fig. 7.16. Rectangular channel with thick walls and channel width significantly larger than the laser beam diameter.

walled cell shown in Figure 7.16 being 9.00 mm x 0.05 mm. Figure 7.16 shows this cell as well as the mounting and inlet/outlet conditions used in testing. This channel was first tested under fluid flow conditions with distilled water as the working fluid, the results of which can be found in Figure 7.17. As with previous results, there is significant spread in the data. This data spread is caused by the fluid flow; more specifically, pump variations under load and the formation of small bubbles in the system which present difficulty in accurately predicting fluid flow characteristics such as entrance losses.

Since flow variations caused results with poor repeatability, the flow was once again eliminated from the system and static cell pressurization was correlated to fringe shifts. Using the channel pictured in Figure 7.16, the variation of pressure under static conditions (as opposed to flowing conditions) resulted in the plot shown in Figure 7.18. Through the elimination of fluid flow, test results collapse to a single line similar to the case of the thin walled version of this channel. Using water as the working fluid at pressures less than 10 psig, the channel walls are now sufficiently thick that deflection remains linear throughout the pressure range. These findings, represented in Figure 7.19, demonstrate a vast increase in the predictability of the system when fringe morphology is properly controlled. In addition, the corresponding fringe thickness values have been calculated and are provided in Figure 7.19. Once again, as pressure was increased within the cell, fringe thickness increased, however, the magnitude of the thickness increase is much lower (less than half) than the identical channel with thin walls.

Upon comparison of these results to Figures 7.14 and 7.15, which were captured under nearly identical conditions, one can observe that the fringe shift no longer levels out within the given pressure range because fringe thickness changes are reduced due

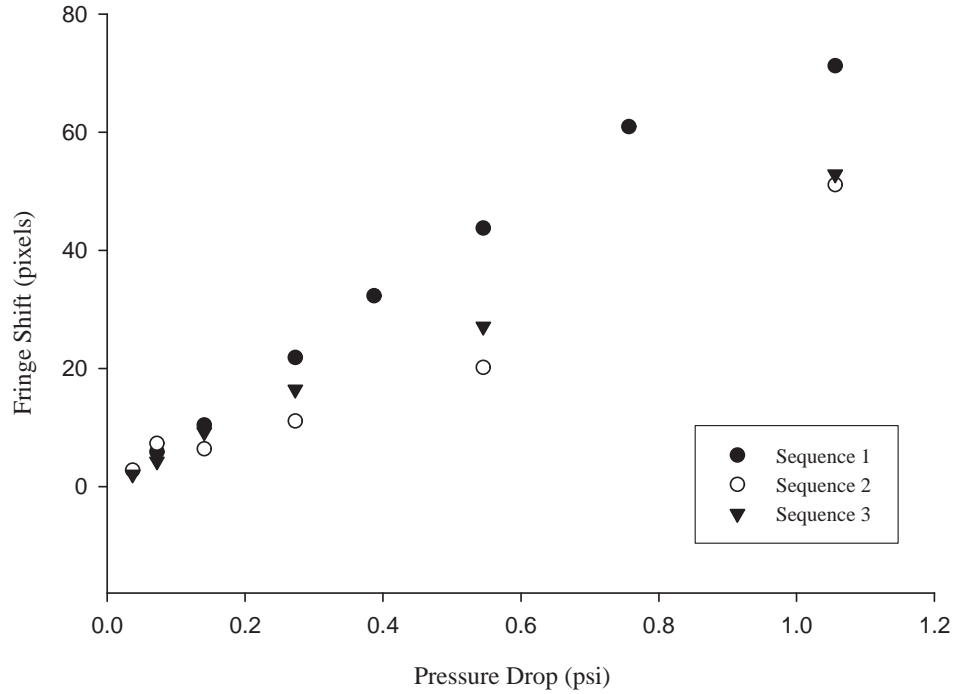


Fig. 7.17. Fringe shifts due to fluid flow in a 50 micron channel with thick side walls for three separate test sequences.

to a decrease in channel deformation. It is anticipated that testing of the thick walled cell at higher pressures would result in the same data trend as those observed for the identical thin walled cell. However, such tests could not be performed here due to the pressure limitations of the channel.

It is also important to note the significant reduction in the data spread as cell deformations were controlled. From Figure 7.19 one can observe only two data points were recorded to display a fringe thickness change over four pixels. The deviation of these points from the best fit line is clearly observed upon direct comparison of Figures 7.18 and 7.19, indicating fringe thickness change is an excellent indicator of experimental error. The major sources of error present in these experiments and their effects on the data will be described in detail in Section 9.3.

To further explore fringe shift as a result of cell pressurization, the previous experiment was performed using air as the fluid within the channel. It is known that the RI of air is significantly more sensitive to pressure changes than water due to the vast differences in their compressibilities. In performing such an experiment, the portion of the signal due to RI change and that resulting from channel deflection could effectively be determined. The results of static pressure testing on the same channel filled with air are provided in Figures 7.20 through 7.22, demonstrating very similar data trends to the previous results.

The raw shift data, provided in Figure 7.20, was produced through fringe tracking in Matlab and shows the shift of the left and right sides of the interrogated fringe

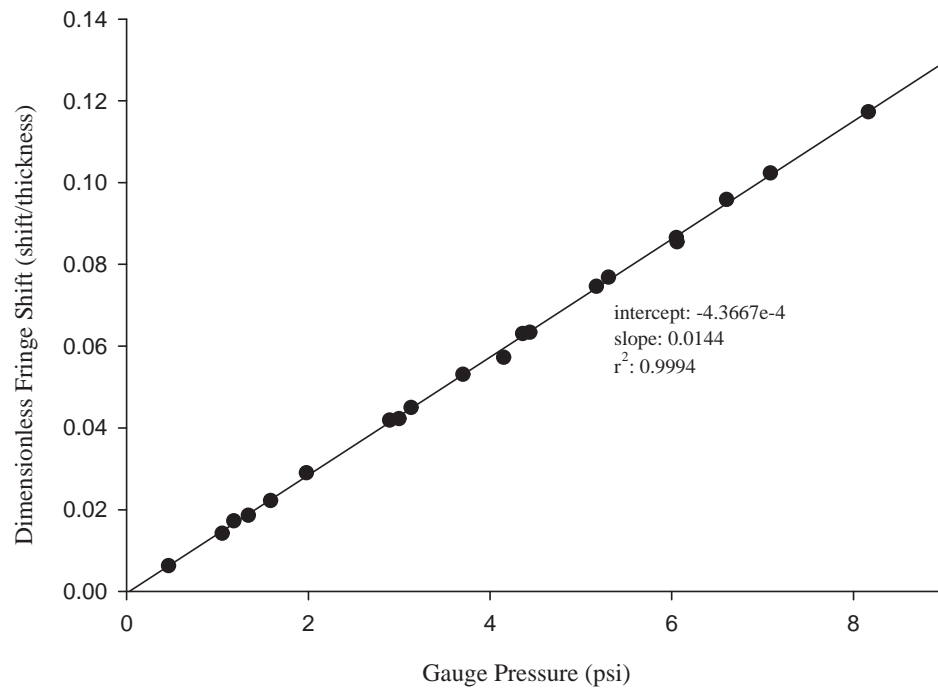


Fig. 7.18. Fringe shift due to static channel pressurization using distilled water and the test cell shown in Figure 7.16.

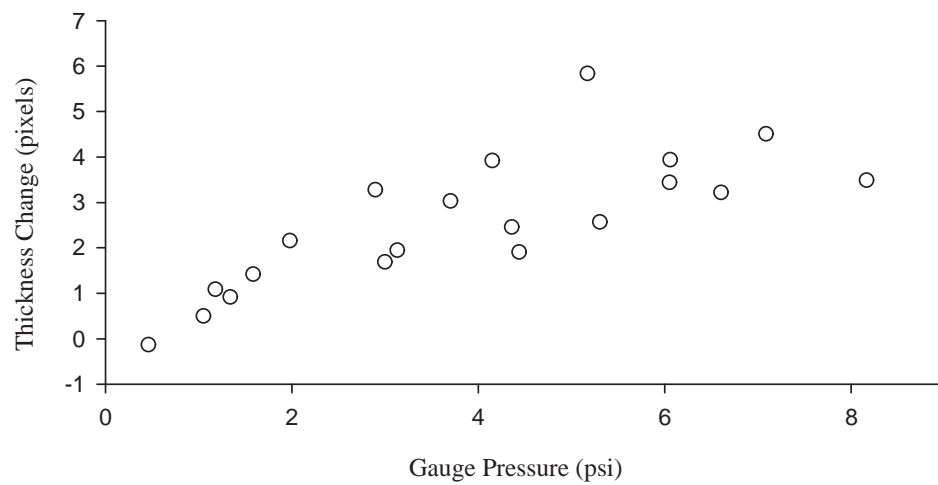


Fig. 7.19. Fringe thickness changes due to static channel pressurization using distilled water and the test cell shown in Figure 7.18.

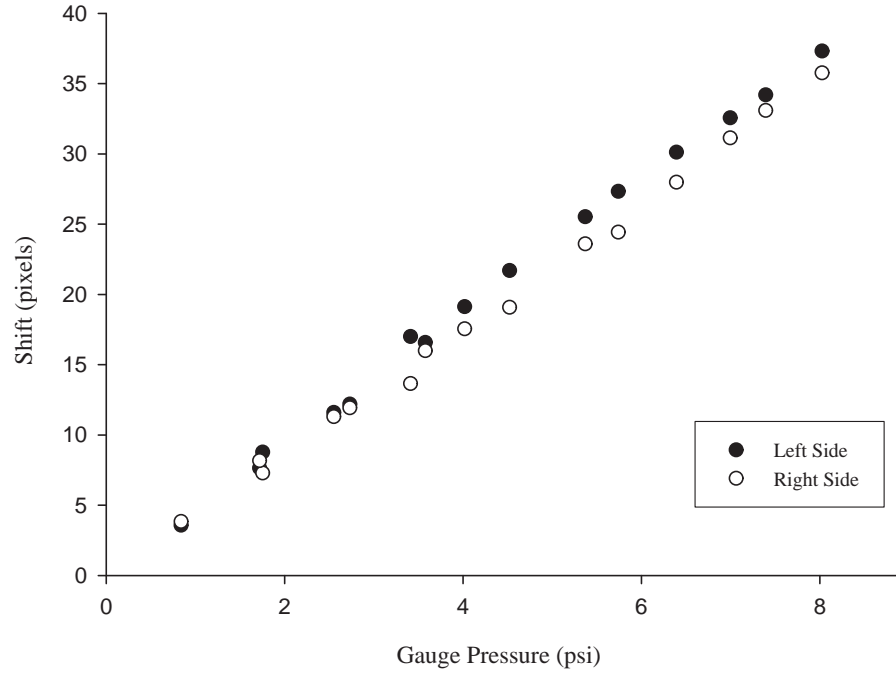


Fig. 7.20. Fringe shift of left and right sides of interrogated fringe due to static channel pressurization using air and the test cell shown in Figure 7.16.

through a pressure range of approximately 8 psig. Here the thickness change is apparent since the separation in the shift values from each side of the fringe is equal to the increase in fringe thickness produced by channel deformation. Upon averaging these two values for each pressure and non-dimensionalizing the data based on fringe thickness, the data can be collapsed further resulting in Figure 7.21. Here, the advantage of a CCD array over a photodetector becomes apparent since both sides of the fringe can be tracked, allowing for non-dimensionalization of the results. Without non-dimensionalized results, the fringes cannot universally be related to physical quantities and instead one must calibrate the device in-situ before use.

Finally, Figure 7.22 provides the fringe thickness changes at various cell pressures. These values are comparable to those found in Figure 7.19 for the water filled channel and are consistently much less than in the case of the thin walled channel with identical inner geometry. At first glance the results for air and water from this channel appear almost identical, leading the reader to believe the signal is not a function of fluid RI changes.

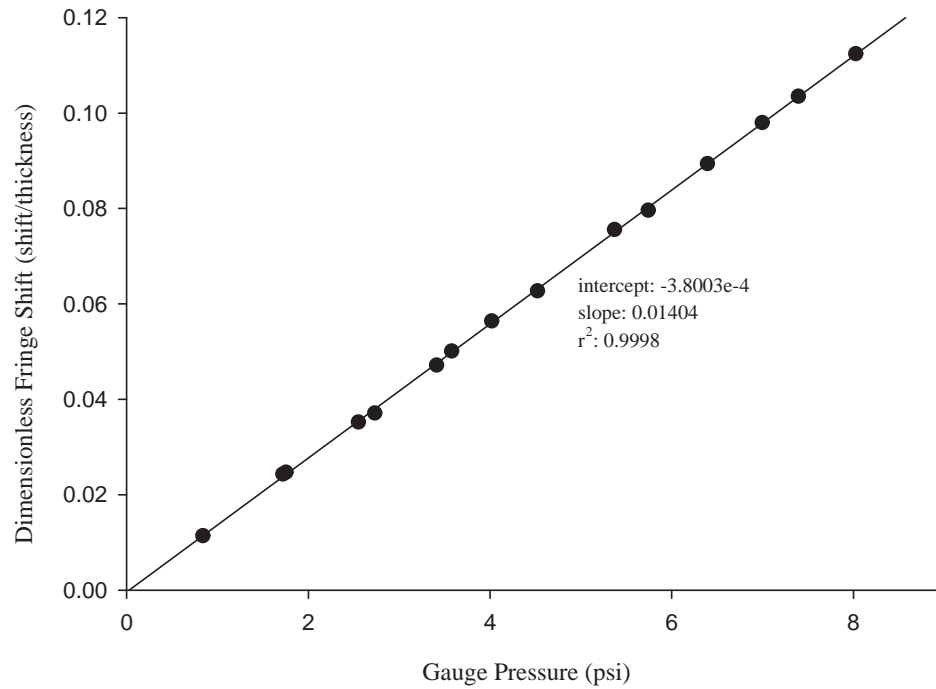


Fig. 7.21. Dimensionless fringe shift due to static channel pressurization using air and the test cell shown in Figure 7.16.

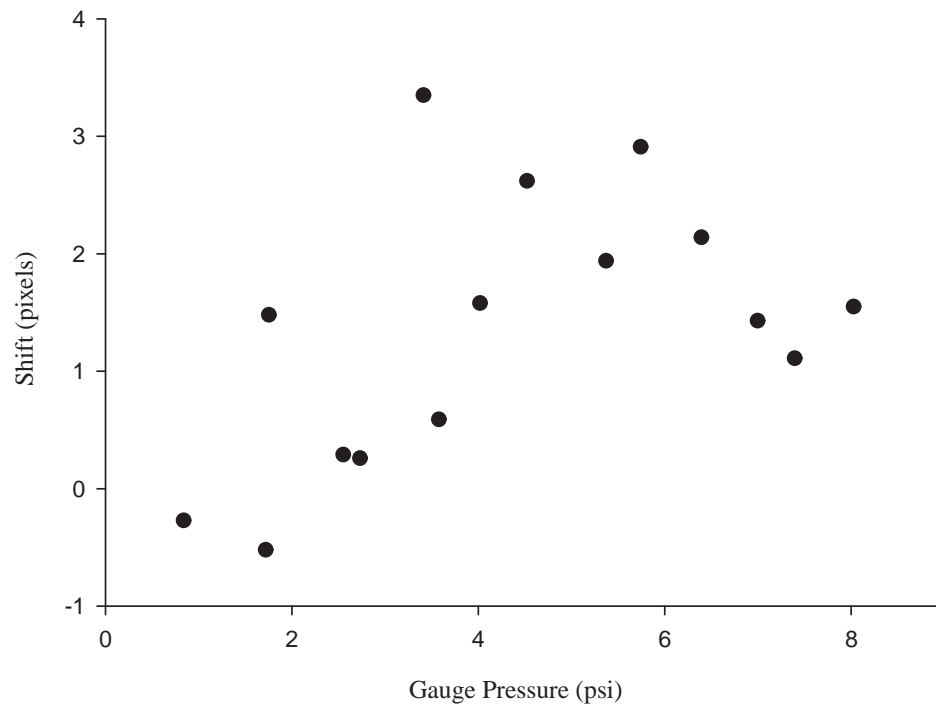


Fig. 7.22. Fringe thickness changes due to static channel pressurization using air in the test cell shown in Figure 7.16.

8. VERIFICATION OF RESULTS

8.1 *Laser Stability Testing*

It is known that a HeNe laser typically displays intensity fluctuations between 0.1% and 1% of its maximum intensity as observed by Bornhop and Wang [1]. To explore how these intensity fluctuations were affecting the experimental results, a Newport Model 818-BB-21 photodetector was placed in the path of the laser beam. Using an Agilent Model 54621A Oscilloscope as shown in Figure 8.1, the intensity fluctuations were observed over time via the voltage output of the photodetector.

It was found that the laser intensity variations were most prominent when the laser was first activated. This is expected since with most hardware, a startup time is required for the system response to stabilize as commonly observed with illumination sources and transducers. To study the effects of the start up time and intensity fluctuations on the output of the laser, the detector signal was observed at various times after startup via the oscilloscope and captured for later analysis. Signals were captured at times of approximately 2, 10, 16, 23, 70, and 120 minutes from startup and plotted to observe the change in fluctuation frequency and amplitude. The results of this test are summarized in Table 8.1, and the plots used to produce these results can be found in Appendix D.

A typical laser intensity fluctuation pattern from the red HeNe laser (model, SN) used in this experimentation can be seen in Figure 8.3. A green HeNe laser (Model 30968, SN 6049-4705-903) was also observed to have similar fluctuations although extensive testing was not performed on this device since fringe shift data captured with this laser was not of a quantitative nature.

It can be observed from Table 8.1 that, as time progressed, the laser continued to stabilize, demonstrating a decrease in fluctuation frequency and a relatively constant intensity fluctuation as a percentage of the full scale intensity. This shows that as the laser stabilizes, the intensity fluctuations produce much less impact on transient events, although these variations remain problematic for longer testing in-

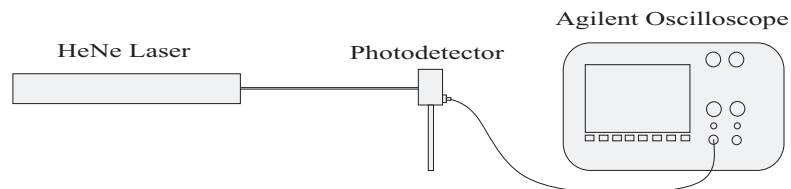


Fig. 8.1. Simple optical arrangement used in testing laser intensity fluctuations.

Tab. 8.1. Laser intensity fluctuation characteristics observed at various time intervals after startup.

Time (sec.)	Frequency (Hz)	Intensity Fluctuation (% of Full Scale Output)
2	0.22	5.8%
10	0.17	5.2%
16	0.11	5.0%
23	0.07	5.7%
70	0.007	6.8%
120	< 0.002	7.0%

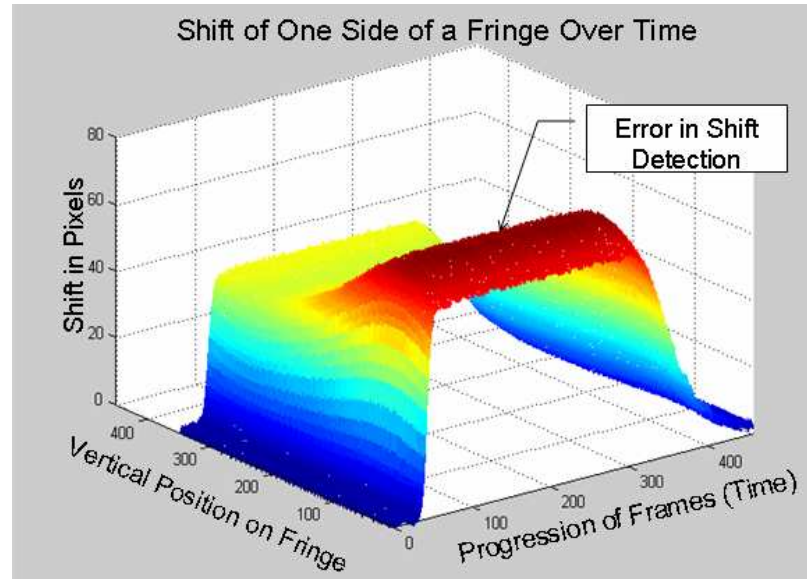


Fig. 8.2. Shift of one side of a fringe captured at 3 fps showing error in shift detection (manifested as variation in the z-direction) caused primarily by intensity fluctuations and mechanical vibrations.

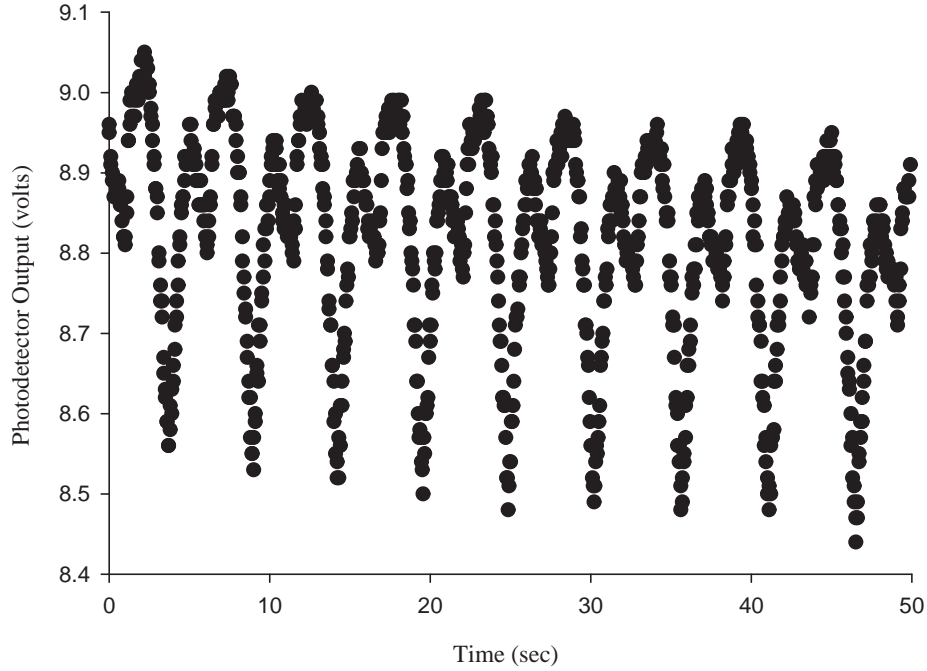


Fig. 8.3. Intensity fluctuations displayed by a 1.5 mW HeNe laser as captured by a photodetector.

tervals. From the plot shown in Figure 8.3, as well as those results at various times shown in Appendix D, one can see that these fluctuations present a high degree of unpredictability in the fringe shift results since data captured during an intensity rise would result in larger recorded shifts and data collected during an intensity decline would result in smaller recorded fringe shifts. This issue has been addressed with notable success by Bornhop [1] through the use of DCDB MIBD where fluctuations are captured by a second control detector and subtracted from a primary shift detecting signal thus compensating for the intensity fluctuations [1]. Although this may seem to be one of the most obvious solutions, it is not without problems which include synchronization of the signals as well as the production of an identical fringe pattern to act as the control (difficult when channel geometry is not constant).

The described intensity fluctuations are manifested as an error in the fringe shift value as shown in Figure 8.2. Here it is observed that as a fringe is tracked through a series of frames, the intensity variations cause a tracking error shown by the vertical fluctuations in the plot. This tracking error has been observed to be as great as ten pixels in some cases, depending upon the proximity of data collection to laser startup and the magnification of the fringes on the CCD array. It should be noted that the vertical fluctuations can also be attributed to mechanical vibrations in the system which have the potential to cause similar errors. On the whole, laser intensity fluctuations play an important role in shift quantification error although control of this phenomenon is possible. Future shift quantification efforts will most likely address

this issue more aggressively than the data displayed in this thesis, thus improving the capability and reliability of the technique.

In some cases, the intensity fluctuations could be observed on the monitor displaying the CCD output. This was found to be most prominent near laser startup and at high fringe magnification. To verify the intensity fluctuations, the laser was mounted in a mass spectrometer containing a slit diffraction wavemeter with analog light intensity measurement capability. Using this device, the same fluctuation pattern observed through the use of the photodetector was witnessed. No graphical results are provided for this test since no digital output was possible, however, the fluctuation frequency was observed to decay over time as in previous observations. Using this system, the signal was not observed to decay in magnitude, as observed in the plots from the photodetector. This signal bleed off is believed to be from stabilization of the photodetector since it also was found to level out over time, while the laser fluctuations remained roughly the same percentage of the full scale intensity of the laser.

8.2 Deflection Testing

8.2.1 Michelson Interferometer

To verify that pressure increase was causing channel deformation, two more experiments were performed. First, a mechanism was created to pinch off the exhaust tube and induce a large pressure increase inside the channel. Clamps were found to be inadequate since mechanical vibration caused in hand tightening the clamp produced unwanted shifted and caused difficulty in determining results. To remedy this problem, a tube pinch-off mechanism was created using a linear actuator which pressed a steel rod against the tube effectively creating a flow restriction. Figures E.1 and E.2 of Appendix E show the device in its entirety. Using the mechanism to restrict or stop flow allows one to control cell pressurization without changing the experimental setup to the static testing configuration, which required different inlet and outlet tube types. To create flow restrictions, the exhaust tube was pinched by activating a linear actuator which moved a steel rod against the flow tube. Since the linear actuator was for optical instruments, it was highly sensitive to position allowing for very precise control over the size of the flow restriction and the pressurization of the cell.

To observe the deformation in the top surface of the channel produced by cell pressurization, a Michelson interferometer was constructed next to the backscatter set-up to observe the deflection magnitude. As discussed in Section 2.1, a Michelson interferometer is commonly used to measure extremely small displacements (sub-micron sensitivity) through the use of two arms with a mirror at each end. A fully labeled view of the device used in this testing can be seen in Appendix E. For the arm of the interferometer used to observe the displacement in the 50 micron channel, a mirror was placed on top the thin walled rectangular cell where it was thought to deflect as shown in Figure 8.4. The beam incident upon this mirror was retro-reflected into the laser aperture to produce an interferometric signal on the observation screen (see Figure E.4). Upon the introduction of flow in the cell, the fringes were observed

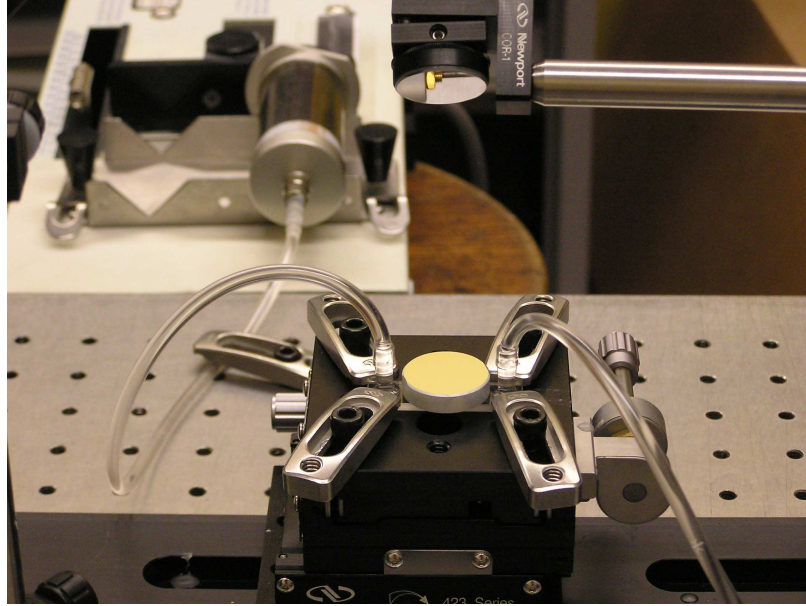


Fig. 8.4. Mirror placed on top flow channel to make up second leg of a Michelson interferometer and test for plate deflection in the top surface of the channel.

to shift slightly and change in thickness due to both translation and rotation of the mirror on the cell. In addition, when the tube was pinched a fringe shift of up to one fringe occurred. This indicated a tilting of the mirror and proved that deflection was in fact taking place as a consequence of cell pressurization. Upon identical testing of the thick walled rectangular cell, no deflection was observed. Any wall deflection was found to be too small to detect without fringe image processing. By comparison to the results in the previous chapter, it is determined that lesser deformations were, in fact, taking place in this channel as depicted in the fringe thickness results. These observations confirm that channel deformation was present resulting in fringe position and thickness changes since fringe thickness change is directly related to channel geometry changes.

8.2.2 Finite Element Analysis of the Cell

Using the derivation of the beam path to fringe shift relationship provided in Section 5.5, the theoretical fringe shift based on a change in the channel thickness could be calculated. In both the case of the air and water static testing results, the theoretical shift was found to be lower than the experimentally measured fringe shifts. This confirmed that a portion of the signal producing these highly linear results (shown in Figures 7.18 and 7.21) was from another source, namely, fluid RI changes.

To confirm this hypothesis, a relationship for the change in channel thickness as a function of pressure was required. Since the channel deformation was not constant over the surface of the channel, the Michelson interferometer was not ideal for measurement of these deformations. Sputtering of a reflective surface on the cell was a possibility, however, the non-uniformity of the channel deformation would cause

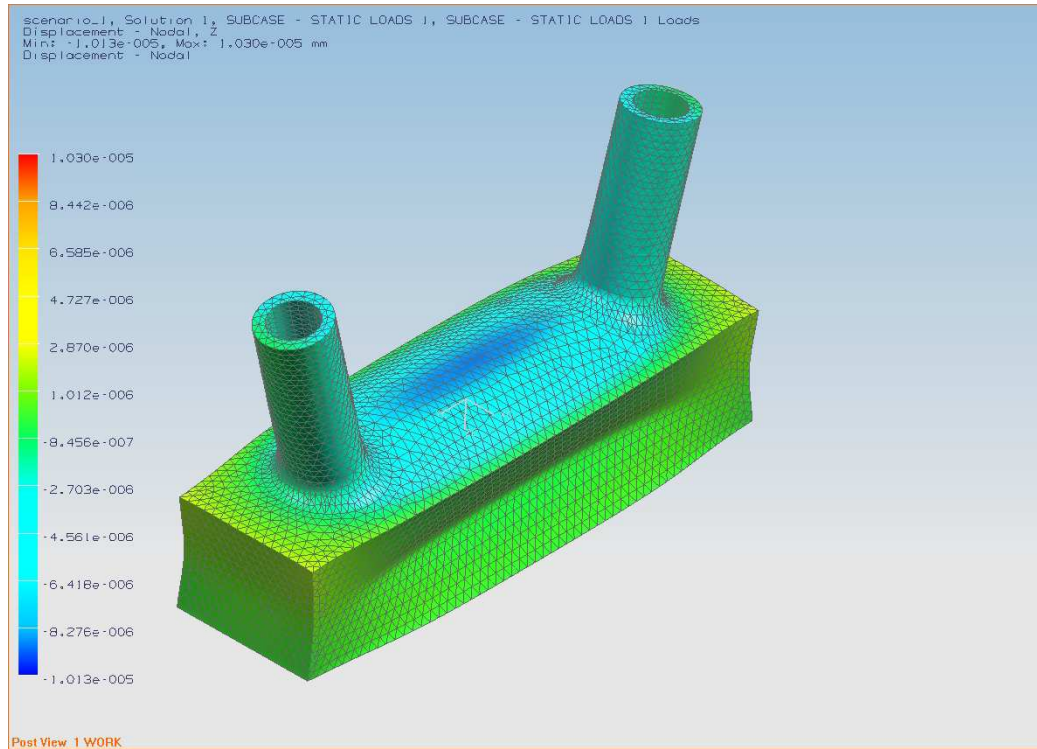


Fig. 8.5. FEA analysis of thick walled rectangular channel under a static pressure of 5 psig. Deflection of the impingement area is shown in blue and is approximately 18 nm when both sides of the cell are considered.

asymmetric fringe formation, making accurate quantification difficult. To resolve this challenge in a less time consuming manner (and avoid coating the cell which would negate its backscattering capability), a finite element model was constructed to predict the channel deformation at various pressures.

The cell was modeled in Unigraphics NX3 and a uniform pressure distribution was applied to the internal surfaces. The resulting cell deformation, shown in Figures 8.5 and 8.6, depicts maximum deflections in the center of the channel at the impingement point. These results show deflection of the channel only in the z-direction (vertical) under a static pressure of 5 psi. When compared to deflection of the cell in all directions, these results are identical, however, this simplified display was chosen since deflection in this direction is characteristic of channel separation, which directly affects the fringe shift results.

Boundary conditions used for this model were those of a part in free space. Since the clamping force used to mount the cell was very low to prevent fracture of the glass, these clamps did not exhibit a force large enough to require modeling. In addition, the deflections calculated were on the order of tens of nanometers, a magnitude considered to be within the free movement of the clamps (vertical tolerance in the threads). Since only one of the bottom edges of the channel was fixed, the model was expected to slightly overpredict the experimental deformation results. Upon convergence of the mesh this was found to be the case since a smaller mesh size gives slightly larger

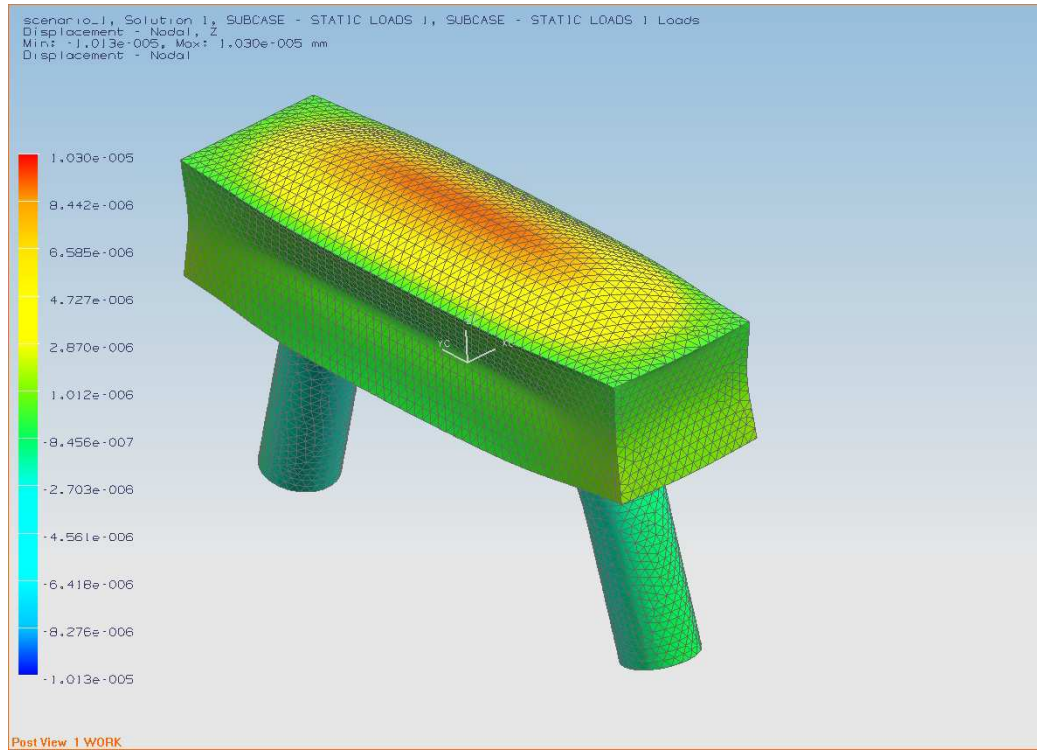


Fig. 8.6. Rotated view of Figure 8.5 showing deflection of bottom surface of cell in the z-direction.

theoretical deflections, but is much more computationally expensive. As a result, the FEA predictions are found to be sufficient to accurately estimate the deformation of the channel.

Using this FEA model, the relationship between channel wall separation and cell pressure is displayed in Figure 8.7. Using a mesh size of 0.8 mm, the model was found to solve in just three minutes and provide a linear relationship such as that desired to fit the experimental data between 0 and 10 psi. The mesh size was found to be sufficiently small such that the results changed by less than 1% when mesh size was reduced to half that of the previous value. The convergence of the mesh to a single value is depicted by Figure 8.8 where the values approach a single y-value in a fairly linear fashion. Ideally the slope of this line would decrease as the mesh size was decreased, however, the results do not appear to diverge from the solution and therefore represent a good estimation of the true channel deflection.

8.3 Verification with Known Data

8.3.1 Known Relationships for Air

Since the FEA model produced channel deformation estimations of lesser magnitude than those predicted from the experimental data, it was hypothesized that RI changes in the fluid comprised the remainder of the signal. In the cases of both air and water,

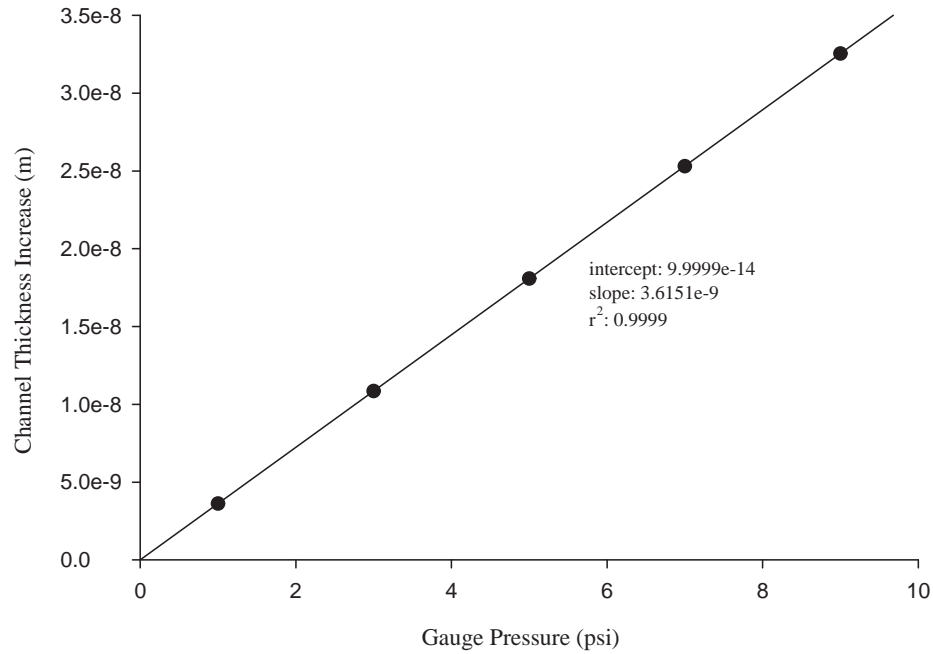


Fig. 8.7. Estimation of cell deflection using finite element model with a mesh size of 0.8 mm.

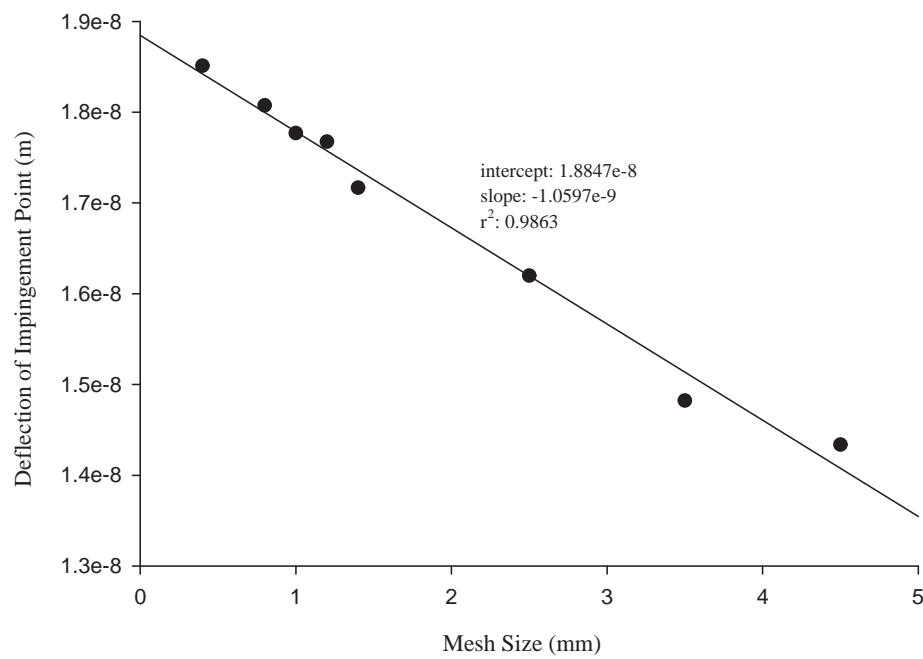


Fig. 8.8. Behavior of deflection estimation as mesh size is decreased at a static pressure of 5 psig. The mesh appears to converge at a value near 19 nm for this pressure value, a slight overestimation of the experimental results as expected.

data is available for the relationship between pressure and RI. For air, the relationship has accurately been described by Birch and Edlén [25, 26] to be

$$n(T, p) = 1 + (n_s - 1) \left[\frac{p(1 + p(60.1 - 0.972T)10^{-10})}{96095.43(1 + 0.003661T)} \right] \quad (8.1)$$

where the RI, n , is dependent upon temperature, T , pressure, p and

$$n_s = 1 + \left(\frac{0.0472326}{173.3 - \sigma^2} \right) \quad (8.2)$$

The wavenumber, σ , is defined as

$$\sigma = \frac{1}{\lambda_{vac}} \quad (8.3)$$

The expression given by Equation 8.1 is linear for the temperature range of interest. Therefore, assuming the temperature of the fluid remains constant (a good assumption since testing times were usually only a few seconds), the shift resulting from the calculated change in RI can be used to check the pressure measurement result.

8.3.2 Known Relationships for Water

Although empirical relationships and data are extremely limited, the relationship between RI and pressure was effectively observed by L. Zehnder in 1888 as reported by Dorsey [5]. In defining a constant Δ such that

$$\Delta = \frac{n_2 - n_1}{p_2 - p_1} \quad (8.4)$$

where n_1 and n_2 are the RI values at pressures p_1 and p_2 , respectively.

This relationship was found to be closely approximated by the equation [5]

$$\Delta = (16.84 - 0.129T + 0.0022T^2)10^{-6} \quad (8.5)$$

where T is the temperature in °C.

Upon equating 8.4 with 8.5 and rearranging we find

$$\Delta n = [(16.84 - 0.129T + 0.0022T^2)10^{-6}] (\Delta p) \quad (8.6)$$

Using Equations 8.1 and 8.6, the change in refractive index of air and water can be theoretically determined at various pressures. Using Equation 5.10, the theoretical fringe shift based on a change in RI can be determined, and upon subtracting these values from the experimental results, the remaining shift should be equal to the predicted cell deflection. Figure 8.9 shows a comparison between the channel deflections predicted by the FEA model and the deflections calculated from the experimental results minus the contribution for the RI change due to pressure variation. The theoretical and experimental results are found to match within 5% in the pressure range between 0 and 10 psig. From this result, one can see that pressure measurement

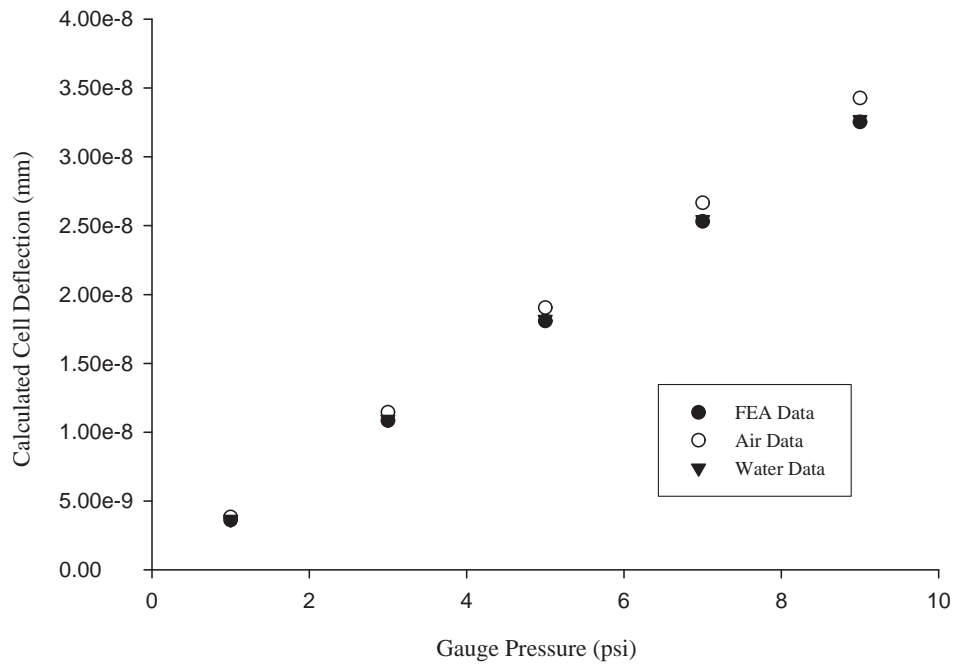


Fig. 8.9. Comparison of finite element model results with calculated deflections based on experimental data for air and water.

in microchannels is possible using the adapted backscattering setup. The signal is comprised of two main components, fluid RI change and channel deformation, which can be isolated or used in combination for pressure measurement. The magnitude of each of these components of the signal will be described in the following chapter.

8.4 Description of Matlab Codes Used in Data Processing

Using Matlab, several codes were written to calculate channel deflection, fluid RI, dimensionless fringe shift, and detection limits based on various theoretical and experimental conditions. The fully commented versions of these codes can be found in Appendices I and J. In these codes, the known theoretical relationships for the change in RI of air and water due to a change in pressure were utilized to verify the experimental results, calculate the detection limits of the technique under different operating conditions, and find the areas where the device could be most significantly improved to enhance measurement sensitivity. Due to the relatively low computational load of these calculations, simple loops were used in most cases to iteratively compute unknown values to a high degree of accuracy. This avoided the need for multiple Matlab files in the form of external functions and simplifies code use for future users. Note that external functions were used in some instances to promote brief and efficient coding. The results of these codes and the use of the equations in Sections 8.3.1 and 8.3.2 provided the basis for the sensitivity results reported in Chapter 9.

9. DEVICE SENSITIVITY

9.1 *Detection Limits*

Using the Matlab codes described in Section 8.4, the detection limits of the technique for measuring changes in RI of water and air were found. These detection limits were calculated for an impingement angle of 13° on a fused quartz glass cell with a channel thickness of $50\text{ }\mu\text{m}$, width of 9 mm , and length of 34 mm . Considering the fringe thickness corresponding to one wavelength of light (one light and one dark fringe) is 400 pixels and the shift tracking capability is to the nearest pixel, then the minimum detectable Δm is 0.0025. This corresponds to a RI change of $1.541 \cdot 10^{-5}$ and $1.560 \cdot 10^{-5}$ in air and water, respectively. Using the experimental conditions described above, the RI changes correspond to 0.842 psi and 14.800 psi for air and water, respectively. Utilizing the combination of channel deflection and fluid RI changes, the detection limits are reduced to 0.21 psi and 0.15 psi for air and water, respectively. Although the detection limits are not overly impressive in comparison to traditional methods, the technique is non-intrusive. In addition, there are several simple modifications that could be made to the device to drastically improve the detection and measurement capabilities of this technique.

9.2 *Effects of Experimental Parameters*

A complete understanding how each of the experimental parameters effecting the sensitivity of the technique allows for optimization of these factors and leads to maximum device sensitivity. To achieve such results, it is first important to define these factors effecting the experimental outputs. As described by Equations 8.1 and 8.6, it is clear that refractive index is primarily a function of temperature and pressure. It is also known that the composition and humidity of air play a role in RI. Likewise, the purity of water also is important in determining its absolute RI. Since these factors are not significantly altered during the measurement of the differential signal, they can be neglected in this analysis.

Using the known relationships for RI as a function of temperature and pressure, Equation 5.10 becomes

$$\Delta m = \left| \left(\frac{2n_{T,p}t \cos(b')}{\lambda} \right)_1 - \left(\frac{2n_{T,p}t \cos(b')}{\lambda} \right)_2 \right| \quad (9.1)$$

where $n_{T,p}$ is the RI of the fluid inside the channel as a function of temperature T and pressure p , t is the thickness of the channel, b' is the angle the light ray forms

with the surface normal, and λ is the wavelength of the light. The subscripts 1 and 2 refer to the initial and final states both before and after the fringe shift. The main factors effecting the sensitivity of the technique are found in Equation 9.1. These include the dimensionless fringe shift measurement δm , temperature, pressure, RI of the fluid used, channel impingement angle, and the wavelength of the light source. It is important to note that this relationship is only valid for interferometric techniques which follow the ray trace from Figure 5.8. In the case of this work, rectangular channels wider than the beam diameter and the central fringe of channels of cross-sectional dimensions lesser than the beam diameter have been accurately represented.

From Equation 9.1 and the deflection predictions of the finite element model, the dependence of the experimental setup on RI of the working fluid can be demonstrated. At first it would appear that there are two unknowns, channel thickness, t and RI, n , however, since the FEA model was verified to match the experimental findings it could be used confidently to determine the deformation of the channel thickness as a function of pressure. Therefore, using an iterative process where channel pressure is increased, the experimental Δm can be used to determine the RI values as a function of pressure. Plotting the relative contributions of channel deflection and RI over the experimental results, the portions of the signal coming from each source can be visualized. Figures 9.1 and 9.2 show the signal contributions for the testing of air and water, respectively. The RI change of air plays a much larger role in the formation of the signal than that for water. On the other hand, it can also be determined that the water filled channel results in an apparatus more sensitive to the detection of channel deflections (as shown in the sensitivities reported in Section 9.1). The physical reason for this difference is the light path through the channel. In the case of the air, the large change in RI at the glass-air interfaces causes a significant bending of the light, this results in an longer path length through the channel when compared to that of the light through the water. In addition, the RI change of air as a function of pressure is much greater, resulting in a larger portion of the signal from this source. In the case of these tests, the impingement angle was chosen such that the experimental results appear almost identical to one another prior to this analysis. However, upon deconvolution of the results one finds that this is simply a result of improbable circumstances and in reality the RI change of air contributes approximately 20% to the signal while the RI change of water contributes on about 3% of the experimentally measured signal. That is to say, even though the plots for dimensionless fringe shift as a function of pressure shown in Figures 7.18 and 7.21 appear to demonstrate nearly identical sensitivities, this is a result of a higher sensitivity to channel deformation for water relative to air and higher sensitivity of RI change for air relative to water.

To increase the sensitivity of the technique to changes in RI, the impingement angle should be maximized. Upon doing so the beam is forced to take the longest possible path through the fluid resulting in the maximum phase lag for a given channel thickness and thus a maximum fringe shift. Another simple alternative to increasing the sensitivity to RI is to increase the channel thickness. This effectively increases the phase lag of the light through the channel as well since the light is forced to travel a greater distance at a new velocity through the medium within the channel. In

comparison to the previously discussed parameters, temperature, barometric pressure, and wavelength of the light have relatively small effects on the results. Since the device is currently used to measure pressure and RI changes, these parameters do not significantly alter the experimental findings since the RI is found to be a linear function of these variables.

A final factor that is of paramount importance in the sensitivity of the device is the CCD sensor or photodetector used in data acquisition. In the case of the CCD sensor used in this experimentation, the fringes were typically set to approximately 400 pixels in width due to the physical limitations of the camera. This allowed for a shift detection of one part in 400 or a dimensionless fringe shift of 0.0025 (shift/thickness = $1/400$). On the other hand, a typical photodetector is capable of shift measurements as low as one part in 10^{-6} [7]. Using Equation 9.1 under the same conditions used to determine the sensitivities in Section 9.1 one finds the limits are dramatically reduced to pressure measurements of $3.63 \cdot 10^{-4}$ psi and $6.07 \cdot 10^{-3}$ psi for air and water, respectively, under ideal conditions. In reality, measurement errors such as mechanical vibrations and laser intensity fluctuations would reduce these measurement capabilities significantly, although the net result would still be a more sensitive device. In practice, it is difficult to use the photodetector for dimensionless fringe shift measurements since it does not readily allow for fringe thickness measurements. Once fringe morphology for a channel type is understood through the use of a CCD, the photodetector could be a logical addition to increase the sensitivity of the device.

Overall, to achieve optimal sensitivity, a channel of the maximum possible thickness should be used in conjunction with a maximum impingement angle. Control over temperature, pressure, and wavelength should be practiced during testing intervals and a detector of maximum spatial resolution should be utilized to quantify fringe shifts. Under these experimental conditions, the technique will display the greatest sensitivity to changes in fluid RI. As this sensitivity is increased, the effects of experimental error play a larger and larger role on the measurement limits.

9.3 Sources of Experimental Error

Sources of measurement error remain relatively constant between testing techniques and channel types. Those sources of error presenting the most immediate need for solutions are laser intensity fluctuations, isolation of air currents in the room (cause of RI changes in air between channel and detector), and inconsistency in channel deformations at different impingement positions. Other sources of error included the measurement of room temperature and pressure, fluid flow rate, channel pressure, fringe shift, inconsistencies in impingement angle (poor ability to measure this parameter), and finally mechanical vibrations. Through the isolation of these parameters, the error was found to be immensely reduced as shown by a comparison between the results shown in Figures 7.6 and 7.21. The results in Figure 7.21 demonstrate the improvements in technique reliability which are reflected in the small relative error shown in the measurements (less than 1% for those shown). Overall, precise quantification of these parameters is dependent upon the experimental parameters chosen by

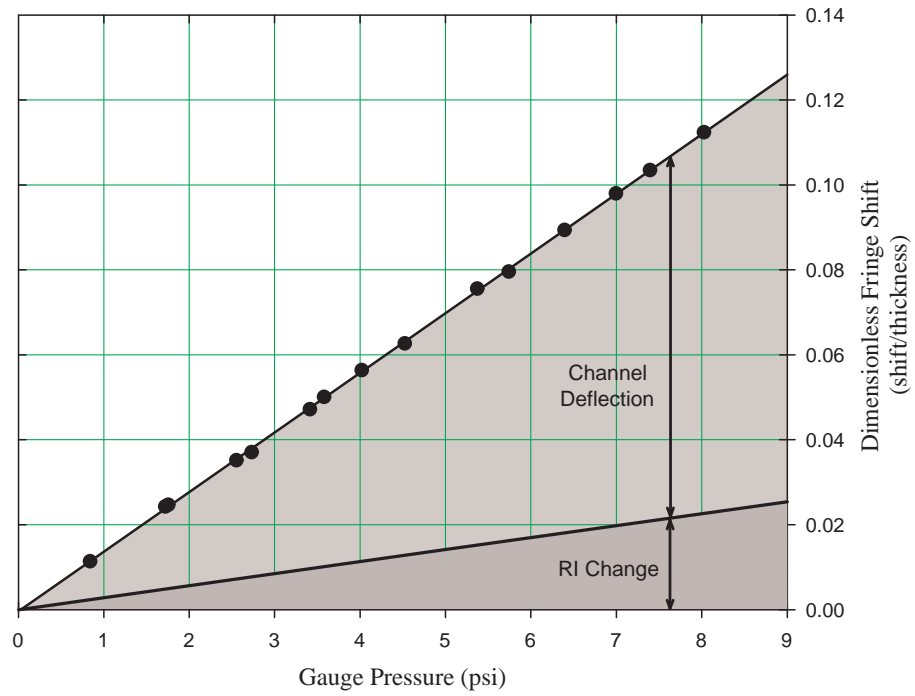


Fig. 9.1. Plot of the experimental results for cell pressurization with air showing components of the signal from channel deflection and fluid RI change.

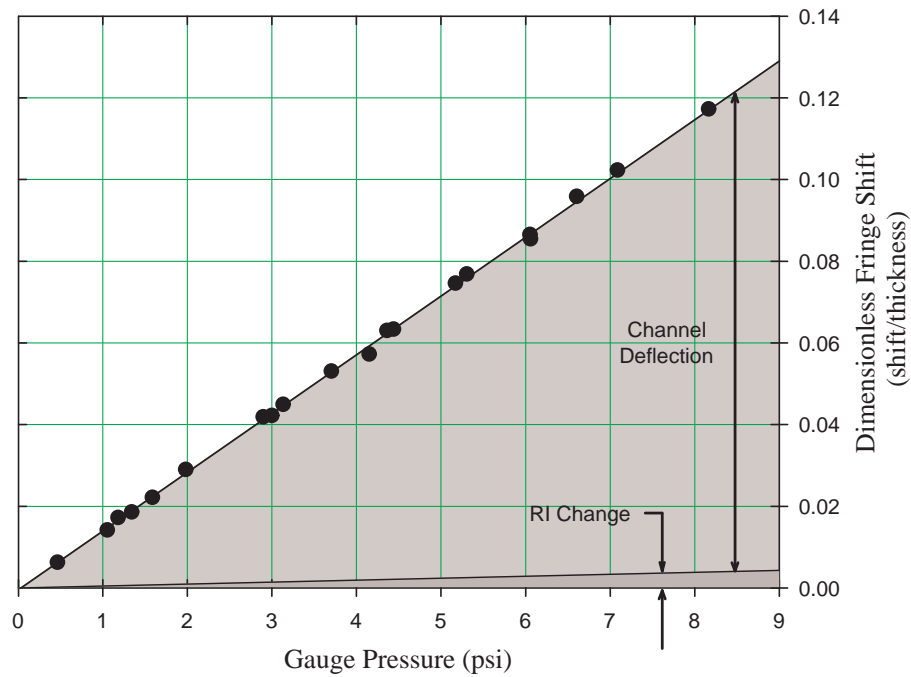


Fig. 9.2. Plot of the experimental results for cell pressurization with water showing components of the signal from channel deflection and fluid RI change.

the user. For example, although the parameters for the static testing proves to result in only 1% error, the use of a different camera sensor or the acquisition of data in the presence of pump vibrations could increase this value and would require case-specific quantification.

10. CONCLUSIONS

Backscattering interferometry has successfully been proven to be adaptable for pressure measurement in microchannels. Upon careful impingement of a channel, a laser beam can be made to interfere with itself as the light reflects from the inner and outer walls of the channel. This observed interferometric pattern changes with variations in channel pressurization, as a result, the quantification of these changes can be correlated to pressure and utilized as a measurement mechanism. The fringe movement and shape changes, also referred to as morphology, are consequences of fluid RI changes as well as channel geometry deformations. It has been observed that asymmetric fringe morphology signifies channel deflections while symmetric morphology can be a result of both RI changes and deformations.

The original motivation for this work was to measure pressure changes in flowing systems, therefore, the technique was first implemented on capillary tubes with flowing distilled water. These experiments proved the feasibility of this initiative demonstrating common data trends and the ability to detect flow within a channel, but the technique lacked repeatability and the capacity to accurately quantify pressure and flow rate values. It was hypothesized that the inability to duplicate results was caused by deformations in the walls of the channel. Upon increasing the wall thickness, the signal was significantly dampened, however, the remaining morphology was found to be symmetric and highly repeatable. These results were repeated using channels with cross sections wider than the laser beam proving that the channel did not have to be completely encapsulated by the beam to produce a highly sensitive signal.

The interferometric pattern was captured using a CCD array and morphology was quantified using image processing in Matlab. When used in conjunction with interferometric theory, this procedure resulted in an ability to quantify RI changes of the working fluid and variations in channel geometry. Using either known relationships for RI as a function of pressure, or a finite element estimation of the channel deformation, the causes of fringe morphology can be separated and quantified. To verify the results, both air and water were tested in a channel of known geometry. Using the known relationships for the RI changes due to pressure in conjunction with a finite element model, the experimental results were verified and found to match the theoretical calculations within 5%.

With the results verified, the channel deformation can be subtracted from the signal leaving only the RI change. This gives information on fluid compressibility and can be used to study the effects of pressure on fluids with unknown properties within the cell. Furthermore, if the RI change is known, channel deformations can be quantified below ten angstrom providing a highly sensitive deflection device. Detec-

tion and measurement limits are functions of channel size, geometry, and material as well as photodetector and fluid type. Using this method, non-intrusive pressure and RI measurements are possible in micro-scale channels providing a capability not previously available which could undoubtedly be found useful for numerous applications in the scientific community in the near future.

REFERENCES

- [1] Wang, Z., Bornhop, D. Dual-Capillary Backscatter Interferometry for High-Sensitivity Nanoliter-Volume Refractive Index Detection with Density Gradient Compensation. *Analytical Chemistry*, 77(24):7872-7877, 2005.
- [2] Begari, D., Markov, D., Bornhop, D. Breaking the 10^{-7} Barrier for RI Measurements in Nanoliter Volumes. *Analytical Chemistry*, 74(20):5438-5441, 2002.
- [3] Markov, D., Swinney, K., Bornhop, D. Chip Scale Universal Detection Based on Backscatter Interferometry. *Analytical Chemistry*, 72(13):2690-2695, 2000.
- [4] Eddins, S., Gonzalez, R., Woods, R. *Digital Image Processing using MATLAB*. Pearson Prentice Hall, 2004.
- [5] Dorsey, N.E. *Properties of Ordinary Water-Substance*. American Chemical Society Monograph Series. Reinhold Publishing Corporation, New York, 1940.
- [6] Dyson, J. *Interferometry as a Measurement Tool*. Hunt Barnard Printing Ltd., Aylesbury, Great Britain, 1970.
- [7] Newport Corporation. *Projects in Interferometry*. Newport Corporation, Irvine, Ca, Revision: B1, 1993.
- [8] Francon, M. *Optical Interferometry*. Academic Press, New York and London, 1966.
- [9] Wolf, E., Born, M. *Principles of Optics*. Oxford: Pergamon, 6th edition, 1983.
- [10] Sorensen, H. *Self Calibrating Interferometric Sensor*. PhD, Technical University of Denmark, 2006.
- [11] Bornhop, D., Swinney, K. Noninvasive Picoliter Volume Thermometry Based on Backscatter Interferometry. *Electrophoresis*, 22:2032-2036, 2001.
- [12] Wood, S., Bornhop, D., Markov, D., Dotson, S. Nonintrusive Fluid Flow Measurements in Microfluidic Channels with Backscatter Interferometry. *Electrophoresis*, 25:3805-3809, 2004.
- [13] Bornhop, D. Laser-Based Refractive Index Detector using Backscatter, 1994.
- [14] Swinney, K., Bornhop, D. Quantification and Evaluation of Joule Heating in On-Chip Capillary Electrophoresis. *Electrophoresis*, 23:613-620, 2002.

-
- [15] Matousek, Lazar, Cip, Petru. Direct Measurement of Index of Refraction of Air by Means of High-Resolution Laser Interferometry. *Pyysica Scripta*, Vol. T118: 48-50, 2005.
- [16] Lotrian, J., Le Menn, M. Refraction Index Measurement by a Laser-Cube-Capillary Technique. *Journal of Physics D: Applied Physics*, 34:1256-1265, 2001.
- [17] Lauer, Miller. An Instrument for the Measurement of the Index of Refraction of Liquids in the Wave-Length Range 200 m μ to 1000 m μ . *Journal of the Optical Society of America*, Vol. 37(8):664-668, 1947.
- [18] Florea. Using a Differential Refractive Index Detector as a Pressure Transducer for Online Viscometry in Exclusion Chromatography. *Journal of Chromatography A*, 878:1-15, 2000.
- [19] Crafton, Fonov, V., Fonov, S., Jones, Goss. The Development of Optical Techniques for the Measurement of Pressure and Skin Friction. *Measurement Science and Technology*, 17:1261-1268, 2006.
- [20] Greywall. Micromechanical Light Modulators, Pressure Gauges, and Thermometers Attached to Optical Fibers. *J. Micromech. Microeng.*, Vol. 7:343-352, 1997.
- [21] Houston, Jarzynski, Zalalutdinov, Bucaro, Lagakos, N. Miniature, High Performance, Low-Cost Fiber Optic Microphone Synopsis. *JASA*, 118(3):6, 2005.
- [22] Kenmore, Tarigan, Neill, Bornhop, D. Capillary-Scale Refractive Index Detection by Interferometric Backscatter. *Analytical Chemistry*, 68(10):1762-1770, 1996.
- [23] Young, Monson, Okiishi. *Fundamentals of Fluid Mechanics*. Wiley, 5th edition, 2006.
- [24] Wood, S. Detecting Flow in a Capillary Using Backscattering Interferometry. Undergraduate Student Internship Report, NASA Glenn Research Center, 2002.
- [25] Birch, Downs. An updated Edlén Equation for the Refractive Index of Air. *Metrologia*, 30:155-162, 1993.
- [26] Edlén. The Refractive Index of Air. *Metrologia*, 2:71-80, 1966.

APPENDIX

A. SYRINGE PUMP CALIBRATION

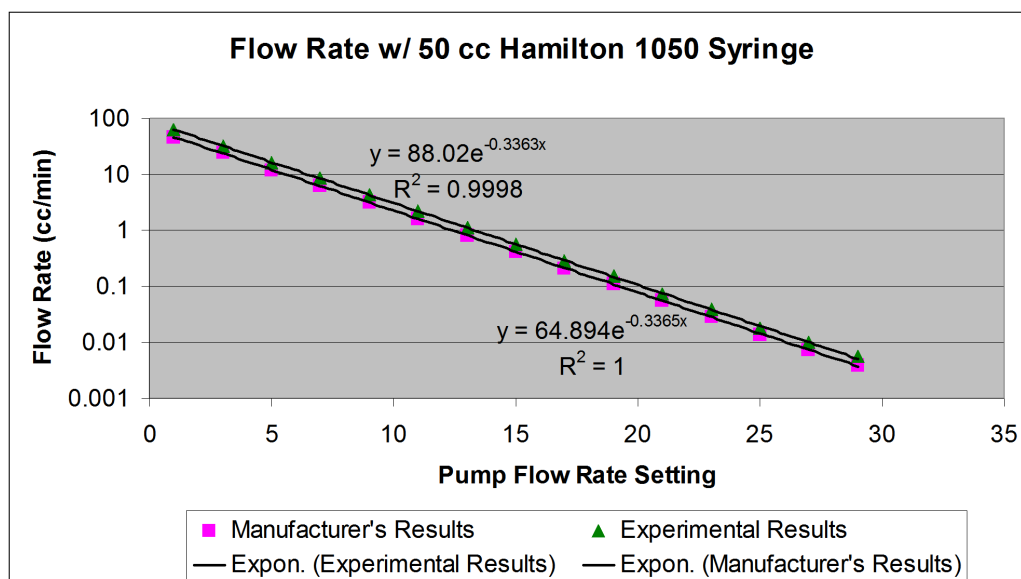
The syringe pump used in flow testing could be set using a numerical scale of integer values between one and thirty where one signified the maximum flow rate. The manufacturer provides corresponding flow rates for select syringe types based upon this scale, however, it was found to be inaccurate for the syringe types in use. The pump was calibrated based on two syringe types used in experimentation. The results have been compared to the manufacturer's reported values for these syringes with excellent agreement in data trends.

Tab. A.1. Linear velocity of syringe pump at various flow rate settings.

Syringe Pump Speeds (Harvard Apparatus 975 - Tag Number 101481)			
Flow Rate Setting Rate Setting	Distance Traveled Under Load (mm)	Time (sec)	Linear Velocity (mm/sec)
1	3.87	30.8	1.26E-01
3	5.38	83.9	6.41E-02
5	4.75	144.9	3.28E-02
7	4.17	247.1	1.69E-02
9	3.94	459.3	8.58E-03
11	3.37	773.2	4.36E-03
13	1.6	716.5	2.23E-03
15	1.6	1399.5	1.14E-03
17	0.93	1608.1	5.78E-04
19	0.67	2233.2	3.00E-04
21	0.48	3339.9	1.44E-04
23	0.23	2921.2	7.87E-05
25	0.18	5017.3	3.59E-05
27	0.14	7085.1	1.98E-05
29	0.07	6271.9	1.12E-05

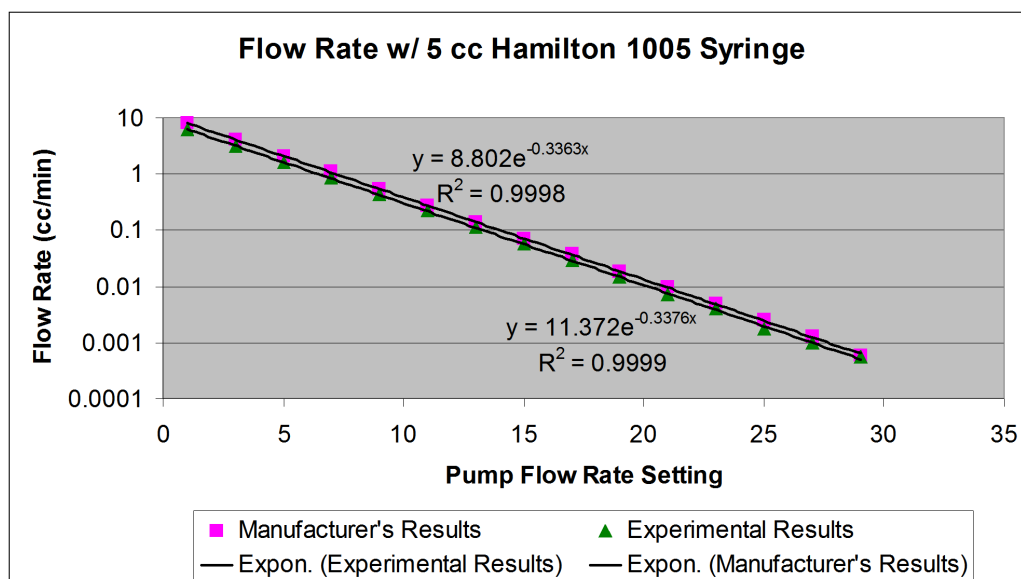
Tab. A.2. Calibration using 50.0 cc Syringe.

Hamilton 1050			
Predicted Flow Rate From Chart	Calculated Flow Rate (cc/min)	Flow Rate (mm ³ /sec)	Percent Difference
4.60E+01	6.28E+01	1047.08	36.58
2.40E+01	3.21E+01	534.37	33.59
1.20E+01	1.64E+01	273.18	36.59
6.20E+00	8.44E+00	140.63	36.09
3.10E+00	4.29E+00	71.49	38.36
1.60E+00	2.18E+00	36.32	36.20
8.20E-01	1.12E+00	18.61	36.16
4.20E-01	5.72E-01	9.53	36.10
2.10E-01	2.89E-01	4.82	37.70
1.10E-01	1.50E-01	2.50	36.37
5.60E-02	7.19E-02	1.20	28.32
2.80E-02	3.94E-02	0.66	40.60
1.40E-02	1.79E-02	0.30	28.13
7.40E-03	9.88E-03	0.16	33.51
3.80E-03	5.58E-03	0.09	46.85

**Fig. A.1.** Calibration of syringe pump for use with a 50.0 cubic centimeter capacity syringe.

Tab. A.3. Calibration using 5.0 cc Syringe.

Hamilton 1005			
Predicted Flow Rate From Chart	Calculated Flow Rate (cc/min)	Flow Rate (mm ³ /sec)	Percent Difference
8.00E+00	6.28E+00	104.71	-21.47
4.10E+00	3.21E+00	53.44	-21.80
2.10E+00	1.64E+00	27.32	-21.95
1.10E+00	8.44E-01	14.06	-23.29
5.40E-01	4.29E-01	7.15	-20.57
2.80E-01	2.18E-01	3.63	-22.17
1.40E-01	1.12E-01	1.86	-20.25
7.20E-02	5.72E-02	0.95	-20.61
3.70E-02	2.89E-02	0.48	-21.85
1.80E-02	1.50E-02	0.25	-16.66
9.60E-03	7.19E-03	0.12	-25.15
4.90E-03	3.94E-03	0.07	-19.66
2.50E-03	1.79E-03	0.03	-28.25
1.30E-03	9.88E-04	0.02	-24.00
6.00E-04	5.58E-04	0.01	-6.99

**Fig. A.2.** Calibration of syringe pump for use with a 5.0 cubic centimeter capacity syringe.

B. PRESSURE TRANSDUCER CLAIBRATION

A Kulite model XCS-062-10D pressure transducer was used for all static testing. To calibrate the transducer, an inclined manometer was connected to the pressurized line of the cell. The results of the calibration can be found in Figure B.1 which shows good agreement between the experimental and manufacturer's sensitivities with only a 0.17% difference between the reported values. It was found that a DC offset of approximately 0.002 mV was required to correct the experimental readings on the day of the calibration. Factors effecting the DC offset include temperature and humidity, although, for differential pressure readings of the pressurized and unpressurized cell, the offset cancels out and only the sensitivity of the transducer is required.

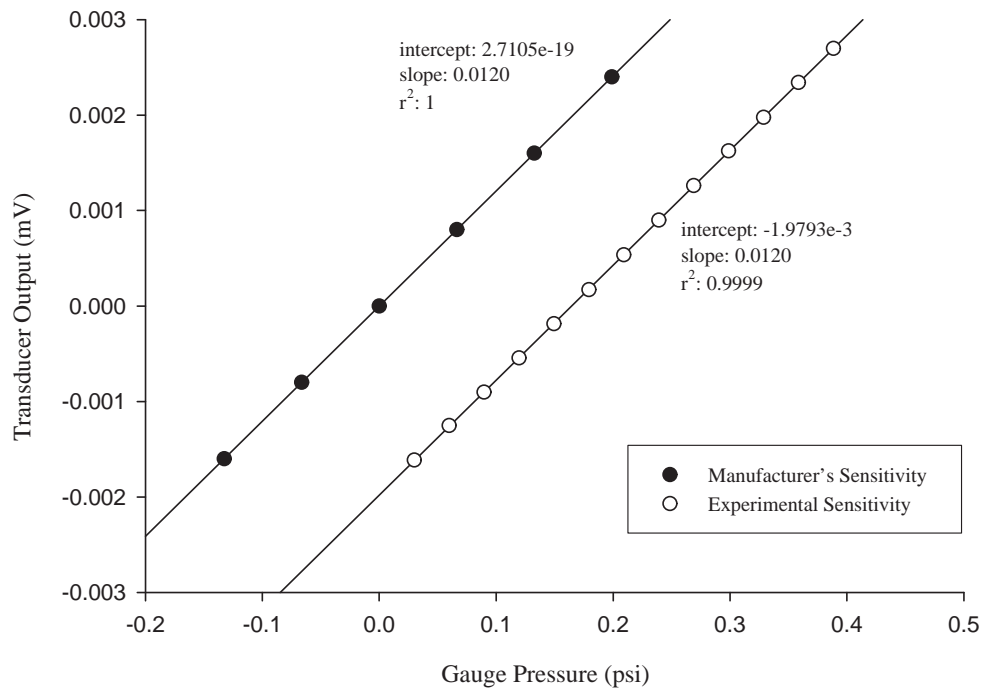


Fig. B.1. Calibration of pressure transducer using an inclined manometer.

C. SPOTLIGHT FRINGE TRACKING RESULTS

This appendix shows the spotlight fringe tracking results for eight areas of interest used in the quantification of fringe shifts for a 500 micron square capillary tube. All data shown is for flowing tests using distilled water in which the flow was induced at frame 30 and extinguished at frame 300 (video capture rate of 3 fps). Flow rates for each pump setting can be determined using the pump calibration tables for the Hamilton 1050 syringe provided in Appendix A.

The horizontal regions in the tracking plots represent instances of constant fringe position or thickness. These regions were averaged to produce the results shown in Figure 7.2. The same procedure was used to create the data presented in Figure 7.6 for the round capillary tube.

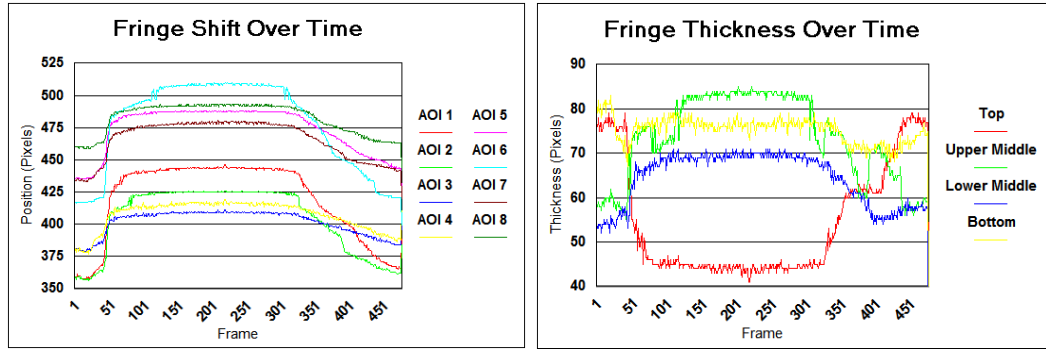


Fig. C.1. Tracking of fringe position and thickness using eight AOI's at a pump flow setting of 17.

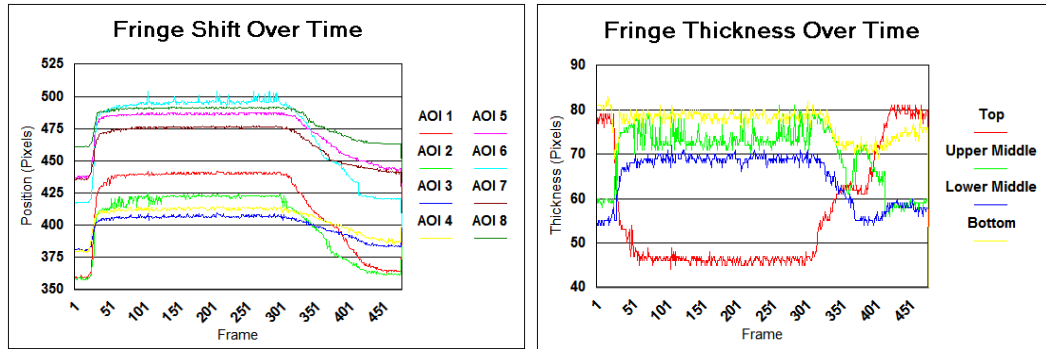


Fig. C.2. Tracking of fringe position and thickness using eight AOI's at a pump flow setting of 19.

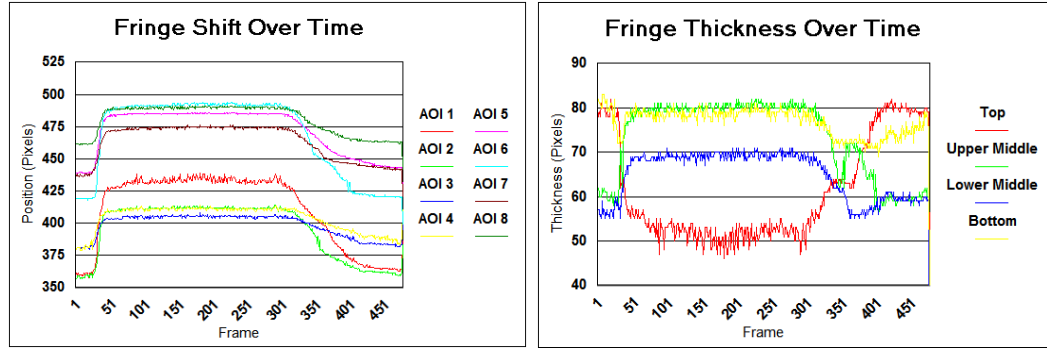


Fig. C.3. Tracking of fringe position and thickness using eight AOI's at a pump flow setting of 21.

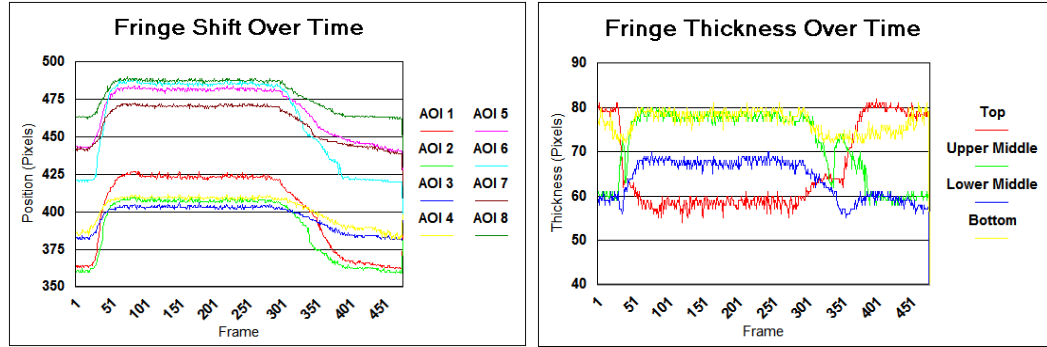


Fig. C.4. Tracking of fringe position and thickness using eight AOI's at a pump flow setting of 23.

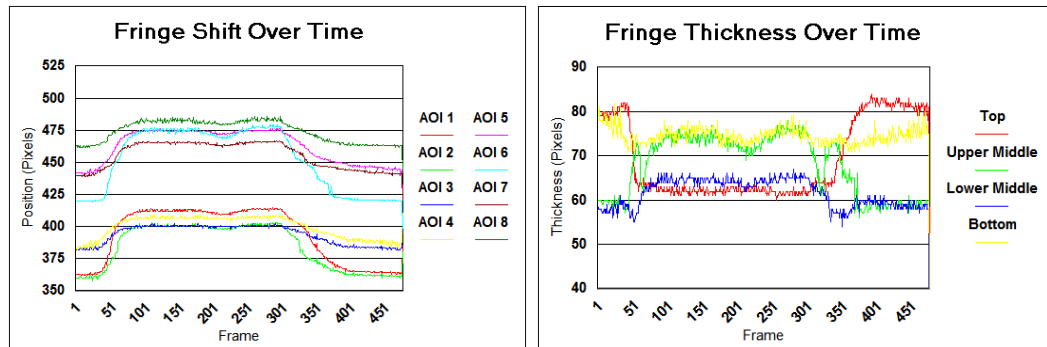


Fig. C.5. Tracking of fringe position and thickness using eight AOI's at a pump flow setting of 25.

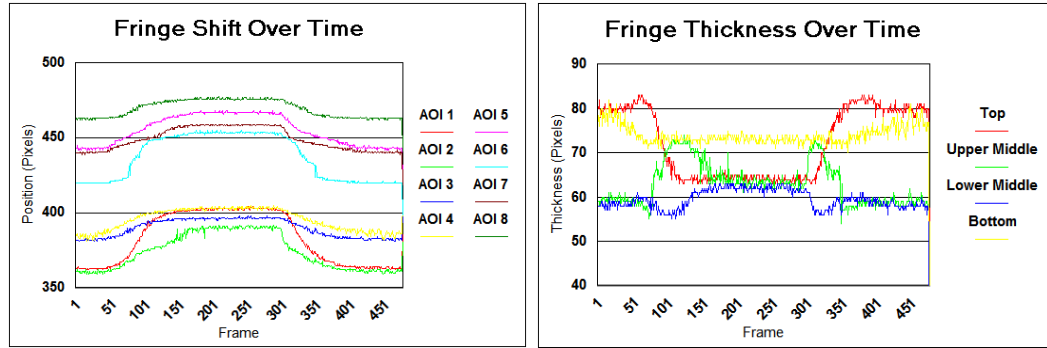


Fig. C.6. Tracking of fringe position and thickness using eight AOI's at a pump flow setting of 27.

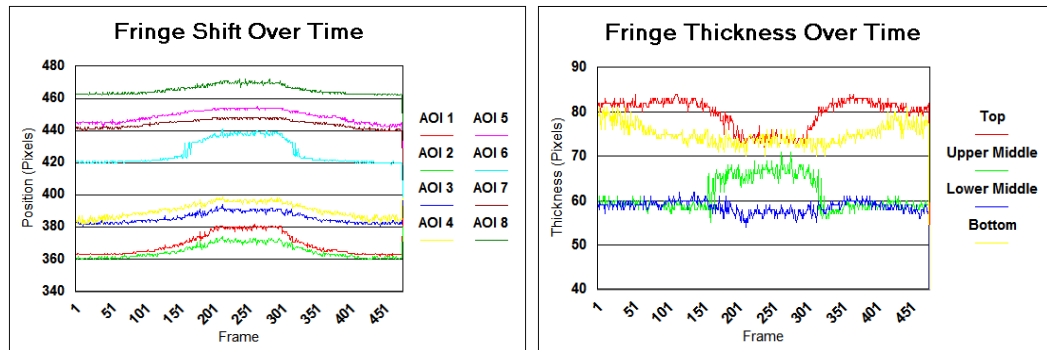


Fig. C.7. Tracking of fringe position and thickness using eight AOI's at a pump flow setting of 29.

D. LASER STABILITY PLOTS

Note that after 12 minutes the neutral density filter was adjusted to lower the intensity of the beam. This effectively lowered the voltage output of the photodetector as shown in Figure D.3. This was done in an attempt to level out the signal more quickly.

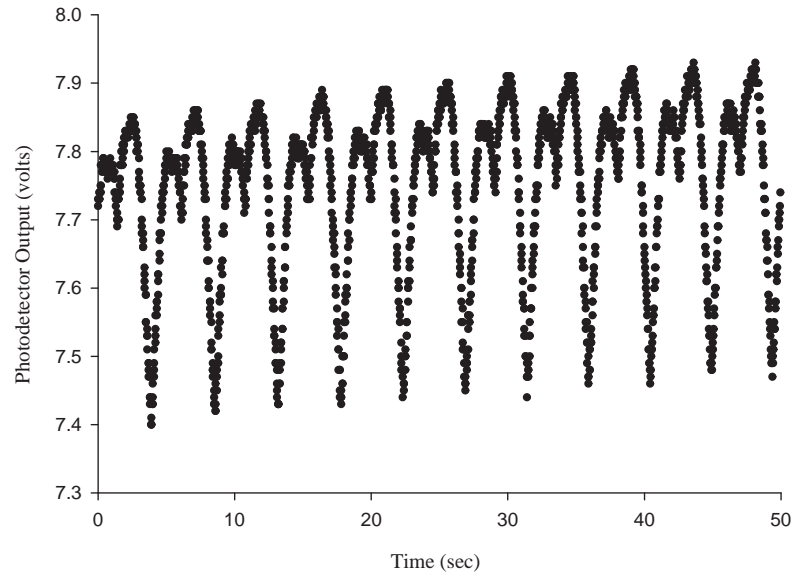


Fig. D.1. Laser intensity fluctuations as captured by the photodetector approximately 2 minutes after laser startup.

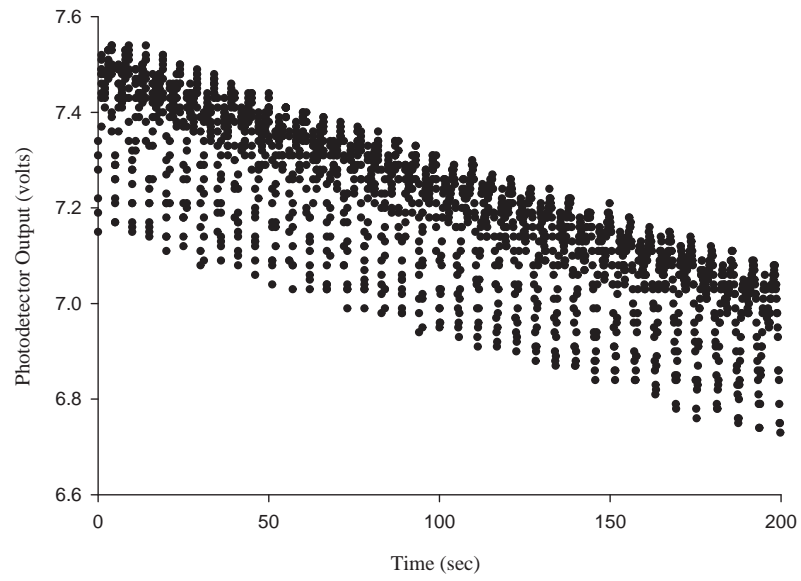


Fig. D.2. Laser intensity fluctuations as captured by the photodetector approximately 10 minutes after laser startup.

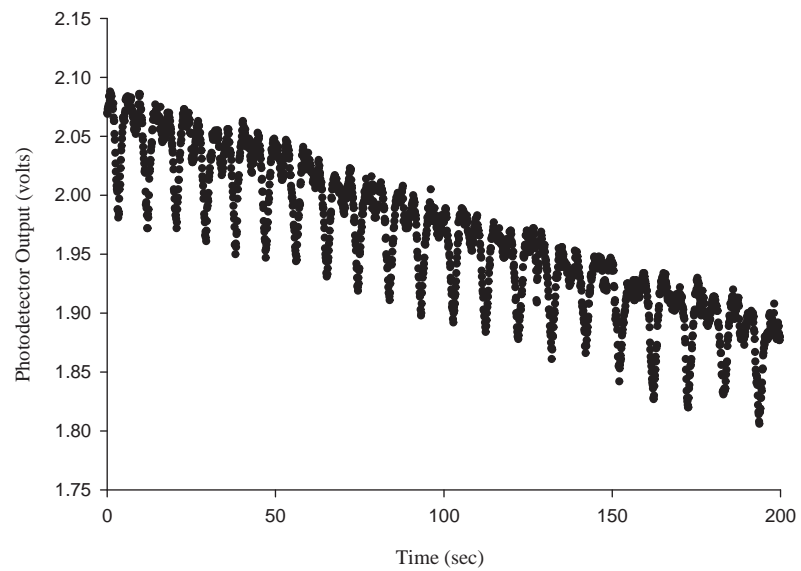


Fig. D.3. Laser intensity fluctuations as captured by the photodetector approximately 16 minutes after laser startup.

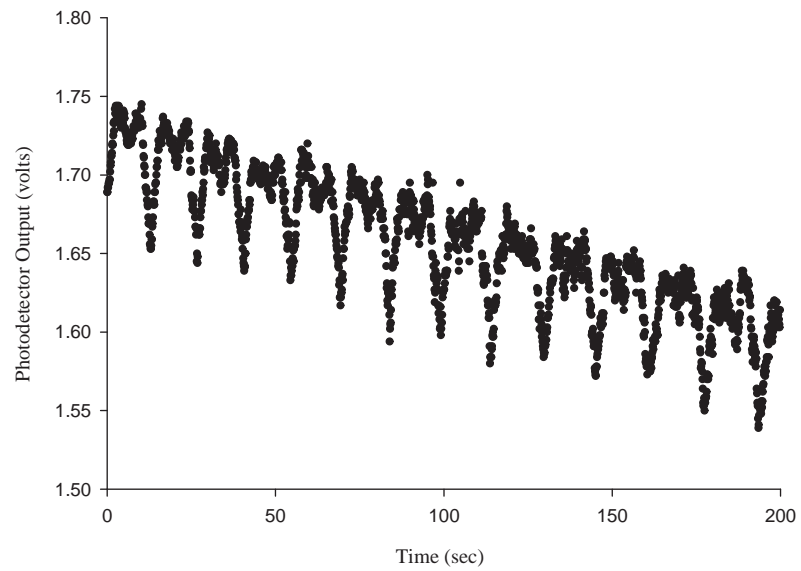


Fig. D.4. Laser intensity fluctuations as captured by the photodetector approximately 23 minutes after laser startup.

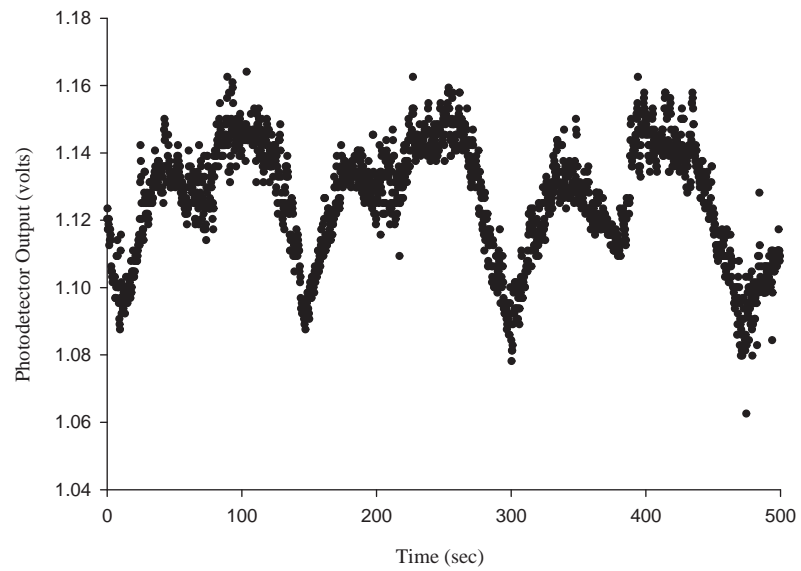


Fig. D.5. Laser intensity fluctuations as captured by the photodetector approximately 70 minutes after laser startup.

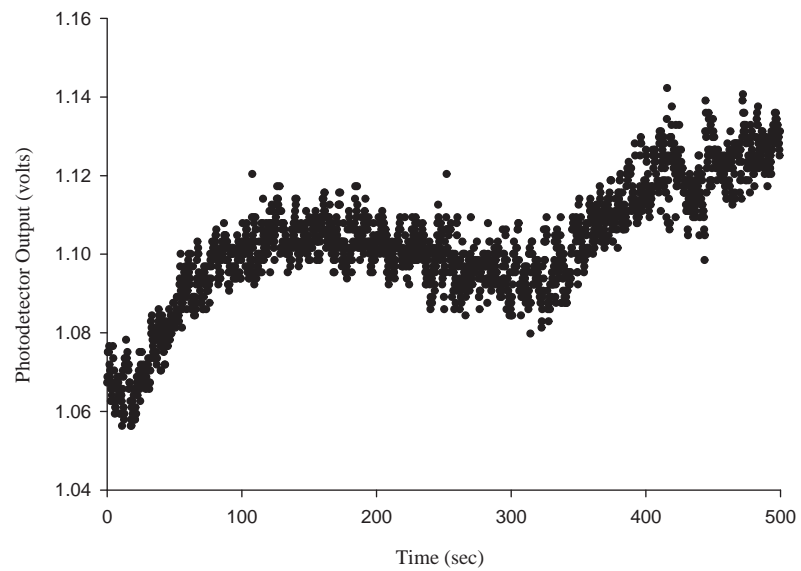


Fig. D.6. Laser intensity fluctuations as captured by the photodetector approximately 120 minutes after laser startup.

E. CONFIGURATIONS FOR RESULTS VERIFICATION

E.1 Tube Pinch-Off Mechanism

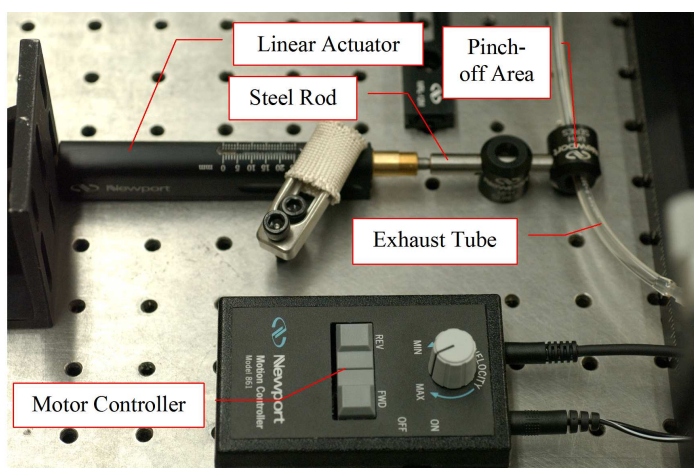


Fig. E.1. Tube pinch-off mechanism used to induce pressure increases at detection point of backscatter set-up.

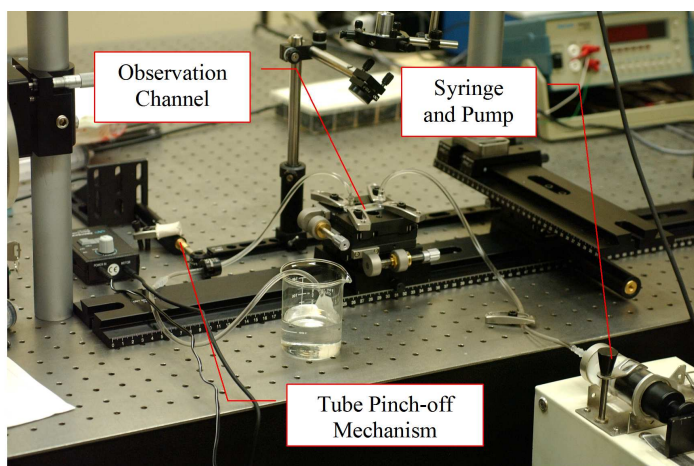


Fig. E.2. Backscatter setup showing placement of pinch-off mechanism and observation channel mounting.

E.2 Michelson Interferometer for Deflection Testing

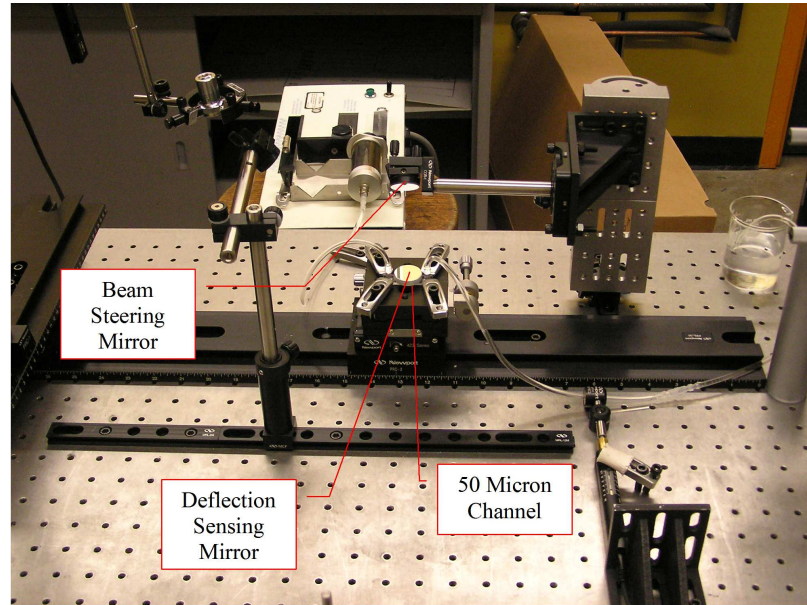


Fig. E.3. Mirror placement on 50 micron channel for deflection sensing leg of Michelson interferometer.

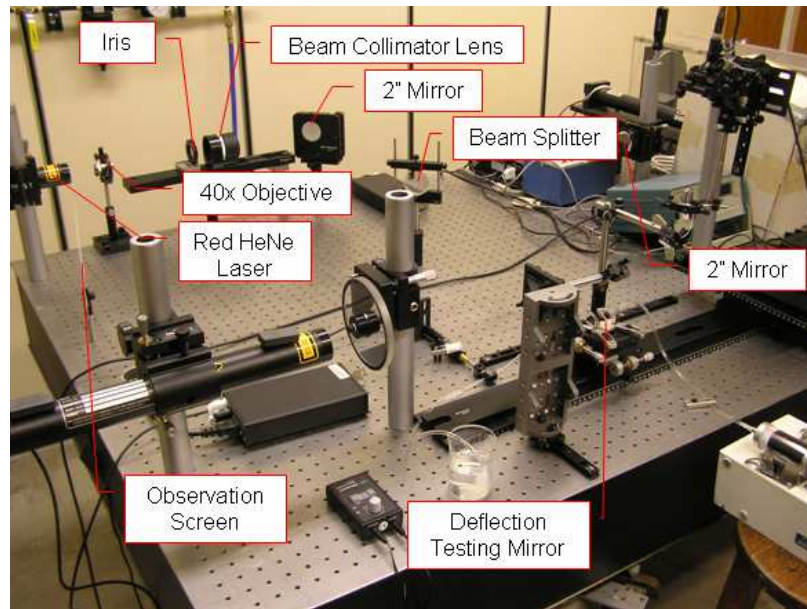


Fig. E.4. Components of the Michelson interferometer used to detect displacements in the glass channel under increased pressure and fluid flow.

F. FRINGE TRACKING PROGRAM

This appendix lists the contents of the fringe tracking program which was written in Matlab to track fringes shifts of transient events.

```
clc
clear
close all
num_fr=2;
first_file=001;
last_file=460;
ff_left_side=zeros(480,num_fr,last_file);
ff_right_side=zeros(480,num_fr,last_file);
ff_thickness=zeros(480,num_fr,last_file);
frame_count=0;
for xxx=first_file:last_file;
    %%%%Load the picture from file%%%%
    [f]=imread('C:\Documents and Settings\Owner\My Documents\SCHOOL\
@@COMMAND LINE WRAP@@ RESEARCH\Image Processing\FR_21_Tracking.tif',xxx);
    f=rgb2gray(f);                %%Convert color image to grayscale

    %%%%FFT%%%%
    PQ = 2*(size(f));
    %%Pads the image with zeros to eliminate wraparound error
    f=double(f);
    Fp = fft2(f, PQ(1), PQ(2));    %%Runs FFT on padded image

    %%%%Image Filtering%%%%%%%%
    D0=2;                          %%Sets size of filter
    sig=D0;

    %%Sets number of standard deviations from center of spectrum for
    %%gaussian filter
    u=0:(PQ(1)-1);
    v=0:(PQ(2)-1);
    ix=find(u > PQ(1)/2);
    u(ix)=u(ix)- PQ(1);
    iy=find(v> PQ(2)/2);
    v(iy)=v(iy)- PQ(2);
    [V,U]=meshgrid(v,u);          %%Create Meshgrid Frequency Array
    D=sqrt(U.^2 + V.^2);
```

```

%%%%Low Pass Filter%%%%
%If using Low Pass Filter: comment out the high pass filter
Hp=exp(-(D.^2)./(2*((2*sig).^2))); %Low Pass Filter

%%%%High Pass Filter%%%%
%If using the High pass filter: comment out loop used for tracking
%left side and right side fringe movement

%Hp=1-Hp;
%%High Pass Fiilter (Comment this line for Low Pass Filter)
Gp = Hp.*Fp; %multiplies image and filter

%%%%InverseFFT%%%%
gp = real(iff2(Gp));
%%Runs inverse FFT on frequency domain image
gpc = gp(1:size(f,1), 1:size(f,2)); %%Resizes image due to padding
figure, imshow(gpc, []); %Shows filtered image
figure, plot(gpc(240, :));
%%Shows histogram of selected row on image (should be smooth sine wave)
%

%%%%Create Binary Image%%%%
gpc=uint8(gpc);
%%Converts data from double to uint8 for processing
level=(graythresh(gpc));
%%Finds the threshold level automatically
%The threshold level can also be manually set using the variable below
%level=.3;
BW = im2bw(gpc,level);
%%Converts image to binary using threshold level

%%%%Edge Detection%%%%
%thresh=(graythresh(f));
%%% Edge funtion typesfor edgetype: 'sobel','prewitt',
%%'roberts','log','canny'
%EDGE=edgetype(gpc,'canny',thresh,sig);

%The code below locates the fringes for tracking
left_side=zeros(length(BW(:,1)),num_fr);
right_side=zeros(length(BW(:,1)),num_fr);
Row=zeros(length(BW(1,:)));
for row_count=1:length(BW(:,1));
    Row=BW(row_count,:);
    column_left=1;
    column_right=1;
    for i=1:length(BW(1,:))-1;
        if ((Row(i) == 0) & (Row(i+1) == 1));

```



```

        left_side(row_count,column_left)=i;
        column_left=column_left+1;
    elseif ((Row(i) == 1) & (Row(i+1) == 0));
        right_side(row_count,column_right)=i;
        column_right=column_right+1;
    end;
end;
end;
%
ff_left_side(:,:,xxx)=left_side;
ff_right_side(:,:,xxx)=right_side;

%Loop calculates fringe thickness
fringe_thickness=zeros(length(left_side(:,1)),length(left_side(1,:)));
for Row=1:length(left_side(:,1));
    for Column=1:length(left_side(1,:));
        if left_side(Row,Column)<right_side(Row,Column);
            fringe_thickness(Row,Column)=right_side(Row,Column)-
@@COMMAND LINE WRAP@@ left_side(Row,Column);
        elseif right_side(Row,Column)<left_side(Row,Column) &
@@COMMAND LINE WRAP@@ right_side(Row,Column)>0;
            fringe_thickness(Row,Column)=right_side(Row,Column+1)-
@@COMMAND LINE WRAP@@ left_side(Row,Column);
        else;
            fringe_thickness(Row,Column)=0;
        end;
    end;
end;

ff_thickness(:,:,xxx)=fringe_thickness;
frame_count=frame_count+1

end;

%%%%Loop to Calculate fringe thickness difference over pixels%%%%
left_side_shift=zeros(length(left_side(:,1)),length(left_side(1,:)),
@@COMMAND LINE WRAP@@ last_file-1);
right_side_shift=zeros(length(right_side(:,1)),length(right_side(1,:)),
@@COMMAND LINE WRAP@@ last_file-1);
for fringe_number=1:num_fr;
    for frame=first_file:last_file-1;
        left_side_shift(:,fringe_number,frame)=ff_left_side(:,fringe_number,
@@COMMAND LINE WRAP@@ frame+1)-ff_left_side(:,fringe_number,frame);
        right_side_shift(:,fringe_number,frame)=ff_right_side(:,fringe_number,
@@COMMAND LINE WRAP@@ frame+1)-ff_right_side(:,fringe_number,frame);
    end;
end;

```

```

        %%%%Loop to Calculate fringe thickness over time from reference%%%%%%%%
        for fringe_number=1:num_fr;
            for frame=first_file:last_file-1;
                abs_left_side_shift(:,fringe_number,frame)=ff_left_side(:,fringe_
@@COMMAND LINE WRAP@@ number,frame+1)-ff_left_side(:,fringe_number,1);
                abs_right_side_shift(:,fringe_number,frame)=ff_right_side(:,fringe_
@@COMMAND LINE WRAP@@ number,frame+1)-ff_right_side(:,fringe_number,1);
            end;
        end;

end;

figure(1), imshow(gpc, []);                %%Shows filtered image
title('Plot of Left Side of First Fringe Through Frames');
figure(2), plot(gpc(240, :));
%%Shows histogram of selected row on image (should be smooth sine wave)
figure(3), imshow(BW);                    %%Shows black and white image
figure(4), imshow(EDGE, []);

%%%%%%%%Plot fringe shift over time%%%%%%%%
plot_shift_l1=left_side_shift(50:400,1,:);
plot_shift_l1=squeeze(plot_shift_l1);
figure(5), mesh(plot_shift_l1);
axis([0 460 5 450 0 10]);
title('Plot of Left Side of First Fringe Through Frames');
%
plot_shift_r1=right_side_shift(50:400,1,:);
plot_shift_r1=squeeze(plot_shift_r1);
figure(6), mesh(plot_shift_r1);
axis([0 460 5 450 0 10]);
title('Plot of Right Side of First Fringe Through Frames');

%%%%%%%%Plot fringe shift from reference%%%%%%%%
plot_abs_shift_l1=abs_left_side_shift(50:400,1,:);
plot_abs_shift_l1=squeeze(plot_abs_shift_l1);
figure(7), mesh(plot_abs_shift_l1);
axis([0 460 5 450 0 10]);
title('Plot of absolute Left Side of First Fringe Through Frames');
%
plot_abs_shift_r1=abs_right_side_shift(50:400,1,:);
plot_abs_shift_r1=squeeze(plot_abs_shift_r1);
figure(8), mesh(plot_abs_shift_r1);
axis([0 460 5 450 0 10]);
title('Plot of absolute Right Side of First Fringe Through Frames');
%
%Plot fringe thickness over time
%First Fringe

```

```
plot_fringe_1=ff_thickness(:,1,:);  
plot_fringe_1=squeeze(plot_fringe_1);  
figure, mesh(plot_fringe_1);  
title('Change in Thickness of First Fringe Through Frames');
```

G. MATLAB CODE FOR STATIC PRESSURE TEST PROCESSING

The code provided in this appendix is a modified version of that found in Appendix F. Here the experimental procedure involved a capturing of two separate data files, the first containing images of unshifted fringes and the second containing images after the shift had occurred. The two files are processed separately and then compared to determine shift magnitude and thickness changes. This two file method was used to save hard drive space and reduce data processing time with equivalent results to the earlier method.

```
%%Derek Fultz
%%7-27-07
%
%%This program is used to process a pair of files for shifted and unshifted
%%fringes used in static pressure testing of the backscatter
%%interferometer.
%
clc
clear
%
%%File Inputs%%%
%
%%Enter the number of bright fringes in the image
num_fr=1;
%
%%Enter the video frames to be processed
first_file=001;
last_file=15;
%
%
%%Create empty matrices to allocate memory and speed up program
ff_left_side=zeros(480,num_fr,last_file);
ff_right_side=zeros(480,num_fr,last_file);
ff_thickness=zeros(480,num_fr,last_file);
%%Initial Frame Counter
frame_count_unshifted=0;
%%Construct loop to process video one frame at a time
for xxx=first_file:last_file;
%%Enter first file with unshifted fringe data (file f)
```

```

[f]=imread('F:\DEREK\Static Pressure Tests 7_27_07\Test_20_Unshifted.tif'
@@COMMAND LINE WRAP@@ ,xxx);
%
%%Image Processing Procedures%%
%
f=rgb2gray(f);           %%Convert color image to grayscale
PQ = paddedsize(size(f));
%%Pads the image with zeros to eliminate wraparound error
Fp = fft2(f, PQ(1), PQ(2)); %%Runs FFT on padded image
%%Choose filter size based on frequencies to be eliminated
D0=2;                    %%Sets size of filter
sig=D0;
%%Sets number of standard deviations from center of spectrum for
%%gaussian filter
Hp = lpfilter('gaussian', PQ(1), PQ(2), 2*sig);
%%Performs gaussian low pass filter on image
Gp = Hp.*Fp;
%%multiplies image and filter (convolution in spatial domain)
gp = real(ifft2(Gp));    %%Runs inverse FFT on frequency domain image
gpc = gp (1:size(f,1), 1:size(f,2)); %%Resizes image due to padding
figure, imshow(gpc, []); %%Shows filtered image
figure, plot(gpc(240, :));
%%Shows histogram of selected row on image (should be smooth sine wave)
%
gpc=uint8(gpc);
%%Converts data from double to uint8 for processing
level=(graythresh(gpc)); %%Finds the threshold level automatically
%%The threshold level can also be manually set using the variable below
%level=.3; %%Enter manual threshold choice here
%
%%Change image to black and white only
BW = im2bw(gpc,level);
%%Converts image to binary using threshold level
figure, imshow(BW);      %%Shows black and white image
title('Black and White Image-Unshifted');
%%Show the square wave created by the fringes
% figure, plot(BW(240, :));
% axis([-5 757 -.25 1.25]);
%
%
%%Locate Fringes%%
%
left_side=zeros(length(BW(:,1)),num_fr);
right_side=zeros(length(BW(:,1)),num_fr);
Row=zeros(length(BW(1,:)));
for row_count=1:length(BW(:,1));
    Row=BW(row_count,:);

```

```

column_left=1;
column_right=1;
for i=1:length(BW(1,:))-1;
    if ((Row(i) == 0) & (Row(i+1) == 1));
        left_side(row_count,column_left)=i;
        column_left=column_left+1;
    elseif ((Row(i) == 1) & (Row(i+1) == 0));
        right_side(row_count,column_right)=i;
        column_right=column_right+1;
    end;
end;
end;
%%Store fringe locations for left and right side in each frame
ff_left_side(:,:,xxx)=left_side;
ff_right_side(:,:,xxx)=right_side;
%
%
%%Calculate fringe thickness of bright fringes%%%
%
%%Note: It is recommended that this portion of code be used on a
%%cropped image
%
%%Use find command to increase the speed of these loops:
%indices=find(x(1:length(x)-1)<0.5 & x(2:length(x))>0.5);
%
fringe_thickness=zeros(length(left_side(:,1)),length(left_side(1,:)));
for Row=1:length(left_side(:,1));
    for Column=1:length(left_side(1,:));
        if left_side(Row,Column)<right_side(Row,Column);
            fringe_thickness(Row,Column)=right_side(Row,Column)-left_side
@@COMMAND LINE WRAP@@ (Row,Column);
        elseif right_side(Row,Column)<left_side(Row,Column) & right_side
@@COMMAND LINE WRAP@@ (Row,Column)>0;
            fringe_thickness(Row,Column)=right_side(Row,Column+1)-left_side
@@COMMAND LINE WRAP@@ (Row,Column);
        else;
            fringe_thickness(Row,Column)=0;
        end;
    end;
end;
end;
%%Store fringe thickness for each frame
ff_thickness(:,:,xxx)=fringe_thickness;
%
%%Advance frame counter
frame_count_unshifted=frame_count_unshifted+1
%
end;

```

```

%
%%Find average values to eliminate measurement errors
for count=1:15
f_average_position_left(count)=mean(ff_left_side(210:310,1,count));
f_average_position_right(count)=mean(ff_right_side(210:310,1,count));
f_average_thickness(count)=mean(ff_thickness(210:310,1,count));
end
%%Save average values for file f
f_average_position_left=mean(f_average_position_left(:));
f_average_position_right=mean(f_average_position_right(:));
f_average_thickness=mean(f_average_thickness(:));
%%%%%%
%%%%%%
%%%%%%
%%%%%%
%
%%%%Begin tracking on frames of fringe data after shift%%
clc
%%Create empty matrices to speed up code and save memory
gf_left_side=zeros(480,num_fr,last_file);
gf_right_side=zeros(480,num_fr,last_file);
gf_thickness=zeros(480,num_fr,last_file);
%%Initialize counter
frame_count_shifted=0;
%
for xxx=first_file:last_file;
%%Read the shifted frame from file (file g)
[g]=imread('F:\DEREK\Static Pressure Tests 7_27_07\Test_20_Shifted.tif'
@@COMMAND LINE WRAP@@ ,xxx);
%
%
g=rgb2gray(g);           %%Convert color image to grayscale
PQ = paddedsize(size(g));
%%Pads the image with zeros to eliminate wraparound error
Fp = fft2(g, PQ(1), PQ(2)); %%Runs FFT on padded image
D0=2;                    %%Sets size of filter
sig=D0;
%%Sets number of standard deviations from center of spectrum for gaussian
%%filter
Hp = lpfilter('gaussian', PQ(1), PQ(2), 2*sig);
%%Performs gaussian low pass filter on image
Gp = Hp.*Fp;
%%multiplies image and filter (convolution in spatial domain)
gp = real(ifft2(Gp));    %%Runs inverse FFT on frequency domain image
gpc = gp (1:size(g,1), 1:size(g,2)); %%Resizes image due to padding
figure, imshow(gpc, []); %%Shows filtered image
figure, plot(gpc(240, :));

```

```

%%Shows histogram of selected row on image (should be smooth sine wave)
%
gpc=uint8(gpc);
%%Converts data from double to uint8 for processing
level=(graythresh(gpc));    %%Finds the threshold level automatically
%%The threshold level can also be manually set using the variable below
%level=.3;
%
%%Change image to black and white only
BW = im2bw(gpc,level);
%%Converts image to binary using threshold level
figure, imshow(BW);        %%Shows black and white image
title('Black and White Image-Shifted');
%%Show the square wave created by the fringes
% figure, plot(BW(240, :));
% axis([-5 757 -.25 1.25]);
%
%
%%The code below locates the fringes for tracking
left_side=zeros(length(BW(:,1)),num_fr);
right_side=zeros(length(BW(:,1)),num_fr);
Row=zeros(length(BW(1,:)));
for row_count=1:length(BW(:,1));
    Row=BW(row_count,:);
    column_left=1;
    column_right=1;
    for i=1:length(BW(1,:))-1;
        if ((Row(i) == 0) & (Row(i+1) == 1));
            left_side(row_count,column_left)=i;
            column_left=column_left+1;
        elseif ((Row(i) == 1) & (Row(i+1) == 0));
            right_side(row_count,column_right)=i;
            column_right=column_right+1;
        end;
    end;
end;
%
gf_left_side(:,:,xxx)=left_side;
gf_right_side(:,:,xxx)=right_side;
%
%
%%The code below is used to calculate fringe thickness (bright fringes)
%%It is recommended that this portion of code be used on a cropped image
%
%%Use find command to increase the speed of these loops:
%indices=find(x(1:length(x)-1)<0.5 & x(2:length(x))>0.5);
%

```

```

fringe_thickness=zeros(length(left_side(:,1)),length(left_side(1,:)));
for Row=1:length(left_side(:,1));
    for Column=1:length(left_side(1,:));
        if left_side(Row,Column)<right_side(Row,Column);
            fringe_thickness(Row,Column)=right_side(Row,Column)-left_side
@@COMMAND LINE WRAP@@ (Row,Column);
        elseif right_side(Row,Column)<left_side(Row,Column) & right_side
@@COMMAND LINE WRAP@@ (Row,Column)>0;
            fringe_thickness(Row,Column)=right_side(Row,Column+1)-
@@COMMAND LINE WRAP@@ left_side(Row,Column);
        else;
            fringe_thickness(Row,Column)=0;
        end;
    end;
end;
%
gf_thickness(:, :, xxx)=fringe_thickness;
%
frame_count_shifted=frame_count_shifted+1
%
end;
%
%
%%Finding average values
for count=1:15
    g_average_position_left(count)=mean(gf_left_side(210:310,1,count));
    g_average_position_right(count)=mean(gf_right_side(210:310,1,count));
    g_average_thickness(count)=mean(gf_thickness(210:310,1,count));
end
%
g_average_position_left=mean(g_average_position_left(:));
g_average_position_right=mean(g_average_position_right(:));
g_average_thickness=mean(g_average_thickness(:));
%%%%%%
%%%%%%
%%%%%%
%%%%%%
%%Find fringe shift and thickness changes between files f and g
final_fringe_shift_left=f_average_position_left-g_average_position_left
final_fringe_shift_right=f_average_position_right-g_average_position_right
final_fringe_thickness_change=g_average_thickness-f_average_thickness
thickness_shifted=g_average_thickness

```

H. MATLAB EXTERNAL FUNCTIONS

Listed below are the external user defined functions required to run the fringe tracking codes provided in Appendices F and G. These short codes can also be found with more detailed explanation in the Digital Image Processing Using Matlab text by R. Gonzalez [4].

```
%%%%%%%%%%%%%%%%%%%%%%%%%%%%%%%%%%%%%%%%%%%%%%%%%%%%%%%%%%%%%%%%%%%%%%%%
%%% Function to pad image %%%
%%%%%%%%%%%%%%%%%%%%%%%%%%%%%%%%%%%%%%%%%%%%%%%%%%%%%%%%%%%%%%%%%%%%%%%%
function PQ = paddedsize(AB,CD,PARAM)
%
if nargin==1
    PQ=2*AB;
elseif nargin==2 & ~ischar(CD)
    PQ=AB+CD-1;
    PQ=2*ceil(PQ/2);
elseif nargin==2
    m=max(AB); %Maximum dimension.
    P=2^nextpow2(2*m);
    PQ=[P,P];
else
    error('Wrong number of inputs')
end

%%%%%%%%%%%%%%%%%%%%%%%%%%%%%%%%%%%%%%%%%%%%%%%%%%%%%%%%%%%%%%%%%%%%%%%%
%%% Function to perform frequency domain filtering %%%
%%%%%%%%%%%%%%%%%%%%%%%%%%%%%%%%%%%%%%%%%%%%%%%%%%%%%%%%%%%%%%%%%%%%%%%%
function g = dftfilt(f,H)
%
%Obtain the FFT of the padded input.
F=fft2(f,size(H,1),size(H,2));
%
%Perform filtering.
g=real(ifft2(H.*F));
%
%Crop to original size.
g=g(1:size(f,1), 1:size(f,2));
```

```

%%%%%%%%%%%%%%%%%%%%%%%%%%%%%%%%%%%%%%%%%%%%%%%%%%%%%%%%%%%%%%%%%%%%%%%%%%%%%%
%%% Function to make meshgrid frequency matrices %%%
%%%%%%%%%%%%%%%%%%%%%%%%%%%%%%%%%%%%%%%%%%%%%%%%%%%%%%%%%%%%%%%%%%%%%%%%%%%%%%
function [U, V] = dftuv(M,N)
%
%Set up range of variables.
u=0:(M-1);
v=0:(N-1);
%
%Compute the indices for use in meshgrid.
idx=find(u > M/2);
u(idx) = u(idx) - M;
idy = find(v > N/2);
v(idy) = v(idy) - N;
%
%Compute the meshgrid arrays
[V, U] = meshgrid(v,u);

%%%%%%%%%%%%%%%%%%%%%%%%%%%%%%%%%%%%%%%%%%%%%%%%%%%%%%%%%%%%%%%%%%%%%%%%%%%%%%
%%% Function to run low pass filter on image %%%
%%%%%%%%%%%%%%%%%%%%%%%%%%%%%%%%%%%%%%%%%%%%%%%%%%%%%%%%%%%%%%%%%%%%%%%%%%%%%%
function H = lpfilter(type, M, N, D0, n)
%
%Use function dftuv to set up the meshgrid arrays needed for computing the
%required distances.
[U, V] = dftuv(M, N);
%
%Compute the distances D(U, V);
D=sqrt(U.^2 + V.^2);
%
switch type
    case 'ideal'
        H=double(D <= D0);
    case 'btw'
        if nargin ==4
            n=1;
        end
        H = 1./(1+(D./D0).^(2*n));
    case 'gaussian'
        H = exp(-(D.^2)./(2*(D0^2)));
    otherwise
        error('Unknown filter type')
end

```

I. PROGRAM TO FIND SENSITIVITY USING WATER

This appendix lists the contents of the Matlab program used to find the sensitivity using water under different experimental conditions.

```
%Derek Fultz
%10-25-06
%
%
%This program finds the minimum RI change detectable using this technique
%as well as the minimum associated pressure change detectable for water.
%
clc
clear
%
%%Experimental Inputs%%
fringe_thickness=400;
%Thickness of light and dark fringe together in pixels
min_delta_m=1/fringe_thickness;
%Minimum detectable dimensionless fringe shift
RI_glass=1.46;           %Refractive index of fused quartz
RI_air=1.0003;           %Approx. RI of air for angle calculation
theta_i=13;              %impingement angle in degrees
theta_i=theta_i*pi/180;  %impingement angle in radians
theta=asin(sin(theta_i)*(RI_air/RI_glass)); %angle through glass
p_barometric=736.4;      %Pressure in mm Hg
p_barometric=p_barometric*(101325/760.0); %Pressure in pascals
temp=24;                  %room temperature in deg C
%
%
%%Known Values%%
lambda=633e-9;           %Wavelength of the light in meters
thickness=50e-6;          %Original channel thickness in meters
%
%
RI_water_exp_conditions=1.332;
%The refractive index of water under the experimental conditions
theta_prime_1=asin(sin(theta)*(RI_glass/RI_water_exp_conditions));
%angle of light in water
m_initial=(2*thickness*RI_water_exp_conditions*cos(theta_prime_1))
@@COMMAND LINE WRAP@@ /(lambda);
```

```

%inital fringe value from vacuum
%
%
new_m=m_initial+min_delta_m; %defines m with min detectable shift
%
%
new_RI_water=RI_water_exp_conditions; %sets an initial value
m=1; %sets an initial value
while m < new_m ; %uses a while loop to avoid external functions
    theta_prime_2=asin(sin(theta)*(RI_glass/new_RI_water));
    m=(2*thickness*new_RI_water*cos(theta_prime_2))/(lambda);
    new_RI_water=new_RI_water+.0000000001;
end
%
%
new_RI_water; %displays the new refractive index of the water
RI_change=new_RI_water-RI_water_exp_conditions %min detectable RI change
%
%
%Find the pressure increase associated with the change in RI of water
p=(RI_change/((16.84-0.129*temp+0.0022*temp^2)*10^-6))*(p_barometric*
@@COMMAND LINE WRAP@@ 1.4508e-4)
%min detectable pressure based on RI change

```

J. PROGRAM TO FIND SENSITIVITY USING AIR

This appendix lists the contents of the Matlab program used to find the sensitivity using air under different experimental conditions.

```
%Derek Fultz
%10-25-06
%
%
%This program finds the minimum RI change detectable using this technique
%as well as the minimum associated pressure change detectable for air.
%
clc
clear
%
%%Experimental Inputs%%
fringe_thickness=400;
%Thickness of light and dark fringe together in pixels
min_delta_m=1/fringe_thickness;
%Minimum detectable dimensionless fringe shift
RI_glass=1.46;           %Refractive index of fused quartz
RI_air=1.0003;           %Approx. RI of air for angle calculation
theta_i=13;              %impingement angle in degrees
theta_i=theta_i*pi/180;  %impingement angle in radians
theta=asin(sin(theta_i)*(RI_air/RI_glass)); %angle through glass
p_barometric=739.7;      %Pressure in mm Hg
p_barometric=p_barometric*(101325/760.0); %Pressure in pascals
temp=23; %room temperature in deg C
%
%
%%Known Values%%
lambda=633e-9; %Wavelength of the light in Meters
thickness=50e-6; %Original Channel Thickness in Meters
%
%
%%Calculated Values%%
lambda_vac=.633; %(micrometers)
sigma=1/lambda_vac;
n_s=1+(.0472326*(173.3-sigma^2)^-1);
RI_air_exp_conditions=1+((n_s-1)*((p_barometric*(1+p_barometric*(60.1-
@@COMMAND LINE WRAP@@ .972*temp)*10^-10))/(96095.43*(1+.003661*temp))));
```

```

theta_prime=asin(sin(theta)*(RI_glass/RI_air_exp_conditions));
theta_prime_deg=theta_prime*(180/pi);
m_initial=(2*thickness*RI_air_exp_conditions*cos(theta_prime))/(lambda);
%
%
new_m=m_initial+min_delta_m;
%
%
new_RI_air=RI_air_exp_conditions;
m=1;
while m < new_m ;
    theta_prime_2=asin(sin(theta)*(RI_glass/new_RI_air));
    m=(2*thickness*new_RI_air*cos(theta_prime_2))/(lambda);
    new_RI_air=new_RI_air+.0000000001;
end
%
%
new_RI_air;
RI_change=new_RI_air-RI_air_exp_conditions %min detectable RI change
%
%
%Find the pressure increase associated with the change in RI of water
RI_change_loop=0;
pressure=p_barometric;
while RI_change_loop<RI_change;
    RI_air=1+((n_s-1)*((pressure*(1+pressure*(60.1-.972*temp)*10^-10))/
@@COMMAND LINE WRAP@@ (96095.43*(1+.003661*temp)))));
    RI_change_loop=RI_air-RI_air_exp_conditions;
    pressure=pressure+.1; %advance pressure in Pa
end
pressure=pressure-p_barometric; %pressure in Pa
pressure=pressure*(1.4508e-4) %min detectable pressure in psi

```